MAX-PLANCK-GESELLSCHAFT

TECHNISCHE
UNIVERSITÄT
DARMSTADT

Investigation of Microstructural Defects in Cu(In,Ga)Se_2 Thin Films by Scanning Transmission Electron Microscopy

Dissertation

zur Erlangung des akademischen Grades eines
Doktor-Naturwissenschaften (Dr. rer. nat.)

von

M. Sc. Ekin ŞİMŞEK SANLI

aus der Türkei

vom Fachbereich Material- und Geowissenschaften
der Technischen Universität Darmstadt

angefertigt am
Max-Planck-Institut für Festkörperforschung,
Stuttgarter Zentrum für Elektronenmikroskopie (StEM)

Darmstadt 2018

D17

Simsek Sanli, Ekin: Investigation of Microstructural Defects in Cu(In,Ga)Se$_2$ Thin Films by Scanning Transmission Electron Microscopy

Darmstadt, Technische Universität Darmstadt
Year thesis published in TUprints 2019
URN:urn:nbn:de:tuda-tuprints-88492
Date of the viva voce 01.10.2018

Investigation of Microstructural Defects in $Cu(In,Ga)Se_2$ Thin Films by Scanning Transmission Electron Microscopy

Prüfungskommission

1. Referent: Prof. Dr. Hans-Joachim Kleebe

2. Referent: Prof. Dr. Peter A. van Aken

Prüfer: Prof. Dr. Wolfram Jaegermann

Prüfer: Prof. Dr. Christoph T. Koch

Tag der Einreichung: 20.08.2018

Tag der Prüfung: 01.10.2018

Darmstadt, 2018 – D17

This page intentionally left blank.

Abstract

Polycrystalline $Cu(In,Ga)Se_2$ (CIGS) based thin-film solar cells achieve power-conversion efficiencies of almost 23% on the laboratory scale, one of the highest among thin-film solar cells. The aim of further CIGS research and development is to reach conversion efficiencies of 25%, which is currently the efficiency of the best single-crystalline Si based solar cells. To reach this goal, the factors limiting efficiency, *e.g.* non-radiative recombination of charge carriers, should be minimized. Such recombination processes may occur at line or planar defects present in the CIGS absorbers (among other interfaces, such as absorber and buffer layer). In the present study, the structure and composition of several defects as well as their evolution during the growth were investigated for an enhanced understanding.

Highest efficiencies in CIGS solar cells are achieved, when the absorber is fabricated with a three-stage co-evaporation process. During the second stage of this process, Cu and Se are evaporated on the initially formed $(In,Ga)_2Se_3$ layer. The composition of the absorber becomes Cu-rich ($[Cu]/([In] + [Ga]) > 1$) during this stage. The change in composition leads to recrystallization, *i.e.* grain growth and defect annihilation, thus enabling higher conversion efficiencies. Therefore, it is crucial to investigate the recrystallization and the evolution of the microstructure at the second-stage of the CIGS growth. In the literature, two methods were suggested for this purpose: *i)* investigating the microstructural evolution of diffusion couples during a heating study; *ii) ex-situ* comparison of a growth-interrupted and a growth-finished sample.

In the first part of this study, a Cu-poor ($[Cu]/([In] < 1$) $CuInSe_2$ (CIS) precursor layer with a $Cu_{2-x}Se$ capping layer was prepared and heated in a scanning transmission electron microscope (STEM) to mimic the recrystallization. During the Cu diffusion from the Cu-rich $Cu_{2-x}Se$ phase into the Cu-poor CIS phase, the growth of defect-free grains towards the grains with closely-spaced planar defects (PDs) was monitored by low-angle annular dark-field (LAADF) imaging, whereas elemental depth profiles were analyzed by energy-dispersive X-ray spectroscopy (EDXS) before and after heating. The substantial impact of the Cu excess on the recrystallization was also indicated by an *in-situ* heating experiment of a Cu-poor CIS film without a $Cu_{2-x}Se$ layer on top, in which neither grain growth nor defect annihilation was detected. Monitoring of the recrystallization within the CIS absorber layers was performed for the first time by means of STEM and provided direct evidence for the currently accepted theory of the grain growth mechanism.

In the second part, a CIGS absorber grown via co-evaporation was analyzed. During the growth, one piece of the sample was removed before the recrystallization at the second stage. For the remaining piece, the three-stage process was completed. The defect concentrations as well as the in-depth elemental analysis were performed by STEM-LAADF imaging and EDXS, respectively. Similar to the *in-situ* heating results, much larger grains with reduced linear/planar defect concentrations were detected in the absorber layer for which the growth had been completed. Although most of the structural defects were annihilated after the recrystallization, few structural defects were detected by LAADF imaging after the recrystallization, and even after the completion of the three-stage growth process.

Further analyses were performed via aberration-corrected, high-resolution STEM (HR-STEM) in combination with electron energy-loss spectroscopy (EELS) to elucidate the nature of individual microstructural defects from various stages of the growth. HR-STEM and EELS results revealed the structure and chemistry of defects that were present in both growth-interrupted and growth-finished samples: Σ3-twin boundaries and stacking faults with stoichiometric elemental distribution; grain boundaries, tilt boundaries and dislocations with cation redistribution, *i.e.* Cu enrichment and In depletion. Stoichiometric inversion boundaries, Cu enriched ‘complex’ PDs and an extrinsic Frank partial dislocation were detected only in the growth-interrupted Cu-poor samples, whereas a ‘$Cu_{2-x}Se$ secondary phase’ was detected only in the growth-finished absorber layer.

The present work provided direct insight into the recrystallization of CIGS absorbers and evolution of structural defects, as well as a thorough investigation of individual defects in CIGS absorbers.

Zusammenfassung

Auf polykristallinem $Cu(In,Ga)Se_2$ (CIGS) basierende Dünnschichtsolarzellen erreichen im Labor einen Wirkungsgrad von bis zu 23%, eine der höchsten aller Dünnschichtsolarzellen. Ein Ziel weiterer Forschung und Entwicklung auf dem Gebiet von CIGS-Solarzellen ist das Erreichen eines Wirkungsgrades von 25% und mehr, welchen monokristalline Silizium-Solarzellen aufweisen. Um dieses Ziel zu erreichen, sollten limitierende Faktoren, wie z.B. nichtstrahlende Rekombination von Ladungsträgern, reduziert werden. Solche Rekombinationsprozesse können an Versetzungen und planaren Gitterdefekten in den Absorbern (und an Grenzflächen wie diejenige zwischen Absorber und Pufferschicht) verstärkt auftreten. Das Ziel der vorliegenden Arbeit ist es, ein besseres Verständnis der Struktur und Zusammensetzung dieser Defekte sowie ihrer Entwicklung während des CIGS-Wachstums zu erlangen.

Die höchste Effizienz für CIGS-Solarzellen wird erreicht, wenn der CIGS-Absorber in einem dreistufigen Koverdampfungsprozess hergestellt wird. Während der zweiten Stufe dieses Prozesses verdampft man Kupfer und Selen auf der in der ersten Stufe gebildeten $(In,Ga)_2Se_3$-Schicht. Die Zusammensetzung des Absorbers wird während der zweiten Stufe Cu-reich ($[Cu]/([In] + [Ga]) > 1$). Neben der Änderung der Zusammensetzung wird auch Kornwachstum (oder Rekristallisation) und Defektannihilation angeregt. Daher ist die Untersuchung der Entwicklung der Mikrostruktur während der zweiten Stufe des CIGS-Wachstums sehr wichtig. In der Fachliteratur werden zu diesem Zweck zwei Methoden vorgeschlagen: *i)* die Untersuchung der Veränderung der Mikrostruktur von Diffusionspaaren während des Erhitzens; *ii)* *ex-situ* Vergleiche von Proben nach beendetem bzw. unterbrochenem Wachstum.

Im ersten Teil der vorliegenden Arbeit wurde eine Cu-arme ($[Cu]/([In] < 1$) $CuInSe_2$ (CIS) Vorläuferschicht mit einer $Cu_{2-x}Se$-Deckschicht präpariert und in einem Rastertransmissionselektronenmikroskop (STEM, engl. scanning transmission electron microscope) erhitzt, um die Rekristallisation nachzuahmen. Während der Cu-Diffusion von der Cu-reichen $Cu_{2-x}Se$-Phase in die Cu-arme CIS-Phase wurde das Wachstum von defektfreien Körnern zu Könen mit eng beieinander liegenden Gitterfehlern durch eine Dunkelfeldabbildung unter flachem Winkel (LAADF, engl. low-angle annular dark-field) beobachtet, wohingegen die Tiefenprofile der Elemente durch energiedispersive Röntgenspektroskopie (EDXS, engl. energy-dispersive X-ray spectroscopy), sowohl vor als auch nach dem Erhitzen, analysiert wurden. Hinweise auf einen erheblichen Einfluss des

Überschusses von Kupfer auf die Rekristallisation lieferte ein *in-situ* Experiment, bei dem eine Cu-arme CIS-Folie ohne eine $Cu_{2-x}Se$-Deckschicht erwärmt wurde und weder Kornwachstum noch Defektannihilation festgestellt wurden. Die Überwachung der Rekristallisation innerhalb der CIS-Absorptionsschichten wurde mittels STEM durchgeführt und lieferte direkte Nachweise für den vorliegenden Kornwachstums-Mechanismus.

Im zweiten Teil dieser Studie wurde ein durch Koverdampfung gewachsener CIGS-Absorber analysiert. Während des Wachstums war ein Teil der Probe in der zweiten Stufe, bevor die Rekristallisation einsetzte, entfernt worden. Das verbleibende Stück der Probe durchlief den dreistufigen Prozess. Die kompositionelle Charakterisierung der Defekte sowie die Tiefenprofilanalyse der Elemente wurden sowohl durch STEM-LAADF als auch durch EDXS durchgeführt. Ähnlich zu den Ergebnissen des *in-situ* Wärmeexperiments wurden weitaus größere Körner mit reduzierten Dichten an linearen und planaren ein- und zweidimensionalen Gitterfehlern in einer Absorptionsschicht gefunden, welche den Wachstumsprozess komplett durchlaufen hatte. Obwohl sich die meisten strukturellen Defekte nach der Rekristallisation aufgelöst hatten, wurden einige wenige strukturelle Defekte durch LAADF nach der Rekristallisation festgestellt und sogar nachdem der dreistufige Wachstumsprozess abgeschlossen war.

Weitere Analysen wurde mit einem C_s-korrigierten, hochauflösenden STEM in Kombination mit Elektronenenergieverlustspektroskopie (EELS, engl. electron energy–loss spectroscopy) durchgeführt, um die Art individueller Mikrostrukturdefekte in den unterschiedlichen Stufen des Wachstumsprozesses erklären zu können. Diese Untersuchungen legten die Beschaffenheit und chemische Zusammensetzung der Defekte offen, die sowohl in der Probe mit abgeschlossenen Wachstum, als auch in der mit unterbrochenem Wachstum zu finden sind: Σ3-Zwillingsgrenzen und Stapelfehler mit stöchiometrischer Elemente Verteilung, Korngrenzen, Neigungsgrenzen und Versetzungen mit Umverteilung der Kationen, d.h. Kupfer Anreicherung und Indium Abnahme. Stöchiometrische Inversionsgrenzen, Kupfer angereicherte, 'komplexe' zweidimensionale Gitterfehler und extrinsische Stapelfehler mit partiellen Frank-Versetzungen wurden nur in der Cu-armen Probe mit unterbrochenem Wachstum gefunden, wohingegen eine ‘sekundäre $Cu_{2-x}Se$-Phase’ nur in der Absorptionsschicht der Probe mit abgeschlossen Wachstum gefunden wurde.

Die vorliegende Arbeit liefert unmittelbare Einblicke in die Rekristallisation von CIGS-Absorbern und der Entwicklung von strukturellen Defekten, sowie eine ausführliche Untersuchung der individuellen strukturellen Defekte in CIGS-Absorbern.

Table of contents

This page intentionally left blank.

1. Introduction

1.1. A brief history of photovoltaics

The photovoltaic effect was first observed by a French physicist Alexandre-Edmond Becquerel in 1839.[1] He found that certain materials produced an electric current, when exposed to solar radiation. In 1873, Willoughby Smith, an English electrical engineer, discovered the photoconductivity of Se.[2] Smith showed that the electrical resistivity of Se varies, when it is exposed to light. Just after Smith's discovery, William G. Adams and Richard E. Day followed up his discovery, and observed an electrical current by illuminating a Se-Pt junction.[3] Shortly thereafter, Charles Fritts designed a solar cell, using Se on a metal plate and coating the structure with a thin layer of Au.[4] This first solar cell had a power-conversion efficiency of 1%. After almost 70 years, in 1954, Chapin *et al.* successfully built the first silicon solar cell with 6% power-conversion efficiency at the Bell Laboratories.[5] The first application area for the solar cells was space industry, *i.e.* satellites, at the beginning of the 1960s. In the 1970s, the oil crisis accelerated the research on solar cells for terrestrial applications. Since the 1970s, as new materials are discovered and synthesized, the efficiencies have steadily increased and the production costs decreased.

1.2. Classification of solar cells

The traditional classification of photovoltaic materials is depicted in Figure 1.1. According to this classification, the single-crystalline and multi-crystalline Si belong to the first generation solar cells. Although single-crystalline Si still has the highest efficiency, it has higher production cost. The energy payback time (EPBT) of single-crystalline Si is around three years.[6, 7] The EPBT is the time span that the solar cell needs to operate until it generates the amount of energy that compensates its production. For the multi-crystalline Si, the EPBT is low compared to single-crystalline Si; however, the efficiencies are also lower.[8, 9]

The second generation solar cells include $Cu(In,Ga)Se_2$ (CIGS), CdTe and amorphous Si (a-Si) thin-films. The material usage and the production cost are much lower for the second-generation solar cells compared to the first generation.[9-11] Therefore, the EPBT is much lower –around one year– for the second generation solar cells.[6] Another advantage of thin-film solar cells is the flexibility, when they are fabricated on flexible polymeric substrates. Two main concerns about the second generation solar cells are their toxicity especially in the case of CdTe, and the scarcity of Te, In and Ga for both CdTe and CIGS solar cells, respectively.

However, separation and high purity recovery of the elements is possible for the CIGS solar cells.[12]

In third generation solar cells the focus is to produce lower cost and higher efficiency solar cells by using alternative materials or producing tandem (multi-layer) structures. The perovskite solar cells are the most popular among third generation solar cells, because of the rapid increase in their demonstrated efficiencies. From 2009 to 2017 their power-conversion efficiencies increased from 4% to 22.7%. However, long-term stability issues and the lead content are the limiting factors for perovskite solar cells.[13-15]

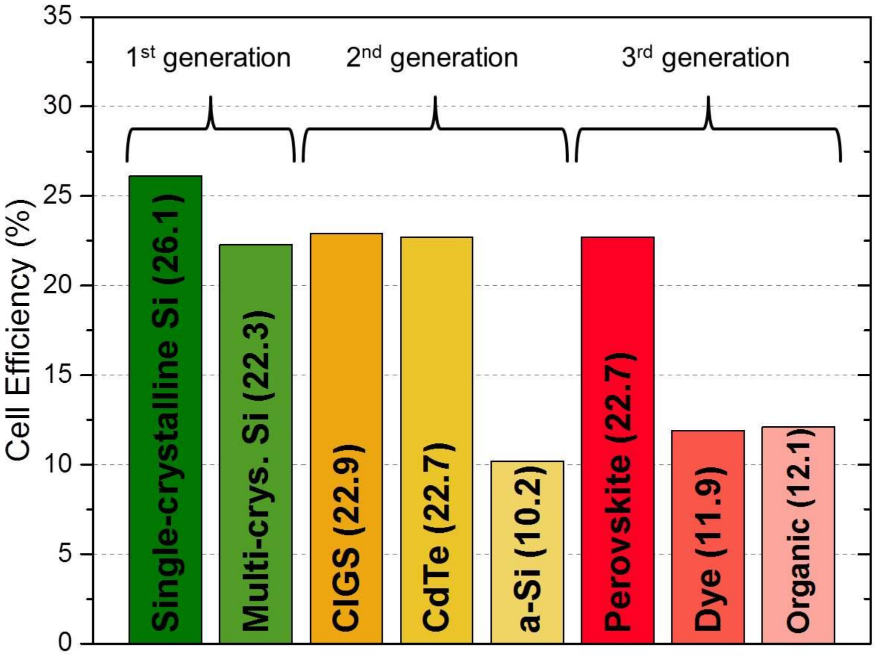

Figure 1.1 Comparison of highest 'cell' efficiencies at the laboratory for various solar cells. The data used here is taken from the National Renewable Energy Laboratory`s (NREL) Best Research-Cell Efficiencies chart plotted on 25.04.2018, and modified with Solar Cell Efficiency Tables (version 51) written by Green *et al.* [16] for a-Si and organic solar cells. The efficiency of CIGS is modified according to new achievement of Solar Frontier on CIS based absorbers.[17]

1.3. The scope of this thesis

Microstructural defects present in the CIGS absorbers may alter the optoelectronic properties of final devices. Therefore, a thorough understanding and control of microstructural defects are crucial for high-performance solar cells. In the scope of the present thesis, the microstructural evolution of the CIGS absorbers was analyzed using scanning transmission electron microscopy (STEM). Two methods were used to investigate the evolution of the defects during the recrystallization: *i)* preparation of diffusion couples followed by *in-situ* heating, *ii)* interruption of the growth process.

STEM imaging and spectroscopy techniques were employed for specific purposes. Low-angle annular dark-field (LAADF) imaging was used for the observation of defect concentrations as well as grain growth and defect annihilation during the *in-situ* heating analyses. Energy-dispersive X-ray spectroscopy (EDXS) was used to determine the elemental distributions along absorber layers. Finally, the structure and composition of individual microstructural defects were investigated using high-angle annular dark-field (HAADF) imaging in combination with electron energy-loss spectroscopy (EELS).

The present thesis is organized as follows:

In the second chapter, the properties and fabrication of the CIGS absorbers/solar cells are provided.

In the third chapter, an overview of STEM imaging and spectroscopy techniques and a sample preparation technique (focused ion beam (FIB)) are given. Additionally, Geometric Phase Analysis (GPA), an advanced image analysis procedure, is introduced briefly.

In the fourth chapter, results on the evolution of microstructural defects during the growth of CIGS absorbers as well as the structural and chemical nature of these defects are shown and discussed in detail.

In the fifth chapter, concluding remarks on the results discussed in the previous chapter and an outlook are given.

This page intentionally left blank.

2. The material system

2.1. An overview on Cu(In,Ga)Se$_2$ thin-film solar cells

The optical and electrical properties of materials are determined by their energy band structure. A material has a direct band gap, when the maximum energy state of its valence band and the minimum energy state of its conduction band happen to be at the same crystal wave vector value. Owing to its direct band gap nature, CuInSe$_2$ (CIS) has a high absorption coefficient of 10^5 cm^{-1}, hence a thickness of 2 to 3 µm of CIS is typically enough for solar cell applications.[18] The drawback of CIS is its low band gap of 1.02 eV[18]. This is because most of the photons reaching the Earth's surface (the air mass coefficient of 1.5– AM 1.5) have energies greater than that. The optimum band gap for a solar cell has been estimated to be 1.4 eV.[19] Therefore, CIS solar cells are alloyed with CuGaSe$_2$ (CGS), a direct band gap semiconductor with a band gap of 1.69 eV[20], allowing for bandgap engineering by varying the Ga content.[21] By increasing the amount of Ga in the CIS, the valence band maximum (VBM) decreases slightly; however, the conduction band minimum (CBM) increases significantly.[22] Hence, the band gap increases with increasing Ga amount. The highest efficiency of CuIn$_{(1-x)}$Ga$_x$Se$_2$ devices were obtained at $0.3 < x < 0.4$, where the band gap value is about 1.2 eV (Figure 2.1).[23, 24] During the growth of CuIn$_{(1-x)}$Ga$_x$Se$_2$, a Ga gradient is formed along the depth of the absorber. The reason for and the results of a grading band gap will be discussed in sub-section 4.2 in more detail.

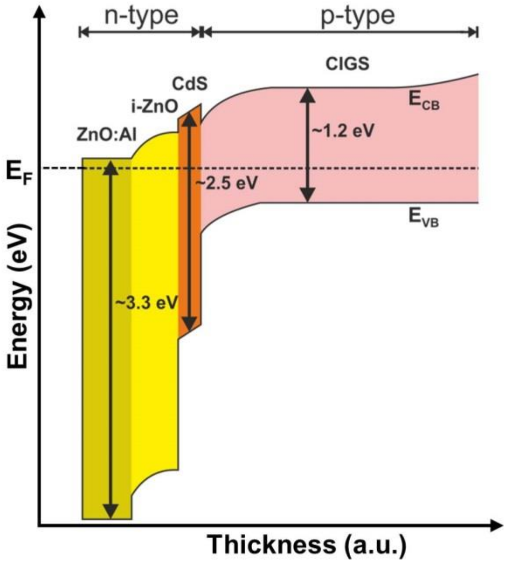

Figure 2.1 An equilibrium band diagram of a CIGS thin-film solar cell.

2.2. Fabrication of CIGS solar cells

A cross-section of a working CIGS solar cell, similar to the samples that were used in this study, is shown in Figure 2.2. It should be mentioned that the samples were processed as they would be to fabricate fully working solar cells, although for the present study the process did not continue with the deposition of the buffer and window layers.

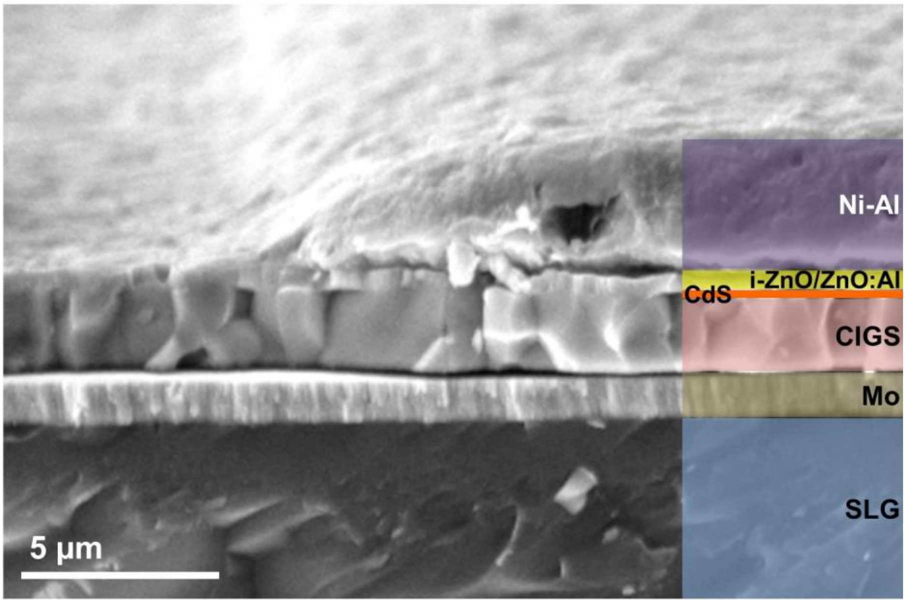

Figure 2.2 A secondary electron image from a fractured cross section of a CIGS solar cell.* The soda-lime-glass substrate, Mo back-contact layer, CIGS absorber, CdS buffer layer, i-ZnO/ZnO:Al window layer and the Ni-Al metal grid are shown by transparent colors on the scanning electron microscopy (SEM) image.

A rigid soda-lime glass (SLG) was selected as a substrate material in this study. For space or building applications, polymeric or metallic substrates can also be selected to make the solar cells flexible.[25] The low growth temperature of the CIGS absorbers becomes essential, if polymeric substrates are chosen.

Polycrystalline Mo with a thickness of between 0.5–1 µm is deposited by a direct current sputtering method, and it serves as a back contact.

The CIGS absorbers used in the highest-efficiency solar cells are produced via a three-stage co-evaporation technique, which is summarized in Figure 2.3.[26, 27] The same technique is used for the growth of CIGS and/or CIS (CI(G)S) absorbers characterized in this study. In the three-stage co-evaporation technique, the first stage starts with alternating In-Se and Ga-Se deposition on the Mo-coated SLG. In the second stage, Cu is evaporated in Se atmosphere. At this stage, the stoichiometry of the absorber changes from Cu-poor ([Cu]/([In] + [Ga]) < 1)

---

* The image was acquired by Ms. Sabine Kühnemann.

to Cu-rich ([Cu]/([In] + [Ga]) > 1), which is essential for recrystallization, grain growth and defect annihilation, hence better crystal quality.[28-34] The Cu-poor to Cu-rich transition also improves the electronic properties of the absorber.[32, 35] However, according to the binary phase diagram of Cu_2Se-In_2Se_3 (Figure 2.4) a Cu-rich stoichiometry is known to lead to the formation of a secondary phase, $Cu_{2-x}Se$ (x = 0–0.25). This secondary phase forms at the absorber surface and at grain boundaries (GBs) within the film.[34, 36-38] Due to its conductive nature, excess $Cu_{2-x}Se$ can be detrimental to the performance of the solar cell.[27, 37] Similarly, $Cu_{2-x}Se$ on the surface can cause high recombination loses at the interface between the CIS and CdS.[35, 39] This undesired secondary phase is consumed during the third stage by simultaneous In, Ga and Se deposition, and a slightly Cu-poor composition is reached at the surface of the absorber. At the end of the third stage, the absorber layer reaches the desired Cu composition of about [Cu]/[In] + [Ga]) ~ 0.8, where there is only an α-chalcopyrite single-phase present according to the phase diagram. The chalcopyrite phase is present in a very narrow region in the phase diagram, and the region gets narrower at lower temperatures.[40] However, Na doping and/or Ga alloying has been found to suppress the formation of ordered defect compounds, *i.e.* β-$CuIn_3Se_5$, and to increase the width of the chalcopyrite single-phase region, respectively.[22, 41]

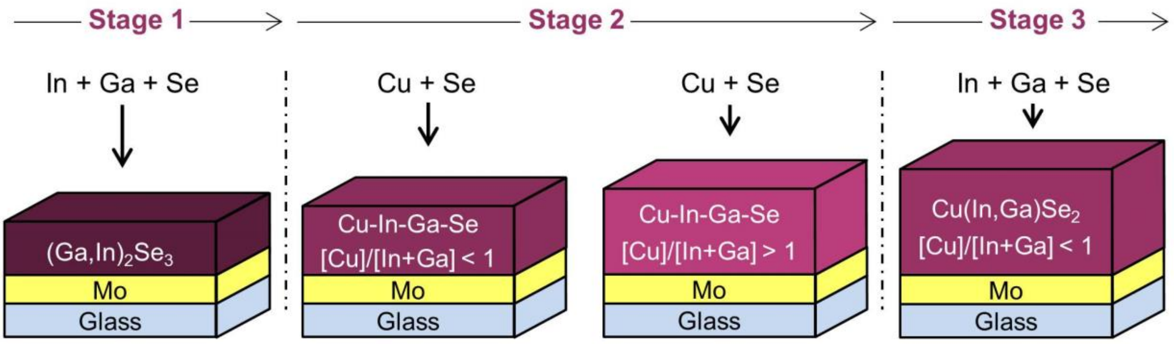

Figure 2.3 A schematic drawing of the three-stage co-evaporation technique.

After deposition of the absorber layer, a 50 nm n-type CdS buffer layer, with a band gap of 2.5 eV, is deposited by a chemical bath deposition technique. A window layer consisting of an n-type intrinsic-ZnO (i-ZnO) and Al-doped ZnO (ZnO:Al) layers with a band gap of ~ 3.3 eV are deposited by radio frequency magnetron sputtering. The total thickness of this layer is about 0.5 µm. Finally, a Ni-Al metal grid is deposited by electron beam evaporation on top of the window layer.

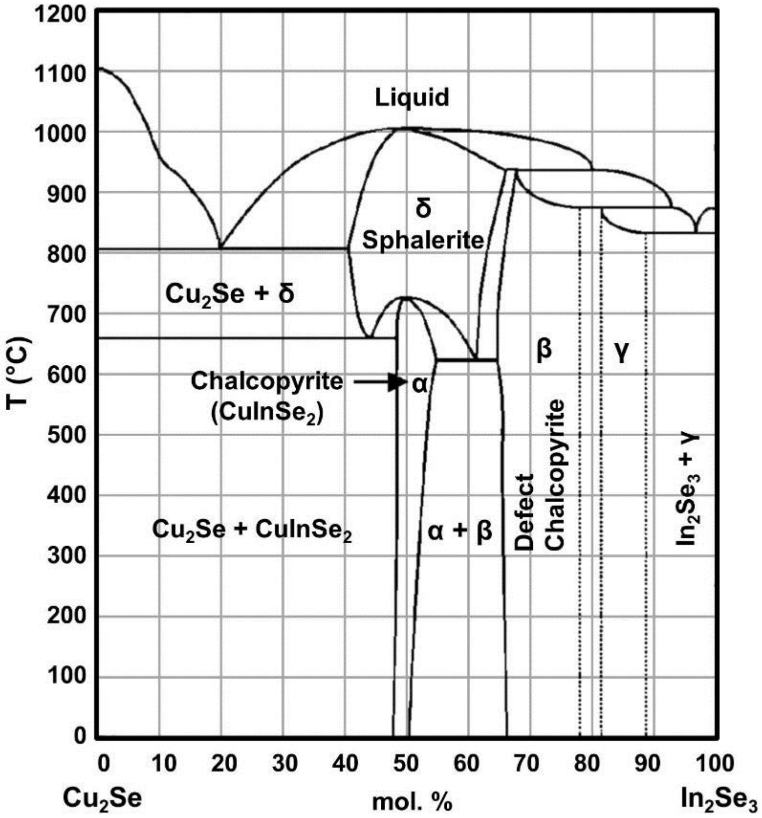

Figure 2.4 Binary Cu_2Se-In_2Se_3 equilibrium phase diagram. The phase diagram is reprinted from J. S. Park *et al*. Journal of Applied Physics 87, 3683 (2000), with the permission of AIP Publishing.[40] Similar to the ternary CIS (α) phase shown in the binary phase diagram, for the quaternary CIGS phase the evolution of the phases occurs as follows: at the first stage γ-$(In,Ga)_2Se_3$ is formed; with the increasing amount of Cu at the second stage γ-$Cu(In,Ga)_5Se_8$ → β-$Cu(In,Ga)_3Se_5$ → α-$Cu(In,Ga)Se_2$ → $Cu_{2-x}Se$ + α-$Cu(In,Ga)Se_2$ are formed sequentially, and finally at the third stage $Cu_{2-x}Se$ is consumed and only α-$Cu(In,Ga)Se_2$ remains.

2.3. Alkali effect on the CIGS solar cells

The beneficial effect of Na incorporation into the CI(G)S was discovered almost three decades ago by chance.[42] When the CI(G)S absorber was directly deposited on SLG, it showed morphological differences, such as a highly textured structure and a change in grain size; as a result, the solar cell made using these absorbers showed better photovoltaic performance. In the literature, the effect of Na on the CIGS solar cells, including an increase in hole concentration, p-type conductivity as well as in open circuit voltage (V_{oc}) and fill factor (FF), are intensively discussed.[42-44] Several explanations are given for the increase in hole concentration and p-type conductivity: *i)* the occupancy of Cu sites with Na and a reduction in the number of In_{Cu} antisites, which act as donors[41, 45]; *ii)* an increase in the concentration of Na_{In} antisites, which act as acceptors[44]; *iii)* at the GBs, a passivation of V_{Se} by the activation of atomic O.[46] These are true for low Na concentrations; however, a high Na concentration removes the acceptors and reduces the hole density, thus deteriorating the performance of the cell.[41, 47] To prevent uncontrolled Na diffusion into the CIGS, a SiN thin film is deposited as a Na barrier on the SLG in this study. To incorporate a controlled amount of Na into the CI(G)S deposited on SLG with the Na barrier, or on polymeric and metal substrates, several methods were developed: *i)* the deposition of precursor layers on Mo before the CIGS deposition[48], *ii)* a post-deposition treatment after the CIGS deposition[49], *iii)* the co-evaporation of Na during the growth of CIGS[50], and *iv)* the use of a Na-containing Mo back-contact layer[51]. The incorporation of Na was done via evaporation of a NaF precursor layer on the Mo-coated SLG before the deposition of CIS samples in the present work.

Investigations on the effects of other alkali metals, such as K, Rb, Li and Cs in the CIGS solar cells increased in recent years.[52-56] The best solar cell up to date is produced by a RbF post-deposition treatment.[26] In this study, other alkali metals were not used and therefore will not be discussed in detail.

2.4. Crystal structure of CIGS

The ternary CIS, CGS and the quaternary CIGS compounds crystallize in the chalcopyrite (Figure 2.5) structure, which is named after the mineral chalcopyrite, $CuFeS_2$.[57] The chalcopyrite structure is a tetragonal structure, which can be derived from the sphalerite structure by an ordered substitution of Zn^{2+} with Cu^{+} and In^{3+}/Ga^{3+} cations.[58] Substitution of the divalent (Zn) cation with monovalent (Cu) and trivalent (In, Ga) cations, doubles the period of the unit cell along the [001] direction, and the space group becomes $I\bar{4}2d$.[58] In the chalcopyrite structure, monovalent cations sit on the 4a (000) and trivalent cations sit on 4b $(00\,{}^{1}/_{2})$ positions, and they are tetrahedrally coordinated with Se on the 8d $(0\ {}^{1}/_{4}\,{}^{1}/_{8})$ positions.[57] Due to the different bonding lengths of monovalent and trivalent cations with Se, some amount of tetragonal distortion $({}^{c}/_{a} \neq 2)$ is present in the lattice.

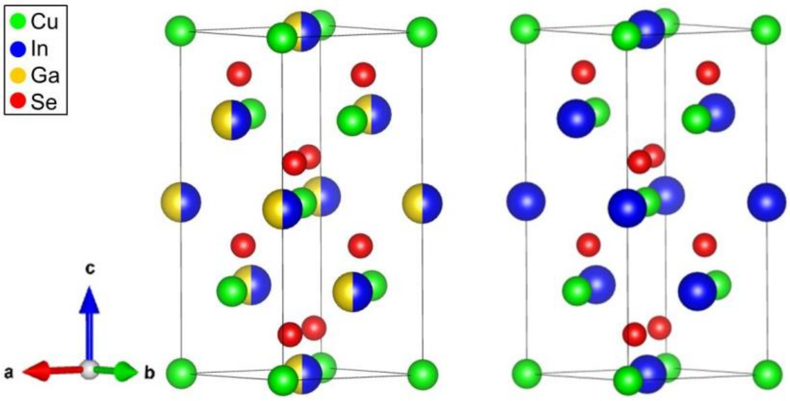

Figure 2.5 Unit cells of CIGS (left) and CIS (right) crystallize in chalcopyrite structure.

This page intentionally left blank.

3. Experimental methods

Thanks to tremendous advancements in monochromators, correctors, energy filters and detectors, the importance of TEM in materials characterization is ever growing. Currently, state-of-the-art TEMs achieve a spatial resolution below 1 Å and an energy resolution below 10 meV.[59] The ability to simultaneously analyze structural defects, chemical composition, electronic structure and atomic bonding makes TEM an essential tool for many applications, including solar cells research.

3.1. Electron matter interaction

Incident electrons scatter upon interaction with the atoms of a sample. Several scattering phenomena, as well as the formation of secondary signals, are depicted in Figure 3.1. Most of the signals shown above the sample are used in scanning electron microscopy (SEM). In SEM, most frequently used signals are secondary electrons and backscattered electrons that give information on topography and composition of the samples, respectively.

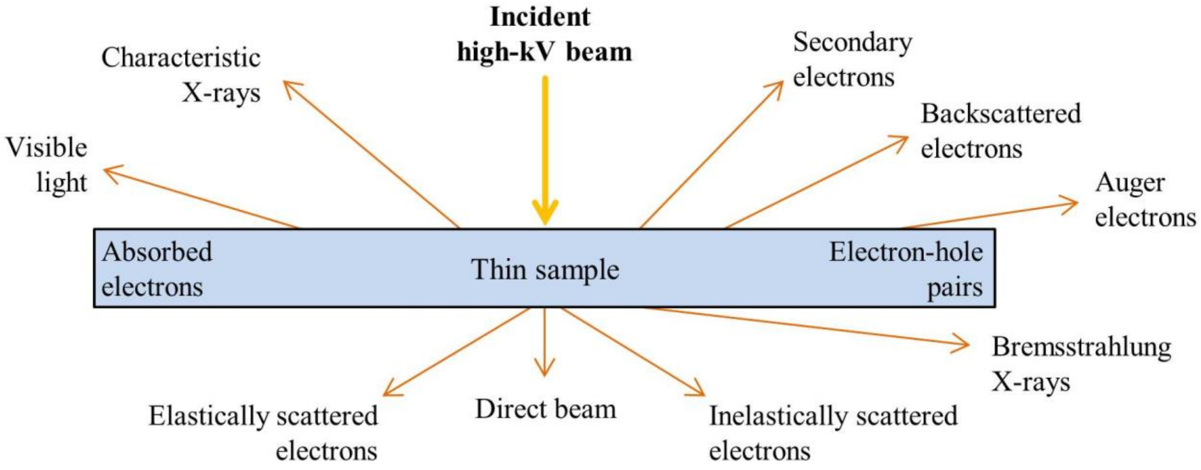

Figure 3.1 Electron beam matter interaction. The figure is adapted by permission from Springer: Transmission Electron Microscopy: A Textbook for Materials Science by D. B. Williams and C. B. Carter (1996)[60].

Electrons exhibit characteristics of both particles and waves. Elastic or inelastic scattering of electrons can be explained considering their particle nature, and coherent or incoherent scattering considering their wave nature. Elastically scattered electrons are considered to conserve their kinetic energies. If the electrons lose some of their energy, they are considered to be inelastically scattered. Generally, if the sample is thin and crystalline, elastically scattered electrons are considered coherent and inelastically scattered electrons incoherent.[60]

Beam energy, atomic mass, thickness and crystallinity of the sample are factors that can affect the scattering event. Scattering and the beam energy are inversely correlated, whereas the amount of scattering is typically proportional to atomic mass and thickness of the sample. If the thickness of the sample increases, multiple scattering increases, which reduces the signal-to-noise ratio (SNR), in particular in imaging, and may complicate the evaluation of the results. With further increasing the thickness, most of the incident electrons start to backscatter; therefore it is important to have thin samples for TEM analyses.

3.2. Conventional and scanning transmission electron microscopy

A TEM consists of an electron gun, multiple electromagnetic lenses, a sample stage and several detectors for various purposes. An electron beam is generated and accelerated out of the electron gun through the application of a high voltage. The acceleration voltages of TEMs can be as low as 20 kV and as high as 3 MV; however, more typically the values range from 60-300 kV.[61] Although there are different types of electron guns, owing to their high brightness (10^{13} A/m^{2}sr at 100 kV) and low energy spread (~0.3 eV at 100 kV) field emission guns (FEG) are used commonly.[60] Condenser lenses demagnify the gun crossover and manipulate the beam convergence, which can also be restricted by a condenser aperture. There are two main modes of TEM, conventional TEM (CTEM) and scanning TEM (STEM). In Figure 3.2 simple schematics of CTEM and STEM are given. The main difference between the two modes is, that in CTEM the sample is illuminated with a close-to-parallel beam and the objective lens forms an image and a diffraction pattern, at the image plane and the back focal plane, respectively. In CTEM either the image or the diffraction pattern is selected and magnified by intermediate lenses. Further magnification is done by the projector lens system. Whereas in the STEM mode, the condenser lens and a probe-forming lens focus the beam and form a fine probe onto the sample. The scanning coils deflect the probe along the X and Y axes, and the sample is scanned in a raster. Unlike CTEM, in STEM mode, in principle, no imaging lenses are needed, as the scattered electrons are collected directly by circular and annular detectors, although post-specimen lenses are often used to provide additional flexibility.

In the scope of this thesis, all microscopes are operated mostly in STEM mode. In STEM mode, the resolution is limited by the probe size, which is determined by the condenser lenses. Electromagnetic lenses suffer from aberrations, particularly spherical and chromatic aberrations. The presence of aberrations results in a blurred illumination and hence a reduced spatial resolution. Aberrations arise due to the deviation of the electrons from their ideal trajectory; in the case of spherical aberration, for instance, the electrons far from the optical axis are focused more strongly than those travelling closer to the optic axis. The energy spread of the emitted electrons causes chromatic aberrations; the electrons with higher energies are deflected less than the ones with lower energies. Scherzer discussed the aberrations of the electromagnetic lenses and later proposed a route to correct the spherical and chromatic aberrations.[62, 63] To correct the electromagnetic lens aberrations, non-round lenses were developed and tested for a long time before their successful application in SEM, TEM and STEM in the 1990s.[64-66] An aberration corrector is formed by the alignment of several non-round lenses in a well-defined order, designed to counteract the natural optical aberrations of the main, round, focusing lenses. These non-round lenses are named after their rotational symmetries. There are two main types of aberration correctors, which are known as *i)* quadrupole-octupole and *ii)* hexapole correctors. By use of aberration correctors, spatial resolution at the Å level was achieved soon after their implementation to the TEMs in the 1990s.

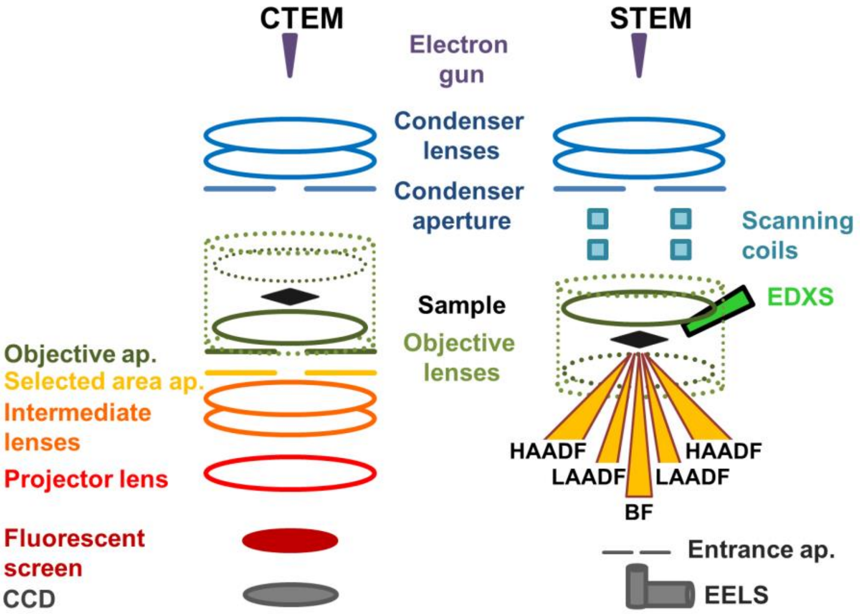

Figure 3.2 Simple schematics of CTEM and STEM

3.3. Imaging in STEM

The fine probe is scanned over the sample, and scattered electrons are collected by various detectors. The intensity of the scattered electrons is plotted as a function of the probe position, and the image is built up serially.[60]

In STEM mode, transmitted electrons, including electrons scattered at very low-angles, are collected by a circular detector to give a bright field (BF) image. The contrast mechanism of BF imaging is mainly phase contrast, which is strongly affected by the microscope defocus and thickness of the sample. Hence, the direct interpretation of STEM-BF images is difficult at atomic resolution, and typically rely on further image simulations.[67] Additionally, the BF detector is located on the optical axis, and therefore precludes analysis using EELS; hence simultaneous analytical measurements can only be done via EDXS. In contrary, using annular dark-field (ADF) detectors, simultaneous imaging and spectroscopy with both EDXS and EELS become possible.

Annular detectors are ring-shaped with a hole in the middle to allow the detection of transmitted electrons either for BF imaging or EELS. Depending on the angular range (inner and outer angles) of the annular detectors, various electrons contribute to the image formation to give rise to a specific contrast. Incident electrons are elastically scattered from the atomic nuclei at high angles due to the Rutherford scattering.[60] When the ADF detector collects mostly such electrons, the image is called a high-angle annular dark-field (HAADF) or a Z-contrast image, because the intensity of the image is then proportional to atomic number, $\sim Z^{1.7}$.[60, 68] Thermal diffuse scattering (TDS) is an incoherent scattering process, which is caused by thermal lattice vibrations. It creates a diffuse background and suppresses the higher order Bragg reflections (diffraction contrast), and enhances the Z-contrast.[60, 69] The interpretation of high-resolution STEM (HR-STEM) images is relatively straightforward in crystalline samples. The bright intensity comes from the channeling of the electrons along the atomic columns in the crystal, when the probe is located on the atomic column.[68] Enhanced channeling increases also the probability of Rutherford scattering by keeping electrons traveling close to the atomic nuclei.

Structural defects disrupt the ordered lattice, create strained regions and affect the channeling behavior of the electrons.[68] Low-angle scattering occurs due to de-channeling of the incident beam in strained regions around the defects. Thus the collection of low-angles scattered electrons by an ADF detector with a smaller inner angle allows large-scale imaging of defects in crystalline samples.[70] The image is then called a low-angle annular dark-field (LAADF) image.

In order to record the desired image contrast, the angular range of the detector can be set simply by changing the camera length of the microscope. An example is shown in Figure 3.3 (a-h). The detector inner semi-angles are varied from 44 mrad (180 mm camera length) to 11 mrad (720 mm) and 6 mrad (1440 mm) to give HAADF, LAADF and BF contrast, respectively.

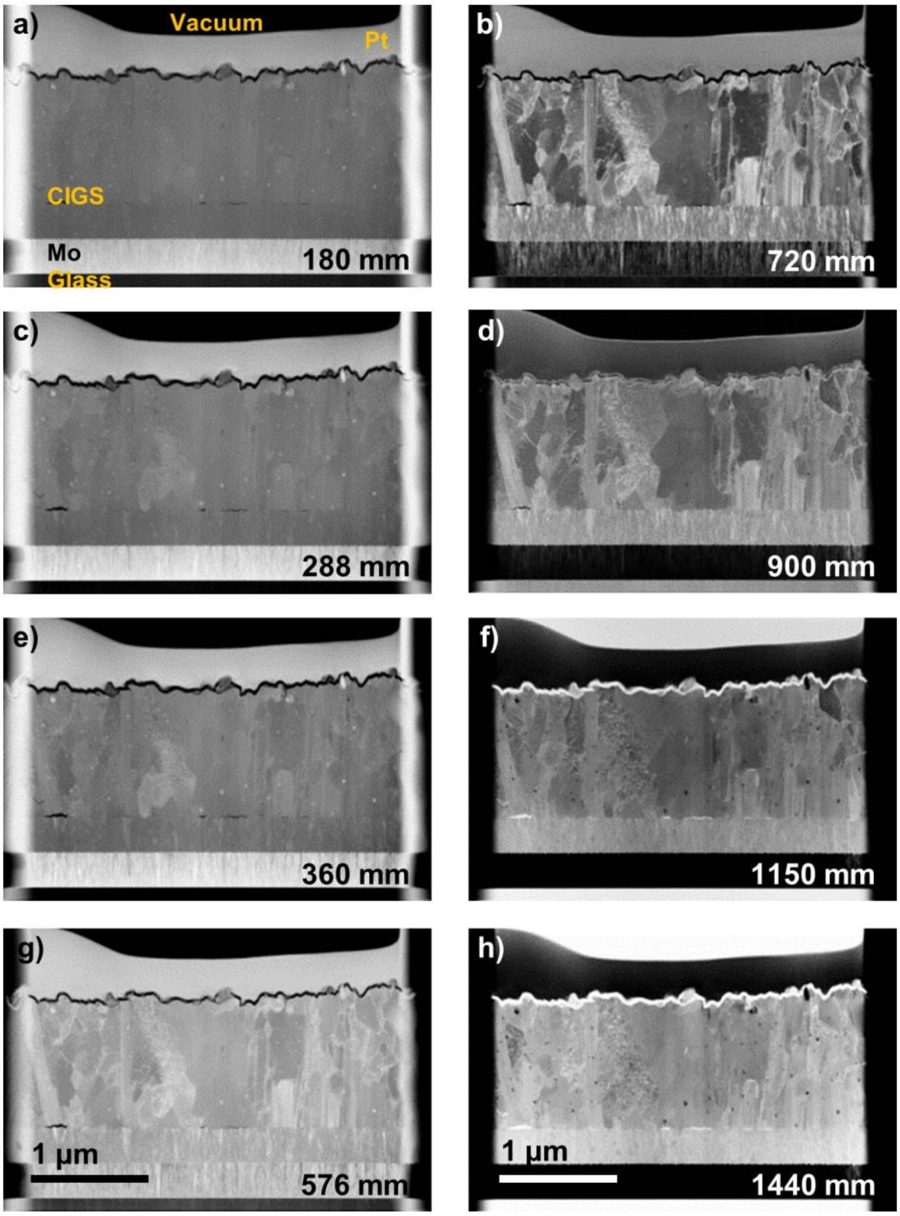

Figure 3.3 (a-h) ADF images with increasing camera lengths (decreasing collection angles) are shown. The images are acquired using an uncorrected microscope at 200 kV. The convergence semi-angle is 7 mrad, whereas the detector inner semi-angles are varied from 44 mrad (180 mm camera length) to 6 mrad (1440 mm camera length).

3.4. Analytical techniques

The scattered electrons and secondary signals are not only used for imaging but also for chemical and electronic structure analysis of the materials. The interaction of the incident beam with the electrons of the atoms is the main mechanism exploited for spectroscopy. Here two of those techniques used in this work, EELS and EDXS, will be discussed. The incident electrons lose energy, when they interact with the atomic electrons of the sample. The EELS detector acquires those electrons as a function of their specific energy loss, whereas EDXS detector collects the X-rays released during the de-excitation of the atoms. A schematic overview of the excitation and de-excitation processes is shown in Figure 3.4.

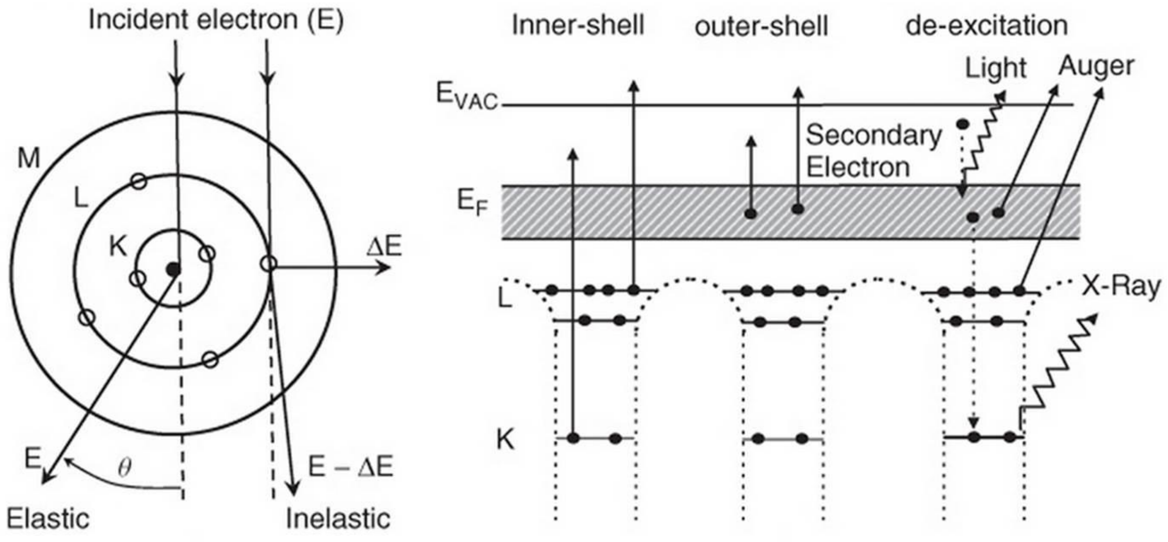

Figure 3.4 Left: Elastic and inelastic scattering are shown schematically. Right: An energy-level diagram showing inelastic excitations. The figure is reprinted by permission from Wiley & Sons, Inc.: Low Voltage Electron Microscopy: Principles and Applications by D. C. Bell, N. Erdman (2012)[71].

3.4.1. Electron energy-loss spectroscopy

Incident electrons can be inelastically scattered from the inner or outer-shell electrons of the atoms in the sample. A specific amount of their kinetic energy is then transferred to the inner- and outer-shell electrons of the atoms. The transferred energy is specific to the element and atomic orbital to/from which the transition takes place. Thus, EELS gives information about the composition, chemical bonding and electronic structure of the materials.

The inelastically scattered electrons are collected by an EEL spectrometer. The electrons are bent in the spectrometer by a magnetic prism depending on their energy, and the energy-dispersed spectrum is formed in the dispersion plane of the spectrometer.[60] An example of an EEL spectrum of CIS is shown in Figure 3.5, which displays the electron counts (referred to as the intensity) as a function of energy loss.

The EEL spectrum consists of three parts: the zero-loss peak, the loss-loss region and the core-loss region. The zero-loss peak (ZLP) is the most intense feature of the EEL spectrum, especially for very thin samples as the probability of multiple scattering is very low. It mainly consists of electrons, which undergo elastic scattering (as well as those that do not interact with the sample at all); therefore, their energy is almost equal to the incident beam energy. The ZLP also includes the quasi-elastically scattered electrons, *i.e.* those that have contributed to the creation of phonons.[72] The width of the ZLP and its intensity relative to the rest of the spectrum are used to extract information about the energy resolution of the system and thickness of the sample, respectively.

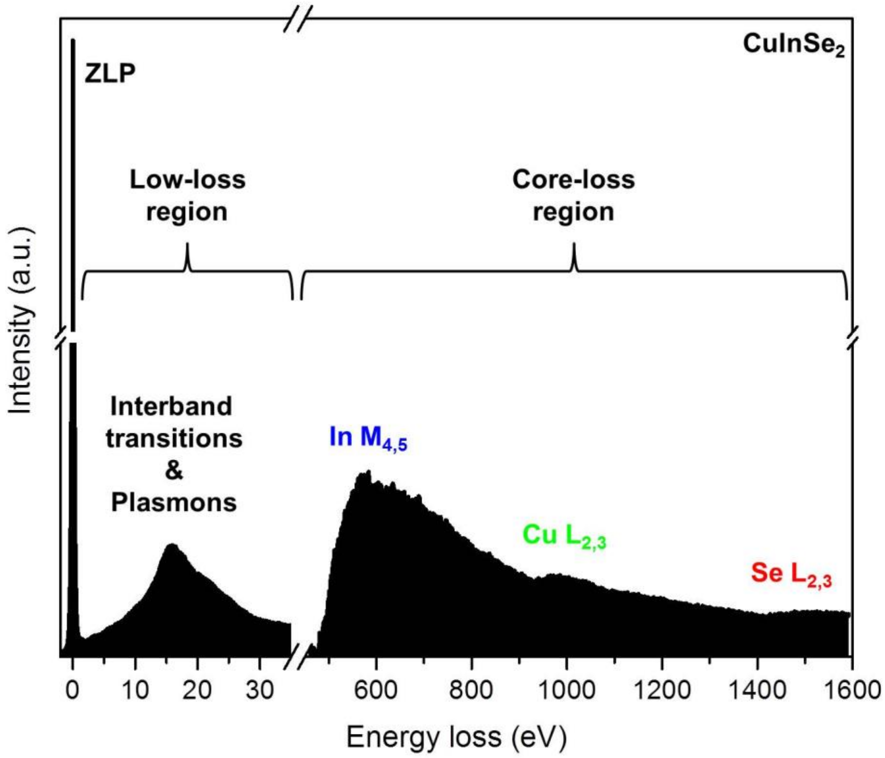

Figure 3.5 An example EEL spectrum of $CuInSe_2$. Different experimental data are used for the low-loss and core-loss parts. The background was subtracted for the core-loss region to show the delayed In, Cu and Se edges.

The low-loss region extends up to ~50 eV. It contains electrons that have interacted with weakly bonded outer-shell (valence and conduction band) electrons. Therefore, it gives information about the electronic and optical properties of the materials. The low-loss region's most dominant feature typically consists of peaks due to plasmon excitations, which are collective electron oscillations in the material.[73] Interband transitions are also detected in the low-loss region.[73] The most simple case of which are single electron transitions from the valence band to the unoccupied states in the conduction band, thus providing a means of estimating the band gap of the material. There is no interband transition allowed below the band gap energy of insulators and semiconductors.

The core-loss (high-loss) region extends from ~50 eV to a few keV. The incident beam excites the inner-shell (denoted K, L, M, etc…) electrons to the unoccupied energy levels above the Fermi level (E_F) of the sample and the atoms are ionized. The energy loss in this region is therefore intimately linked to the binding energy of the excited electrons.[74] Hence the ionization edges and their intensities are used to determine the chemical composition of the sample. The thickness of the sample is a critical parameter for the quantification of the

EEL spectra. As the thickness of the sample increases, the background intensity increases due to multiple scattering. Inelastic scattering from electrons with lower binding energy is another reason of the superimposed background at ionization edges. For qualitative and quantitative EELS analysis, the background has to be subtracted from the spectrum.[73]

Electrons of the atoms are excited from different orbitals, which are used in classifying the ionization edges, e.g. K excitation for ionization of $1s_{1/2}$ electrons from the K shell, L_1 for $2s_{1/2}$, L_2 for $2p_{1/2}$ and L_3 for $2p_{3/2}$ electrons from the L shell.

In this study, EEL spectrum images (SIs) were acquired from carefully selected regions of interest on the sample. Figure 3.6 (a) shows an example HAADF image with a selected region for spectrum image acquisition and (b) an acquired SI. A SI is a data cube formed as the probe is scanned over the selected area on the sample. The X and Y axes of the data cube represent the spatial information about the probe position, while Z axis represents the energy-loss spectrum acquired at each data point. The one-dimensional version of this technique, called EELS line scans, was also applied in this work. ADF detectors allowed simultaneous image acquisition during the SI acquisition. An example of a simultaneously acquired HAADF image is shown in Figure 3.6 (c). After the acquisition of a SI, it is processed using the Multivariate Statistical Analysis (MSA)[75] plug-in for Digital Micrograph (DM), based on the weighted principal component analysis (PCA), to reduce noise. The PCA procedure starts by decomposition of the 2D data matrix.[75] A scree plot is generated after PCA decomposition.[75] It gives a logarithm of the eigenvalues against the index of components.[75] Figure 3.7 shows an example scree plot, which was generated after PCA decomposition of the SI shown in Figure 3.6 (b). To distinguish principle components (data represented in the graph with high eigenvalues) from the noise (with lower eigenvalues) a number of components can be evaluated.[75] Figure 3.8 shows six individual components with extracted spectra (spectral features) and corresponding score images (spatial amplitudes). The first component indicates the average spectrum of the selected SI; other components indicate the difference from the first component; hence they contain positive and negative regions. Evaluation of the individual components in Figure 3.8, suggests that the last principle component is the fourth component. A SI with reduced noise was then reconstructed by using the four principal components. The presented components 5 and 6 mainly represent noise. Figure 3.9 shows the difference between the original and the reconstructed SI and extracted Se elemental maps. In order to extract the elemental maps, the background was subtracted using a power-law fit. A background window of ~50 eV in the pre-edge region and an integration window of ~80 eV were selected to extract the Se elemental map. Same background and integration windows at same positions were used to compare the Se elemental maps before and after PCA. The same procedure was also applied to extract elemental maps of cations in the course of the present study. For the CI(G)S samples analyzed in this study, elemental distribution maps/lines were extracted from the EEL spectra based on In $M_{4,5}$-edges at 443 eV, Cu $L_{2,3}$-edges at 931 eV, Ga $L_{2,3}$-edges at 1115 eV and Se $L_{2,3}$-edges at 1436 eV.

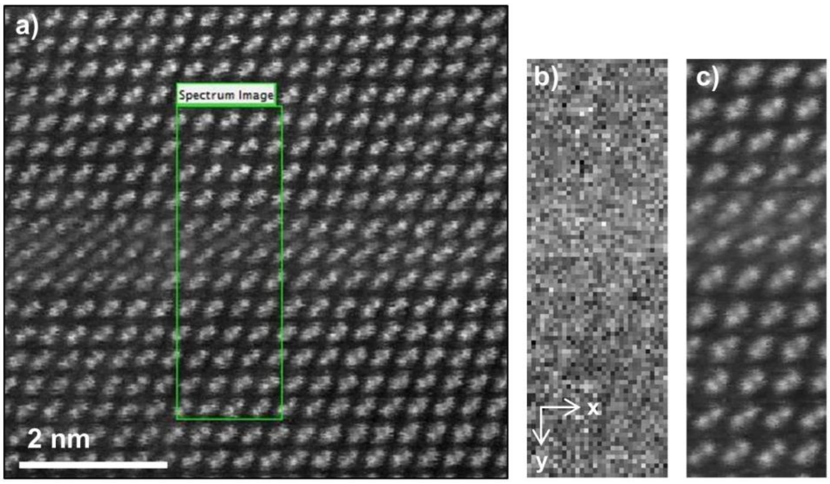

Figure 3.6 (a) HAADF image with a selected region for SI acquisition; (b) SI acquired from the selected region; (c) simultaneous HAADF image acquired during the SI acquisition.

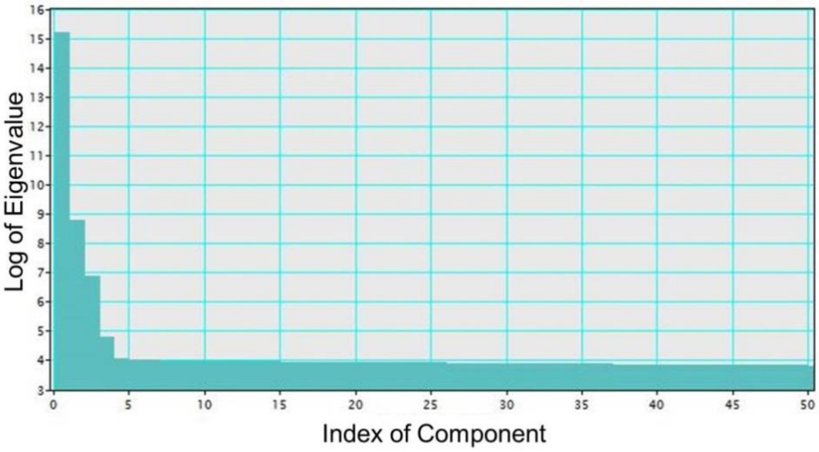

Figure 3.7 The scree plot generated after PCA decomposition of the SI shown in Figure 3.6 (b).

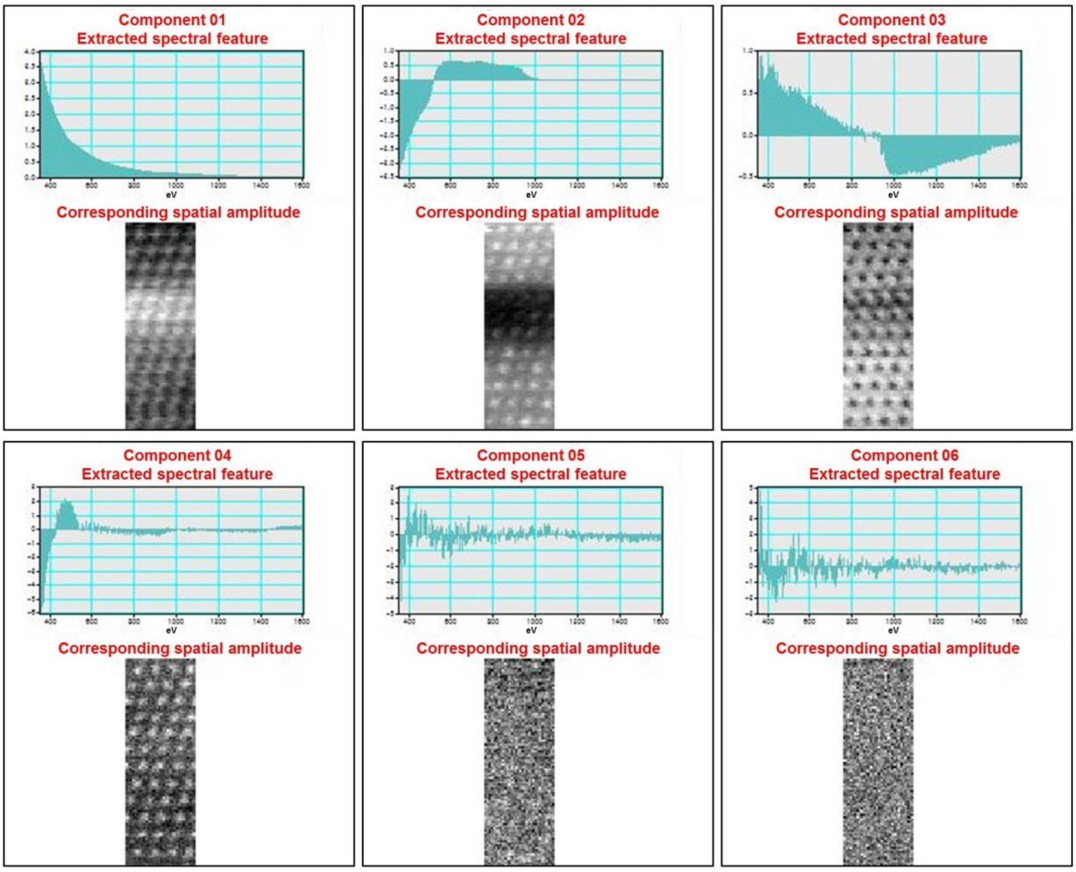

Figure 3.8 Extracted spectra and corresponding score images from the six components of the SI shown in Figure 3.6 (b).

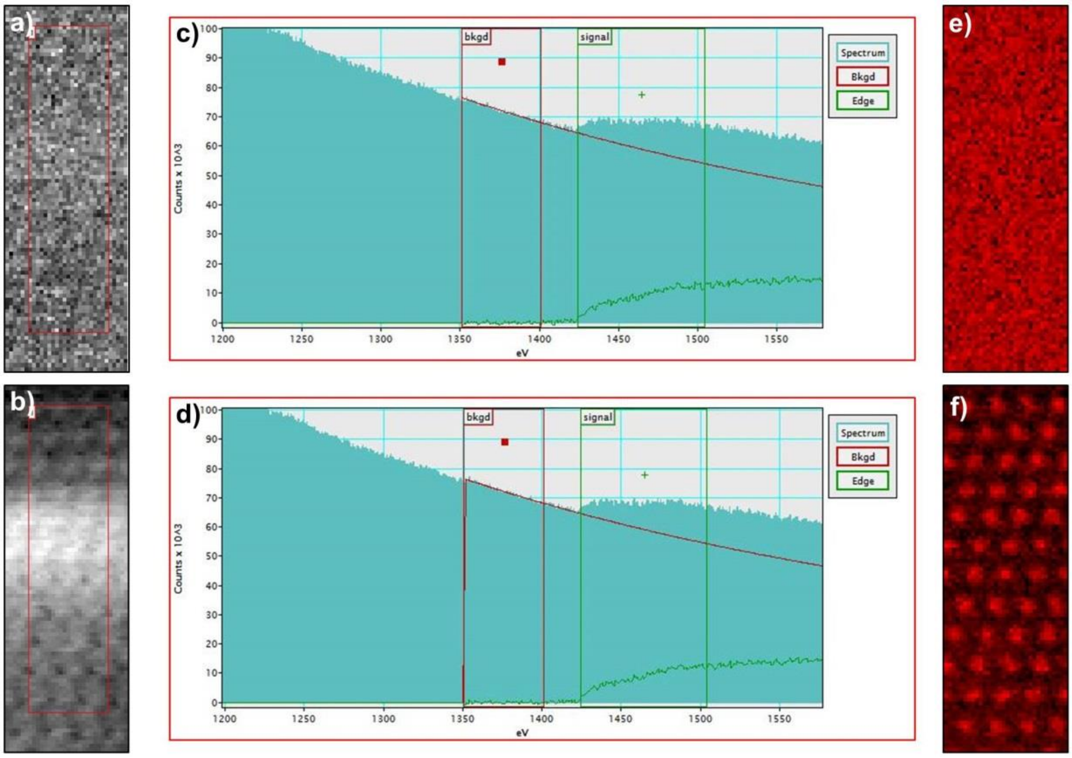

Figure 3.9 (a) non-PCA SI; (b) reconstructed SI; (c-d) extracted spectra from the regions indicated by red rectangles on (a) and (b), respectively; (e-f) non-PCA and PCA elemental maps of Se.

3.4.2. Energy-dispersive X-ray spectroscopy

An ionized atom, with an empty state within its inner-shell, can return to a lower energy state simply by filling the empty state with an electron from the outer shells. This process is known as de-excitation.[60] Due to the energy difference between the electron shells, excess energy is released as an Auger electron or an X-ray during de-excitation. Possible electron transitions between different shells of each atom are defined, and the energy of the emitted X-rays is characteristic for each transition. Hence, EDXS, like EELS, can be used to derive information about the composition of the sample. An example of an EDX spectrum from the Ga-rich region of a CIGS absorber is shown in Figure 3.10. Similarly to EELS, EDXS peaks are named depending on the energy shells, to and from which the transition occurs. For instance, if a K shell hole is filled by an L shell electron, then the X-ray 'line' is called K_α, whereas if the same hole is filled by an M shell electron, it is called K_β.

EDXS gives rapid qualitative results, but one needs to be careful with quantification. Before the quantification, the background, which mainly originates from bremsstrahlung, needs to be removed. For thin TEM samples, quantification can be done by comparing the elemental peak intensities with standards: this is known as the *k*-factor method.[60] The so-called *k*-factors are compound, microscope/detector and acceleration voltage dependent. They can be determined on a given instrumental set-up using standard compounds with pre-determined compositions; however for the CIGS system, there is no standard sample that can be used, as CIGS is a multi-component, complex and non-stoichiometric compound with possible impurity elements.

During the acquisition of EDXS elemental maps and line scans, the intensity of each pre-selected element is determined and plotted as a function of the X and Y beam position.

For high spatial resolution EDX and EELS analyses, a small probe is needed. Beam broadening through the sample thickness limits the spatial resolution, especially for EDXS as a significant amount of X-rays is emitted from the beam broadening region.[76] Another limiting factor in EDXS is its low count rates due to the restrictions in positioning and detection area of the detector.

The ultimate energy resolution achievable with EELS (< 20 meV) is much better than EDXS (~100 eV), especially when using a monochromator. EELS can be used for electronic structure analysis in addition to the chemical analysis that can be done via both methods.

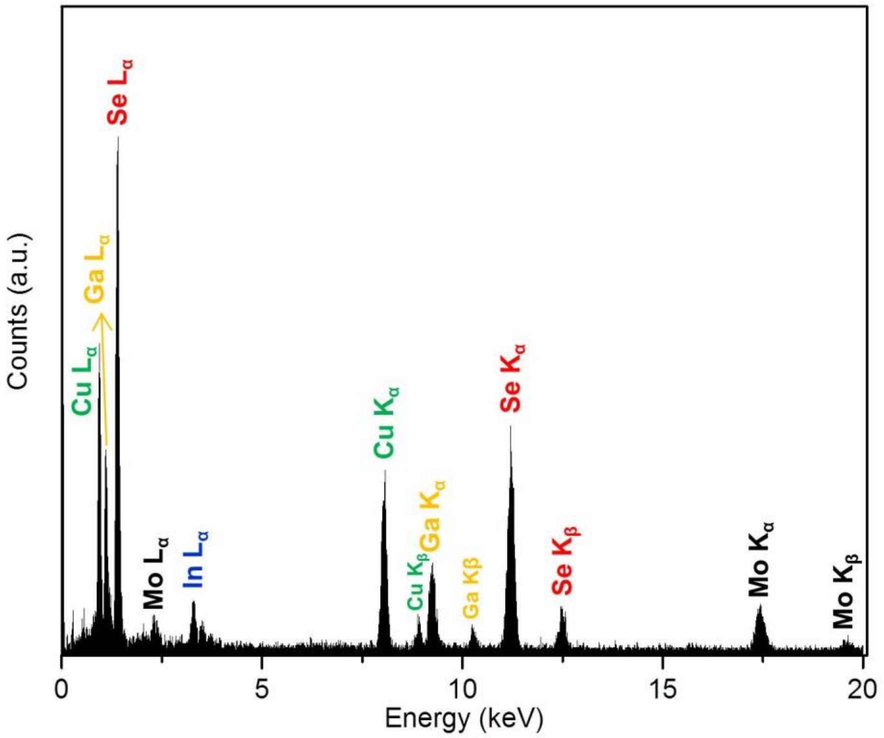

Figure 3.10 An example of a background removed EDX spectrum from a CIGS sample from a Ga-rich region.

3.5. Sample preparation

Cross-sectional thin lamellae from the CI(G)S absorbers were prepared[†] in a focused ion beam (FIB) Zeiss Crossbeam XB 1540 EsB instrument, using the *in-situ* lift-out method.[77, 78] In this method, a Pt metal thin film is deposited on the area of interest [Figure 3.11 (a) and (b)] to protect the sample surface from ion beam damage. Two parallel stair-step FIB trenches are milled out on both sides of the protection layer [Figure 3.11 (c)] using a Ga^+ focused ion beam. An accelerating voltage of 30 kV and a beam current of 10 nA is used in this step. After cutting most of the obtained slice free [Figure 3.11 (d)], a micromanipulator tip is welded to one of the free corners of the lamella, before the side cut is finished [Figure 3.11 (e)]. The lamella is then lifted out of the bulk sample and welded to a special support grid –a FIB grid– [Figure 3.11 (f)]. The process is finalized with a final milling (30 kV, 200 pA and 50 pA) and polishing (3 kV, 50 pA) steps [Figure 3.11 (g)–(i)]. Because of the stringent thickness requirements for analytical measurements, separate areas (referred to as windows) at various depth of the absorber layer were thinned as shown in Figure 3.11 (i). This allowed probing structural defects at changing [In]/[Ga] ratio through the whole absorber layer. Figure

---

[†] The FIB lamellae were prepared by Dr. Bernhard Fenk.

3.12 shows an example of a ready FIB lamella. In this study, before FIB slicing, some of the absorbers were coated with a C layer to protect the sample surface further.

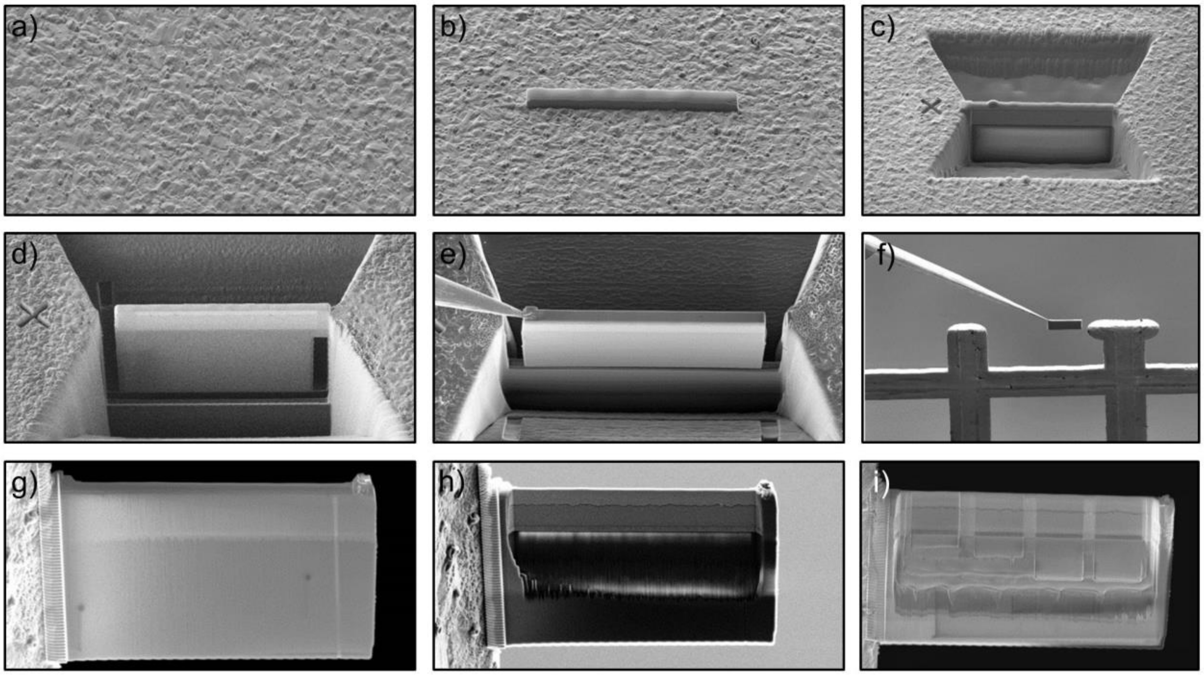

Figure 3.11 FIB sample preparation stages: (a) area of interest; (b) Pt deposition on the selected area; (c) cutting of FIB trenches, (d) cutting sides of the slice; (e) welding of the micromanipulator to the slice; (f) lift-out of the lamella and welding it to the grid; (g) welded lamella; (h) first side milling; (i) windows milling and polishing from the second side.

FIB is a fast method, however the high voltage and intense current of the ion beam can cause several problems, such as surface roughness, deep ion implantation, amorphization and temperature rise, which can cause structural changes within the sample.[79] For CI(G)S samples, the final polishing step is thus especially important, to avoid the formation of undesirable Cu agglomerates (seen in Figure 3.12 with yellow arrows and oval) on the surface of the lamellae during the milling process. Preferential sputtering under the Ga beam is given as a possible formation mechanism of these Cu agglomerates.[80] Although it is not possible to fully eliminate the formation of Cu agglomerates on the TEM lamellae, using a XeF_2 reactive gas atmosphere during the sputtering process, liquid-N_2 cooling the sample and reducing the Ga ion beam energy are suggested ways to reduce the number of Cu droplets formed during sample preparation.[80]

In addition to the FIB sample preparation, before the HR-STEM analyses, which were done using a Nion UltraSTEM 100, a turbo-pumped vacuum oven was used for *ex-situ* baking of the TEM lamellae mounted on their sample holder at 130 °C under $1.33\text{x}10^{-4}$ Pa for 5 h to minimize carbon-based contamination.

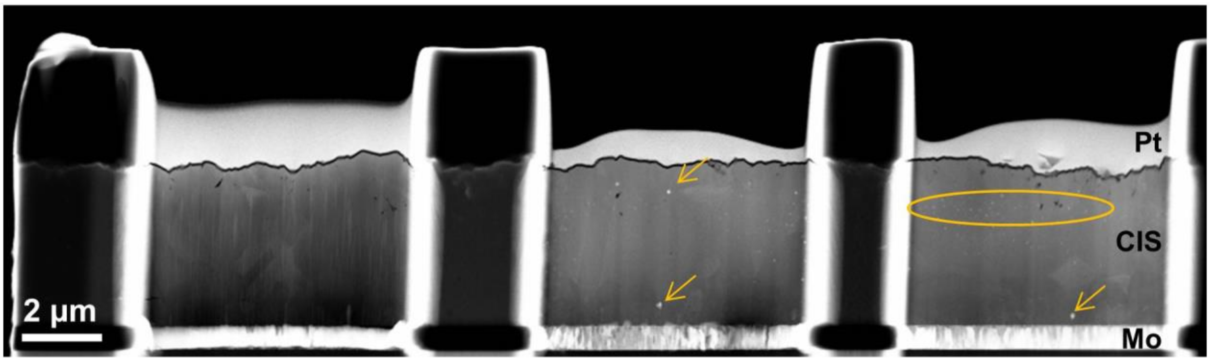

Figure 3.12 A ready TEM lamella with three windows. The yellow oval and arrows show Cu agglomerates.

3.6. Instrumentation

The experimental results presented in this work were acquired using four S/TEMs shown in Figure 3.13.

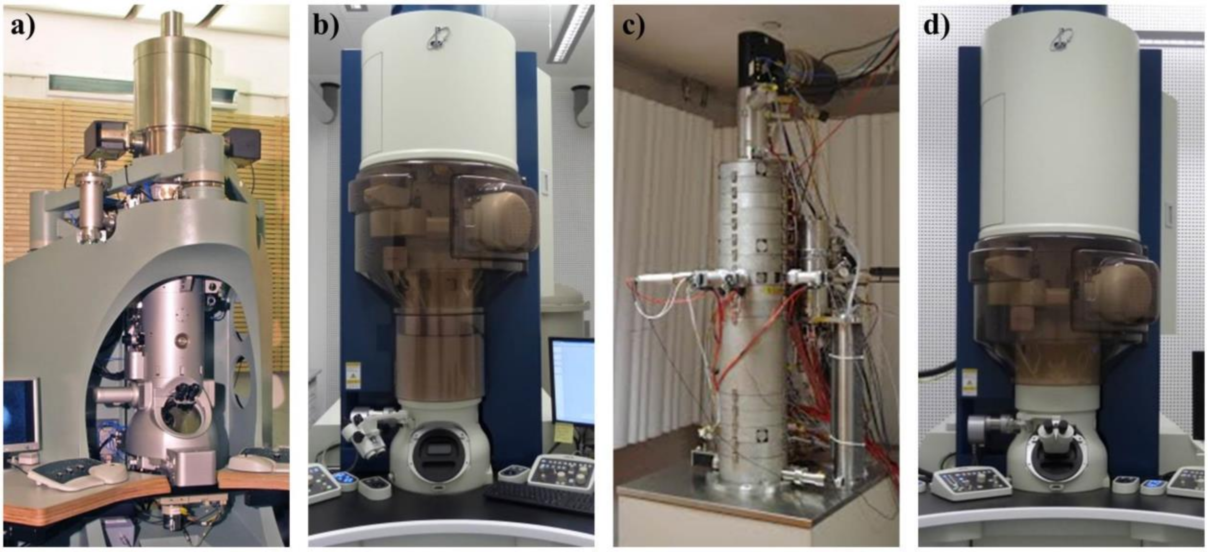

Figure 3.13 Microscopes used for this study (a) Zeiss SESAM, (b) JEOL ARM-200F CETCOR, (c) Nion UltraSTEM 100, (d) JEOL ARM-200F DCOR

The Zeiss Sub-Electron-Volt Sub-Angstrom Microscope (SESAM) microscope, equipped with a Schottky field emission gun (FEG) and operating at 200 kV acceleration voltage, was used for STEM-LAADF imaging and heating experiments. The ADF detector angular range was set from 11 to 72 mrad for LAADF imaging, by selecting an appropriately large microscope camera length to detect electrons that scatter to lower angles. A Gatan double tilt heating holder (Model 652) was used to heat the sample up to 470 °C.

EDXS measurements in STEM mode were carried out on sample cross sections at 200 kV acceleration voltage using an image-corrected (CETCOR) JEOL ARM 200F microscope, equipped with a cold-field emission gun (CFEG) and a Bruker QUANTAX X-ray spectrometer for EDXS elemental mapping and line-scan analysis.

HR-STEM and EELS measurements were carried out in parts at 100 kV on a Nion UltraSTEM 100 microscope equipped with a CFEG, a Cs probe corrector and a Gatan Enfina EEL spectrometer. HR-STEM imaging was performed by using simultaneous HAADF and medium-angle annular dark-field (MAADF)/bright field (BF) detectors. The HAADF and MAADF detectors' angular range were set to 85-185 mrad and 42-85 mrad, respectively. The beam convergence semi-angle was 33 mrad for imaging and the collection semi-angle was 38 mrad for the EELS investigations. The EELS measurements were conducted at 1 eV/channel dispersion covering the energy loss from 315 eV to 1655 eV to allow simultaneous elemental mapping of In, Cu, Ga and Se.

Additional HR-STEM and EELS measurements were carried out at 200 kV on a probe-corrected (DCOR) JEOL ARM 200F microscope equipped with a CFEG and a Gatan GIF Quantum ERS spectrometer. The HAADF detector's angular range was set to 109-270 for imaging. The beam convergence semi-angle was 28 mrad for imaging, and the collection semi-angle was 111 mrad for EELS investigations. The EEL SIs were acquired in DualEELS mode at 1eV/channel dispersion covering the core energy-loss from 300 eV to 2348 eV.

3.7. Strain mapping

Geometric Phase Analysis (GPA) is an advanced imaging analysis technique used to map the deformation and strain of HRTEM and HR-STEM images.[81] It can be carried out using the GPA plug-in for the image processing package of Gatan DigitalMicrograph (DM), which is a commercial implementation of the technique developed by HREM Research Inc. Additionally, during STEM imaging scan distortions or sample/stage drift might affect local strain measurements. The scan noise can be partially removed before the strain analysis is carried out using a variety of methods, for instance implementing another DM plug-in, Jitterbug[82]. In the present study; however, Jitterbug was not used as it did not change the main features, which needed to be highlighted.

Figure 3.14 shows the results of the GPA on a Frank partial dislocation discussed in section 4.3.2. An HAADF image of the Frank partial dislocation is presented in Figure 3.14 (a). Figure 3.14 (b) shows the Fourier transform of the HAADF image. The <112> reflections, as shown by red arrows, are selected for the GPA. A circular mask is used to isolate two reflections and to obtain inverse Fourier transforms [Figure 3.14 (c)–(d)]. The size of the mask determines the spatial resolution and precision: a larger mask increases the spatial resolution at the expense of precision. Here a mask with a size corresponding to 1.31 nm spatial resolution is used. Two ‘phase images’ corresponding to the lattice fringe images are then extracted. After defining a reference area, by selecting a region of the undistorted lattice, the phase image is refined [Figure 3.14 (e)–(f)]. The refined phase images are then used to calculate the two main components, ε_{xx} and ε_{yy}, of the strain tensor [Figure 3.14 (g)–(h)].

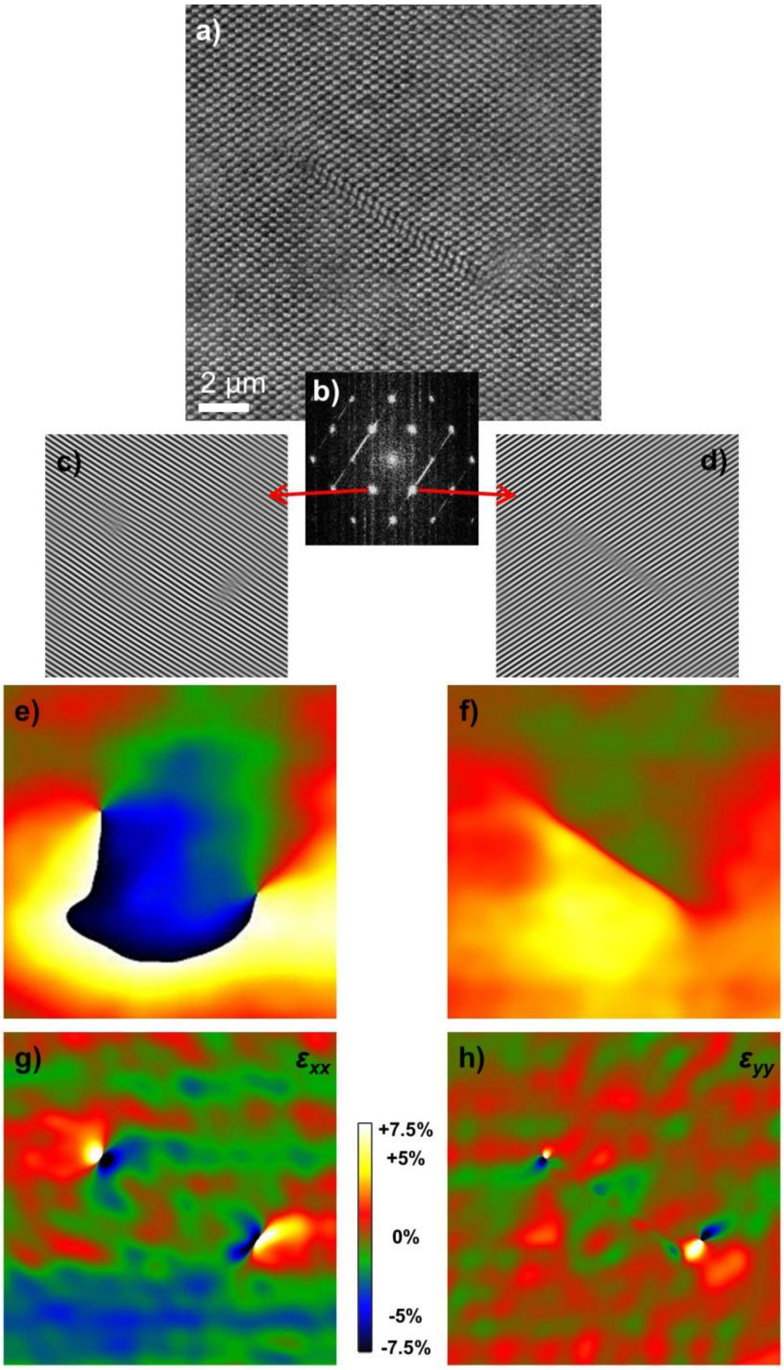

Figure 3.14 Geometric phase analysis. (a) HAADF image of a Frank partial dislocation; (b) Fourier transform of the HAADF image, red arrows show selected {112} reflections; (c-d) {112} lattice fringes; (e-f) Phase image of {112} lattice fringes; (g-h) ε_{xx} and ε_{yy} components of the strain tensor.

4. Experimental results and discussion

This chapter is mainly composed of three parts. In the first part, the second stage of the three-stage co-evaporation technique is mimicked by preparing diffusion couples and heating them in the STEM. The results provide direct visual insight into the recrystallization of the CIGS.

In the second part, the effect of recrystallization is analyzed via the interruption of the growth process. The defect concentration and the elemental distribution along the absorbers, from an intermediate and a final growth stage, are compared by LAADF imaging and EDXS.

After the recrystallization, and even after the completion of the growth process, structural defects are detected in the absorbers by LAADF imaging. Therefore, in the final part of this chapter, the structure and composition of individual microstructural defects from various stages of the growth are analyzed thoroughly by HR-STEM in combination with EELS.

Parts of this chapter were published in the following journal articles;

- Elemental redistributions at structural defects in Cu(In,Ga)Se_2 thin films for solar cells; **E. Simsek Sanli**, Q. M. Ramasse, W. Sigle, D. Abou-Ras, R. Mainz, A. Weber, H.-J. Kleebe, and P. A. van Aken; Journal of Applied Physics **120**, 205301 (2016); DOI: 10.1063/1.4967731.[83]

- Point defect segregation and its role in the detrimental nature of Frank partials in Cu(In,Ga)Se2 thin-film absorbers; **E. Simsek Sanli**, D. Barragan-Yani, Q. M. Ramasse, K. Albe, R. Mainz, D. Abou-Ras, A. Weber, H.-J. Kleebe, and P. A. van Aken; Physical Review B 95,195209 (2017); DOI: 10.1103/PhysRevB.95.195209.[84]

- Evidence for $Cu_{2-x}Se$ platelets at grain boundaries and within grains in Cu(In,Ga)Se_2 thin films; **E. Simsek Sanli**, Q. M. Ramasse, R. Mainz, A. Weber, D. Abou-Ras, W. Sigle and P. A. van Aken; Applied Physics Letters **111**, 032103 (2017); DOI: 10.1063/1.4993917.[85]

4.1. Investigation of the recrystallization by comparative *in-situ* heating study

Studying the recrystallization is essential for understanding the evolution of the many linear and planar defects often observed in CIGS absorbers, as they can be assumed to affect the performance of the CIGS solar cells. In early studies, the recrystallization of CI(G)S was investigated by preparing samples with various growth paths or by interrupting the growth at several points in time.[31, 32, 86-88] In one of the earliest growth-interruption studies, the phase change and grain growth were observed during the Cu-poor/Cu-rich transition, where the recrystallization occurs.[87] In the first stage, $(In,Ga)_2Se_3$ was formed; at the second stage, with increasing amount of Cu, a phase transformation from $Cu(In,Ga)_5Se_8$ to $Cu(In,Ga)_3Se_5$ and finally to stoichiometric $Cu(In,Ga)Se_2$ was detected. The grain growth mechanism was associated with the movement of crystallite interfaces that were induced by atomic diffusion.[87] This mechanism is similar to the well-known solid-phase sintering growth model. Later, Barreau *et al.* explained the reason for the atomic diffusion in their proposed growth mechanism by grain boundary migration (GBM).[86] In the GBM model, the atomic diffusion is based on the reduction in the number of the high-energy, highly defected grains through the growth of lower energy, defect free grains.[86] Caballero *et al.* noticed grain growth also at Cu-poor compositions ([Cu]/([In]+[Ga]) = 0.70-0.95) of absorbers, which have not reached the stoichiometry point during the growth process.[32] However, those Cu-poor absorbers resulted in poor conversion efficiencies of the corresponding solar-cell devices.[32]

Finally, Rodriguez-Alvarez *et al.* designed *in-situ* energy-dispersive X-ray diffraction (EDXRD) experiments, where they analyzed the recrystallization and the film growth separately in order to reveal the sole effect of recrystallization on structural defects.[31] They prepared a Cu-poor CIGS with a Cu-Se capping layer, heated this diffusion couple and detected the evolution of XRD peaks *in-situ*. The signature of planar defects (PDs) in the observed XRD patterns disappeared after Cu diffusion from the capping layer into the Cu-poor CIGS.[31] They concluded that the recrystallization includes not only phase change and grain growth, but also defect annihilation that occurs only after enough Cu is incorporated into the Cu-poor CIGS layer.

STEM has been commonly used for imaging and spectroscopy of materials, but recently there have been significant advancements regarding the *in-situ* capabilities of this technique. Therefore, it was possible to revisit the work of Rodriguez-Alvarez *et al.* by preparing FIB lamellae from similar diffusion couples and probing the recrystallization via STEM *in-situ* heating. In contrast to XRD, STEM imaging gives direct imaging insights into the recrystallization.

To avoid the possible influence of In/Ga diffusion, a Cu-poor CIS (without Ga) precursor layer was grown by interrupting the growth during the second stage (before reaching the stoichiometry point). A Cu-Se capping layer was then deposited at 150 °C on the Cu-poor CIS precursor layer. The deposition of the capping layer at low temperatures is crucial to impede diffusion between the Cu-Se and CIS. The samples were then heated in the microscope from 30 to 450 °C either at a heating rate of 10 K/min and 5 min holding plateaus in steps of 30 °C, or with a continuous temperature ramping of 3 K/min (no holding of temperatures). The schematic representation of the experiment is given in Figure 4.1.

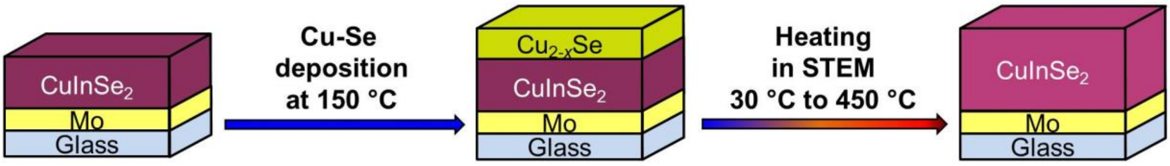

Figure 4.1 Schematic drawing of the experiment: a Cu-poor CIS precursor layer on a Mo-coated soda-lime glass (SLG), deposition of the $Cu_{2-x}Se$ capping layer at 150 °C, STEM *in-situ* heating up to 450 °C and formation of Cu-rich CIS.

The samples[‡], which were extensively analyzed in this study, are shown in Table 4-1. In section 4.1 the first sample set will be discussed; the second sample will be analyzed in section 4.2 and 4.3.

Two FIB lamellae were prepared from sample 1.1 and imaged whilst applying the two different heating procedures described above. Two images from each lamella are shown in Figure 4.2 and Figure 4.3, respectively. During heating, the GB migration and grain growth were probed by simultaneous STEM-LAADF imaging. In both lamellae, the GB migration started at around 200 °C and accelerated around 400 °C. The yellow-dotted ovals on both figures highlight typical changes in grain morphology: defect-free grains grow at the expense of grains with closely-spaced PDs. This is in good agreement with the grain growth mechanism proposed by Barreau *et al.*[86] However, remaining PDs are still visible: some of them are shown by red arrows in both figures. Possible reasons for the remaining PDs are the lack of Cu or the vacuum atmosphere in the TEM instead of continued material supply in the co-evaporation chamber.

[‡] First sample set was grown by Dr. Helena Stange, Dr. Dieter Greiner and Dr. Mark Daniel Heinemann. Second sample set was grown by Dr. Roland Mainz and Dr. Alfons Weber.

Table 4-1 Sample sets with growth parameters

Sample #		**Material system**	**Growth temp. (at the 2nd stage) (°C)**	**Process**	**[Cu]/([In]+[Ga])[§]**
1[**]	**1.1**	CIS/Cu-Se	450	Interrupted + thin capping	0.97
	1.2	CIS	450	Interrupted	0.9
	1.3	CIS/Cu-Se	450	Interrupted + thick capping	1.07
2		CIGS	430	Interrupted	0.71
		CIGS	430	Finished	0.81

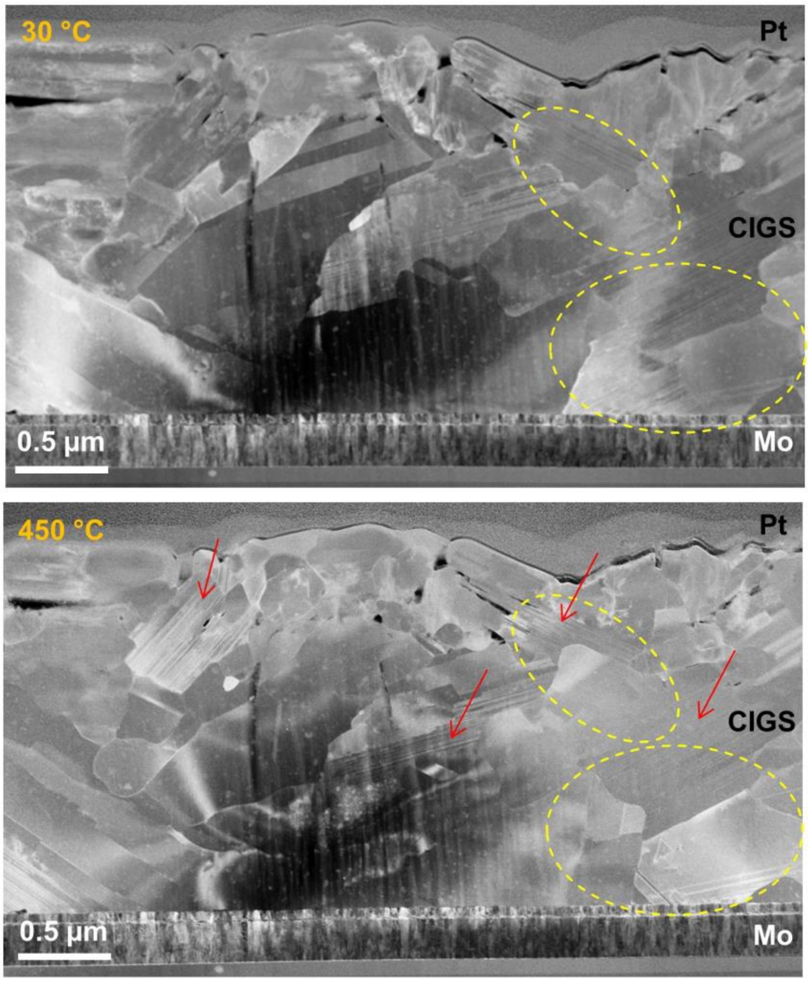

Figure 4.2 LAADF images of the sample 1.1 at 30 °C and 450 °C. Interrupted heating with 5 min. breaks was applied for the first FIB lamella. The grain growth towards the planar defected grains can be seen in the yellow dotted ovals. Red arrows show the remaining grains with closely-spaced PDs.

[§] [Cu]/([In]+[Ga]) ratio was calculated via X-ray fluorescence (XRF) by the growth team.

[**] The growth temperature at thestage shows the temperature before the process interruption. Final Cu-Se deposition was done at 150 °C.

Another possible reason might be the differences between the temperature profiles of the STEM heating experiments and the usual growth process. During heating in the STEM, the temperature is increased from room temperature gradually and reaches 450 °C, whereas during the growth in the co-evaporation chamber, the temperature is increased from about 300 °C to 450 °C and stays at this temperature during the rest of the growth process. In the STEM, when the lamellae are kept at elevated temperatures material loss, *i.e.* void formation, was detected and the process had to be stopped.

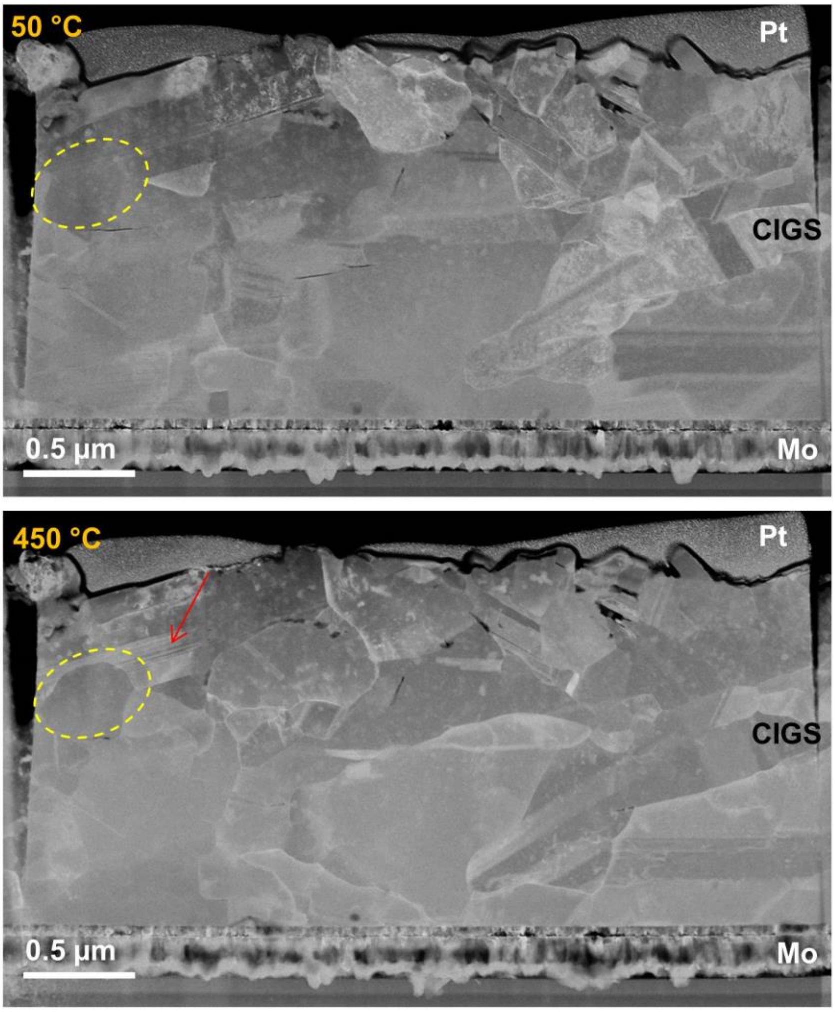

Figure 4.3 LAADF images of the sample 1.1 at 50 °C and 450 °C. Continues temperature ramping was applied for the second FIB lamella. Again yellow ovals show the grain growth towards the planar defected grains, although there were not many grains with closely-spaced PDs in this region. Red arrow shows the remaining closely-spaced PDs.

The elemental compositions of the absorbers are shown by STEM-EDXS maps (Figure 4.4) and line scans (Figure 4.5). EDXS analyses were carried out before and after the heating experiments. EDXS maps that were acquired before the heating showed the presence of Cu-rich grains on top a chemically homogeneous region. After heating, a homogeneous elemental distribution was detected throughout the absorber. EDXS line scans, acquired along the red arrows indicated in Figure 4.4, revealed the presence of a pure $Cu_{2-x}Se$ phase on top of the CIS phase before the heating while only the CIS phase was detected after the heating. These analyses confirmed that during heating the excess Cu in the $Cu_{2-x}Se$ grains diffuses into the Cu-poor CIS, while simultaneously the In in the CIS phase diffuses into $Cu_{2-x}Se$ grains. It is known that the Se sublattice is preserved for both $Cu_{2-x}Se$ and CIS phases[89]; therefore, the homogeneous elemental distribution along the absorber layer is a result of Cu-In (cation) interdiffusion only.

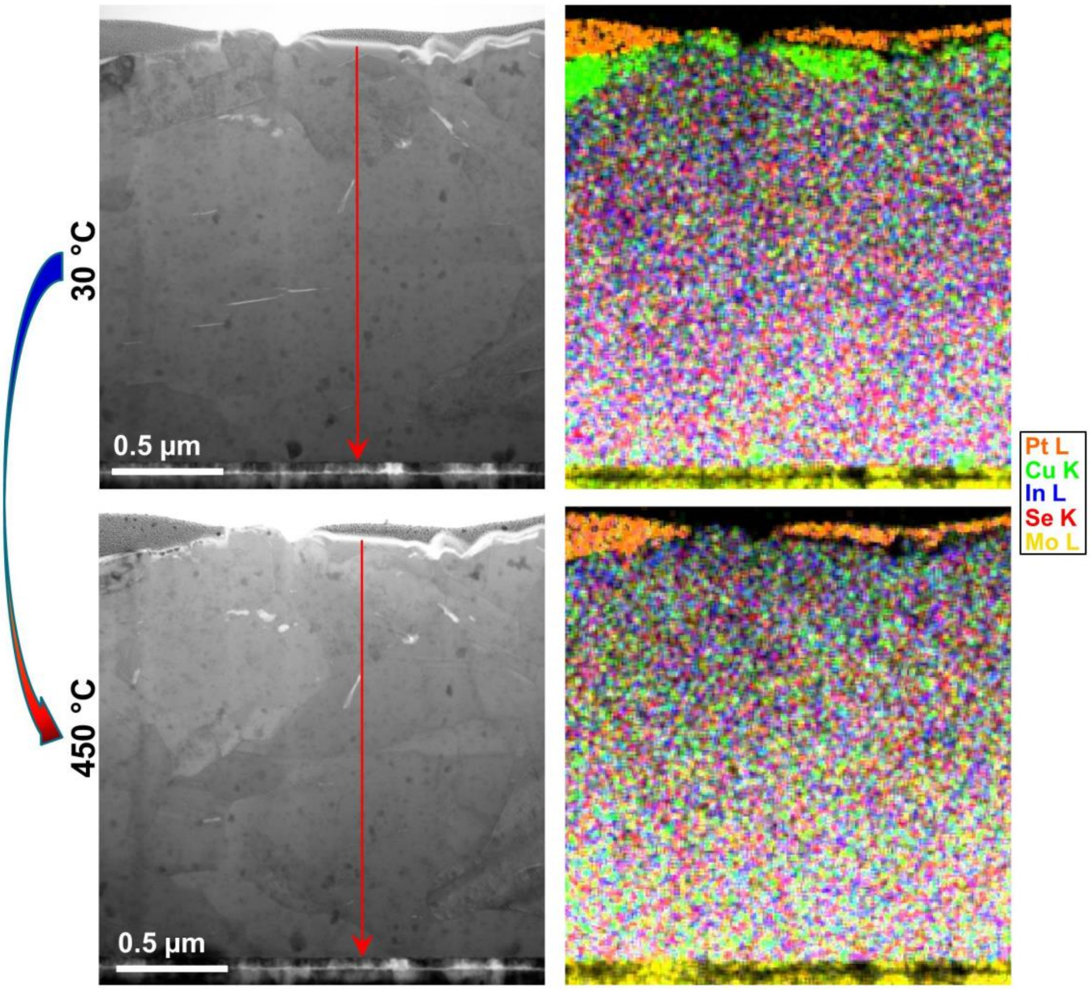

Figure 4.4 STEM-BF images from a part of the TEM lamella shown in Figure 4.3. STEM-EDXS maps show the compositional changes before and after the heating.

These analyses have proven the occurrence of a phase change and grain growth towards the grains with closely-spaced PD. However, two important questions arise: *i)* Would heating have any effect on recrystallization if there was no Cu? *ii)* Was the thickness of the $Cu_{2-x}Se$ capping layer enough for the absorber to reach the Cu-rich composition? Had the overall composition become Cu-rich, there should have been excess Cu in the absorber after the heating, which was not the case.

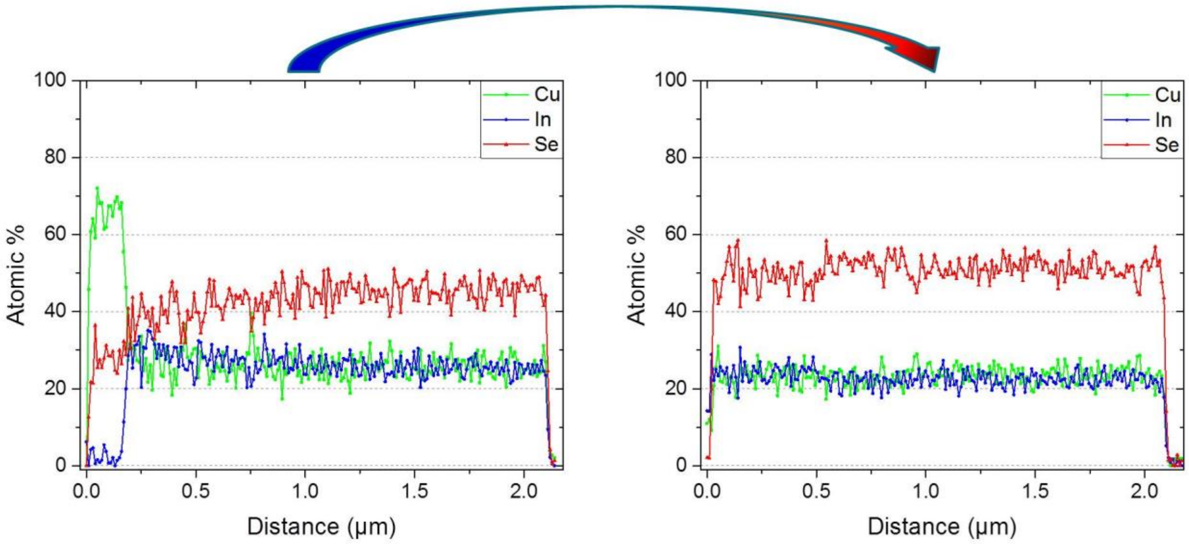

Figure 4.5 STEM-EDXS line scans extracted along the red arrow indicated in Figure 4.4. The composition profiles across the lamella before (left) and after (right) the heating are shown.

In order to answer the first question, a FIB lamella from the sample 1.2, the Cu-poor CIS precursor layer without Cu-Se capping, was prepared. Figure 4.6 shows two LAADF images acquired at 30 °C and 450 °C. A continuous temperature ramp was applied, but neither defect annihilation nor grain growth was detected in this sample. The difference in the contrast of the two images is only due to the heating related instabilities, such as a slight bending of the lamella. The contrast change is tracked during the *in-situ* heating clearly. If there was Cu excess in the present lamella, one would definitely detect shrinkage in the grain with closely-spaced PDs (shown with red arrows in the same figure).

A homogenous elemental distribution was preserved during the *in-situ* heating of the lamella (Figure 4.7). The EDXS line-scans (not shown here) also confirmed the homogeneous distribution across the lamella. The only truly striking observation was the disappearance of the Cu agglomerates at around 400 °C. This is most probably due to their diffusion into the Cu-poor CIS layer rather than to evaporation. As explained in sub-section 3.5, Cu agglomerates form at the surface of FIB lamellae during the milling process. Their number can be reduced by several techniques as discussed, but the formation of Cu agglomerates cannot be impeded completely.

Rodriguez-Alvarez *et al.* showed that the PD signal in the EDXRD pattern disappeared only in the case of CIGS with a Cu-Se capping layer.[31] The presented STEM results support that work: in the loss of Cu, no GB motion was detected. In a more recent study, the effect of temperature and Cu deposition rate on the PDs were tested.[33] The results showed that neither of them annihilates the PDs completely, unless the transition from a Cu-poor to a Cu-rich composition is completed. In another study, for a Cu-poor (22 at% Cu) CIS sample, 550 °C was suggested as the lowest temperature for significant grain growth according to the normal grain growth model.[28] However, in the present study maximum heating temperatures were set to 450-470 °C, to hinder fast material evaporation and any possible risk of breaking the samples in the microscope.

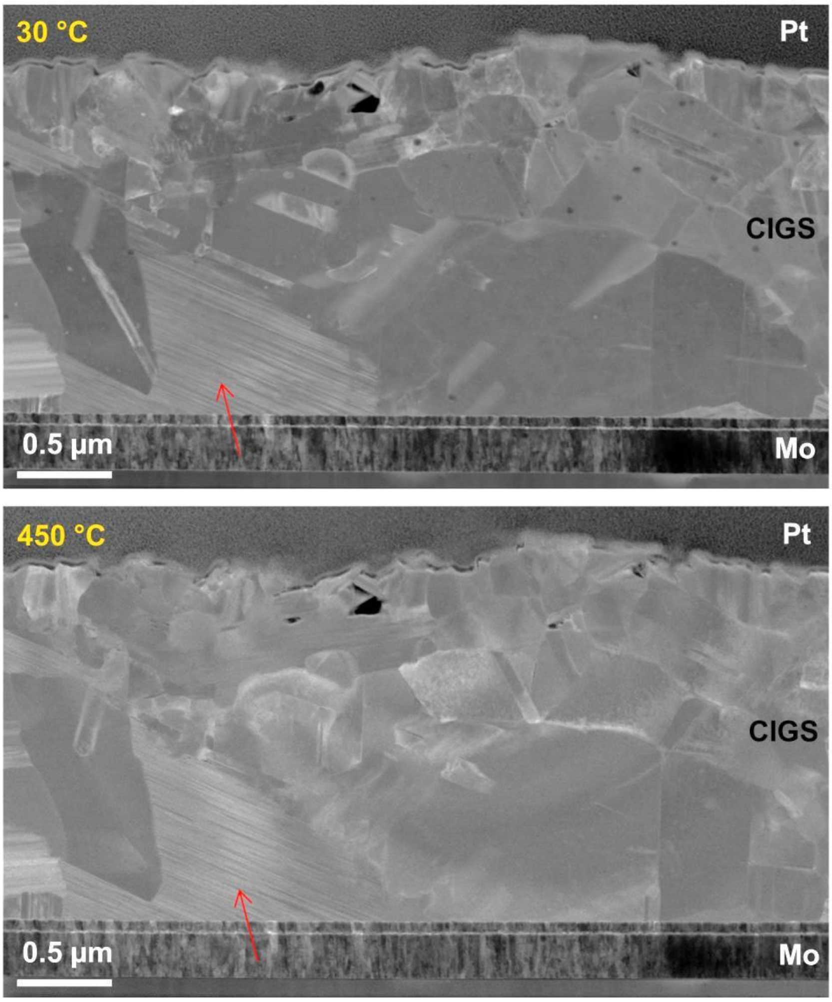

Figure 4.6 LAADF images of the sample 1.2 at 30 °C and 450 °C. Grain growth and defect annihilation were not detected. Red arrows show the grain with PDs.

In order to answer the second question, first the [Cu]/[In] ratio of the CIS/Cu-Se diffusion couple was determined via X-ray fluorescence (XRF). XRF is a fast, non-destructive technique used to determine the composition of materials. In this technique, the material is exposed to high energy X-rays (higher than the ionization energy of atoms in the material) and emits characteristic fluorescent X-rays. The technique thus provides elemental identification and composition quantification based on the peak energy and the intensity of the detected X-rays. XRF results showed that the [Cu]/[In] ratio is 0.9 for the Cu-poor CIS precursor, whereas with the Cu-Se layer it increases to 0.97. XRF is not straightforward for non-homogeneous samples; however, in this case, prior STEM results gave some hints that the [Cu]/[In] ratio might not exceed 1 and the XRF data are therefore in good agreement. To exceed a [Cu]/[In] ratio of 1, a thicker $Cu_{2-x}Se$ capping layer was deposited on the same CIS precursor layer and the [Cu]/[In] ratio was indeed determined as 1.07 via XRF for the final diffusion couple, sample1.3.

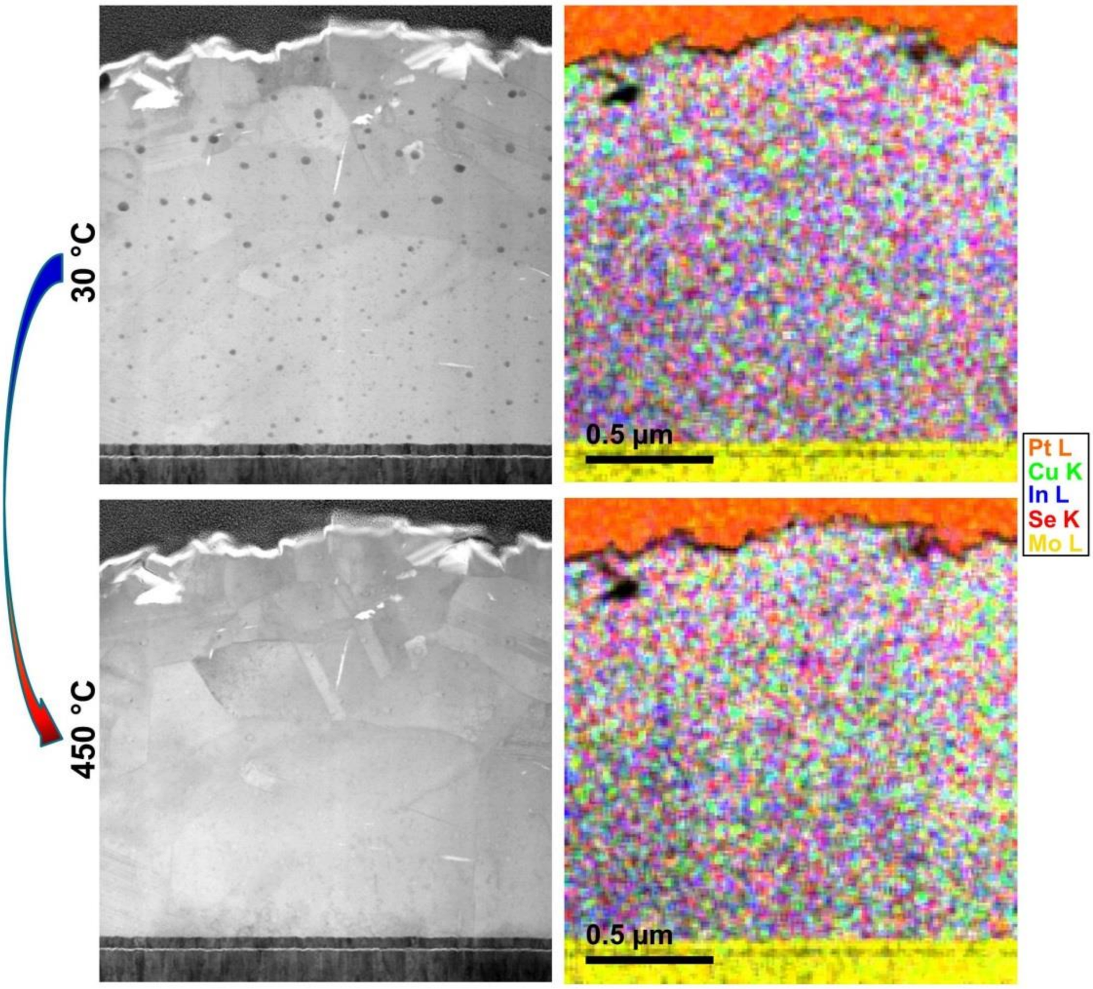

Figure 4.7 STEM-BF images and EDXS maps show the microstructural and compositional changes after the heating of sample 1.2. The only change observed is the in-diffusion of the Cu droplets into the lamella during the heating.

The initial (before heating) and final (after heating) microstructures of the sample 1.3 are seen in Figure 4.8. GB migration and annihilation of defects were tracked very clearly during the heating. The microstructure changed dramatically compared to sample 1.1. Two yellow ovals on Figure 4.8 indicate a pair of grains growing towards other grains with closely-spaced PDs. Additionally, most of the PDs are annihilated which gives a direct visual explanation for the loss of the PD signal at EDXRD measurements. However, it should also be noted that not all the closely-spaced PDs were annihilated as two sets of them are indicated by red arrows on the same figure. At low concentration, these PDs would not generate a strong XRD signal.

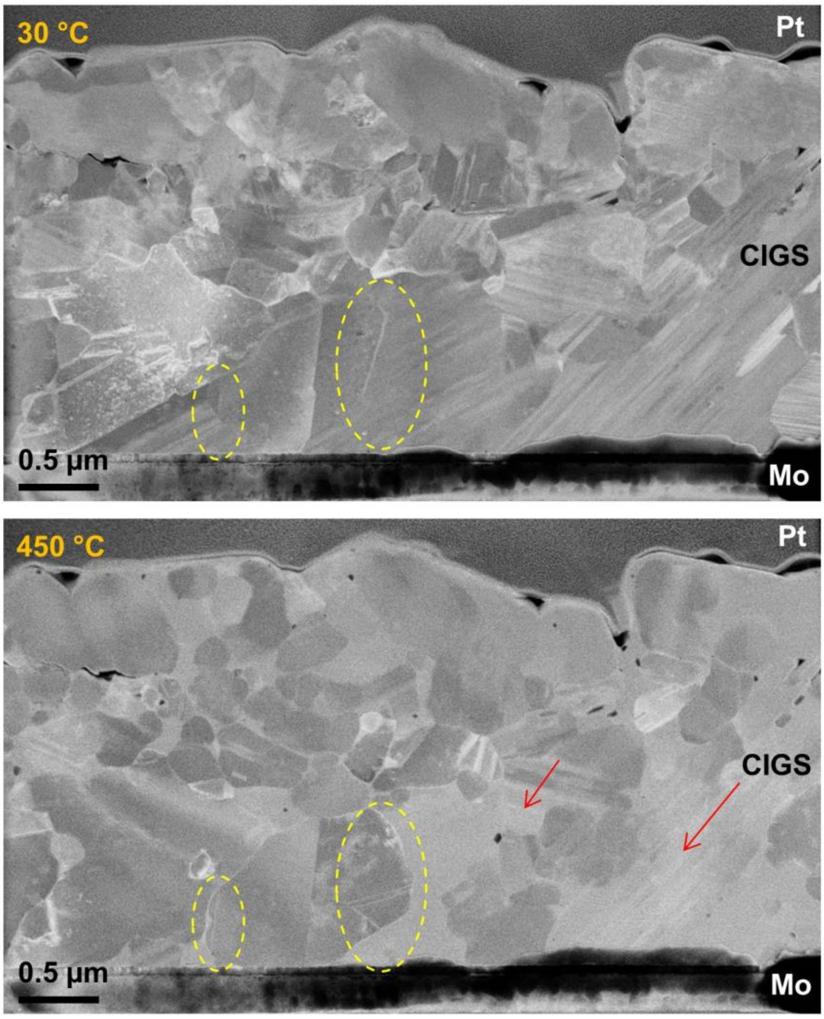

Figure 4.8 LAADF images of sample 1.3 at 30 °C and 450 °C. Red arrows show the remaining grains with PDs after heating. Yellow ovals show the grain growth towards the planar defected grains.

The elemental distribution was determined by EDXS maps (Figure 4.9) and line scans (Figure 4.10), which clearly show the CIS precursor with a thick $Cu_{2-x}Se$ capping layer before the heating, and the final spatial redistribution of two phases along the lamella after the heating. Due to overlap of the CIS and $Cu_{2-x}Se$ grains, the expected sharp phase transition between the grains is not apparent in the line scan acquired along the lamella after the heating. However, this sharp phase transition between the CIS and $Cu_{2-x}Se$ phases/grains is visible in Figure 4.11, which shows a top part of another region of the same lamella. There is no gradual diffusion zone for Cu and In in the vicinity of GBs. In one grain the Se sublattice is filled solely by Cu atoms, whereas in the next grain the same sublattice is filled by both Cu and In cations. A possible driving force for the spatial redistribution of the two phases might be related to entropy, as it has been suggested for $CuInS_2$. The entropy is much higher when two phases distribute in a volume than when they are separated laterally.[90]

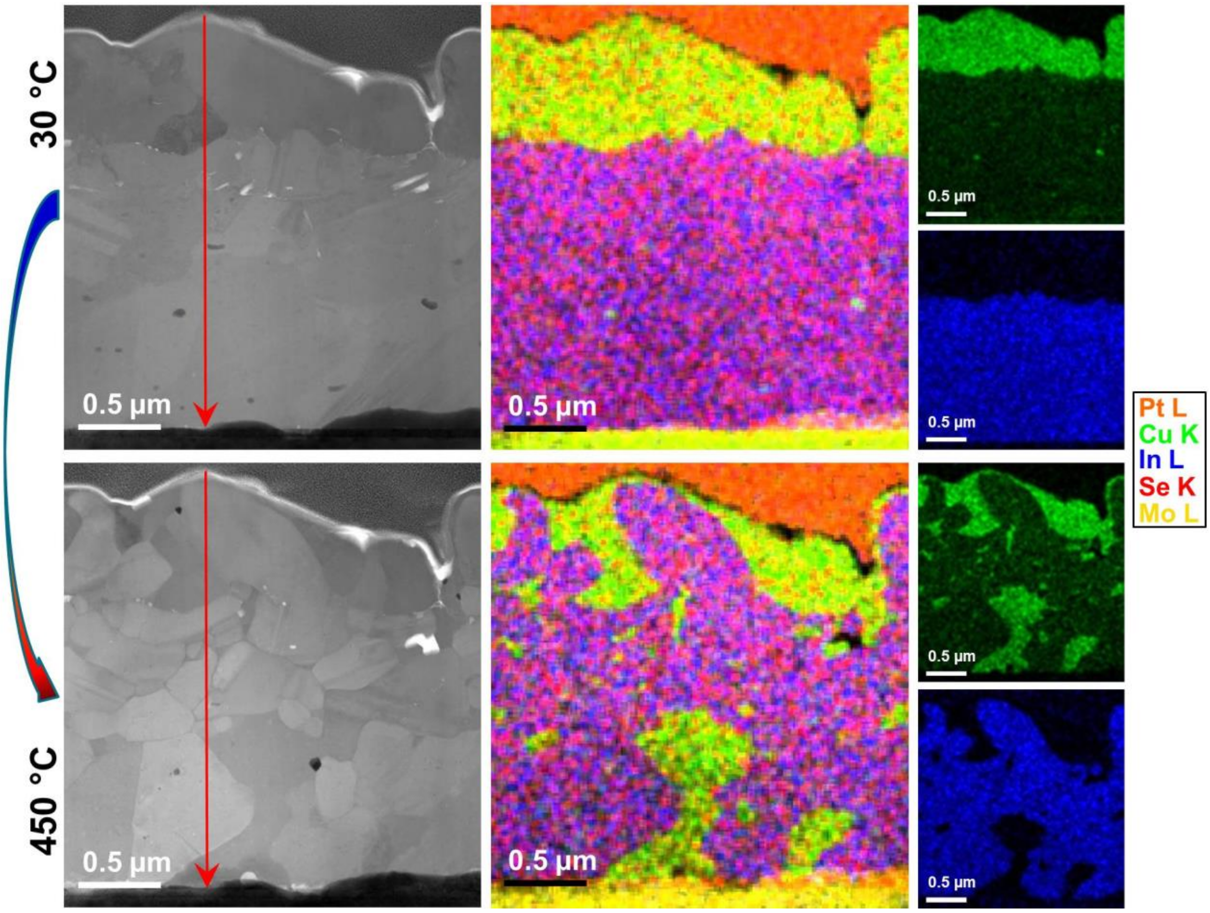

Figure 4.9 STEM-BF images and composite EDXS maps show the microstructural and compositional changes before and after the heating of the sample 1.3. The Cu-Se capping layer before the heating and new distribution of $Cu_{2-x}Se$ grains after the heating are shown. The Cu and Se are depicted in green and red color, respectively. Despite its yellowish appearance, the red-green $Cu_{2-x}Se$ phase should not be confused with Mo, which is shown by yellow color. On the right side of the figure Cu and In elemental distribution maps are shown separately for visual clarity.

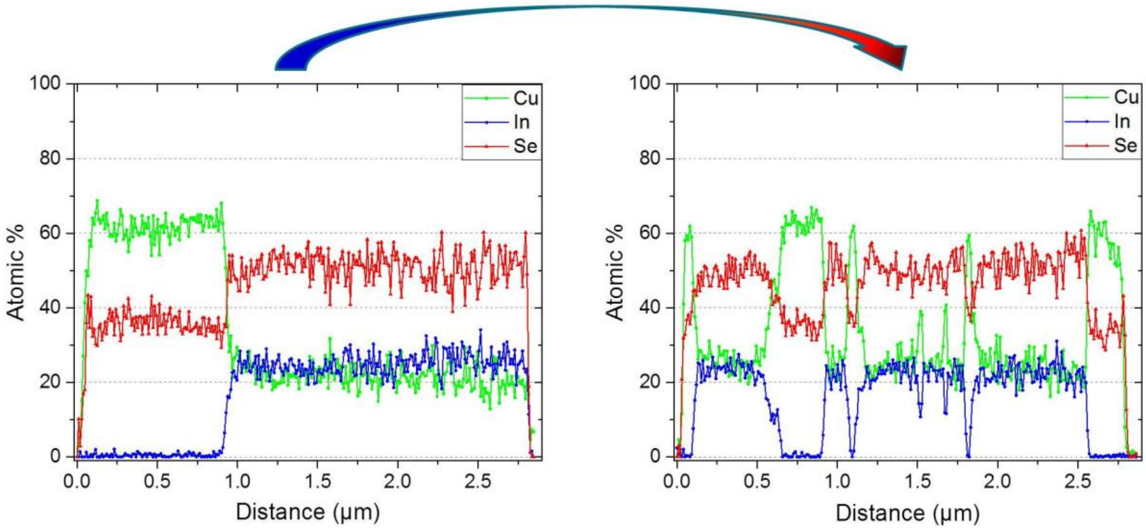

Figure 4.10 EDXS line scans extracted along the red arrows drawn in Figure 4.9 show the composition profile across the lamella before and after the heating, respectively.

The defect contrast is one of the strongest contributors to the LAADF signal, but some Z-contrast contribution remains. Therefore, the contrast change observed in the LAADF images acquired simultaneously give already some hints for the presence of interdiffusion of Cu and In during the heating. When Cu leaves from and In accumulates towards a $Cu_{2-x}Se$ grain, the grain becomes darker in the LAADF images. In contrast, when In leaves from and Cu accumulates towards a CIS grain, the contrast becomes brighter as it is shown in Figure 4.12 by 4 black-dotted ovals. However, in LAADF imaging one needs to be careful, since the highly defected grains also look brighter. For this analysis, the interdiffusion interpretation is supported by spectroscopy that was done after the heating.

In Figure 4.13, the yellow arrows in the time series show that the grain growth starts just below the interface between $Cu_{2-x}Se$ and CIS, and continues towards the Mo side as Cu diffuses in the CIS phase. It proves the effect of Cu on the grain growth.

Due to the interruption of the ordered lattice, GB planes contain a high vacancy concentration, which leads to faster cation diffusion at GBs than within grain interiors. In this study, EDXS results at higher magnification (Figure 4.14) provided further proof for the Cu diffusion along GBs. Especially for sample 1.3, the observation of Cu enrichment at many GBs indicates that Cu prefers to diffuse along the GBs. During heating, the contrast change in the $Cu_{2-x}Se$ phase starts at the interface region between $Cu_{2-x}Se$ and CIS. However, in some grains (as shown by the left and right black-dotted ovals in Figure 4.12) the contrast change started from the Pt side of the $Cu_{2-x}Se$ grains. This is an additional proof of Cu out-diffusion and In in-diffusion to the $Cu_{2-x}Se$ grains along the GBs.

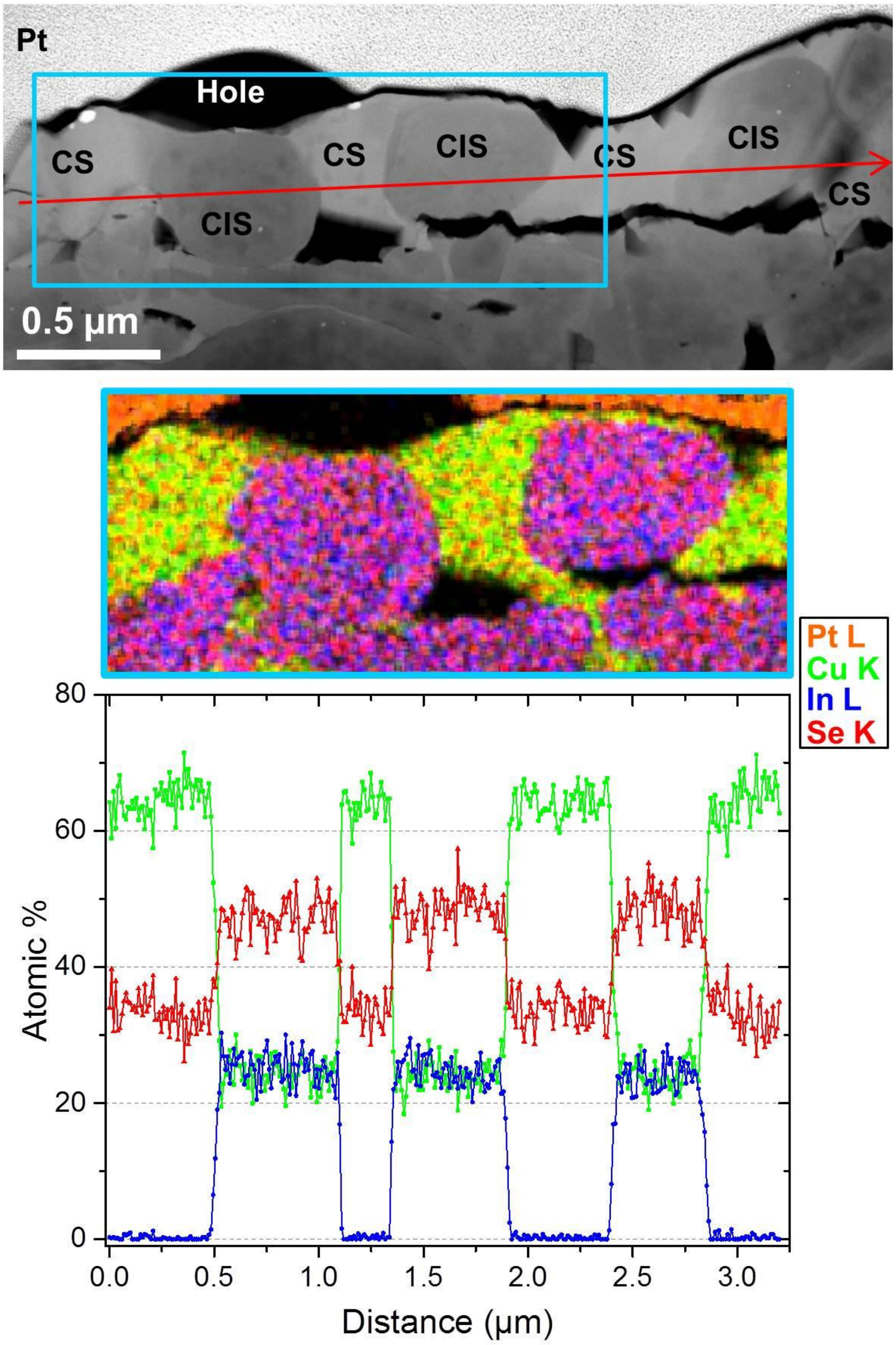

Figure 4.11 HAADF image from top part of the sample 1.3 after heating. Sharp phase transitions between the CIS and $Cu_{2-x}Se$ grains are shown by the EDXS map and the line scan, extracted from the regions shown by the blue rectangle and the red arrow on the HAADF image, respectively.

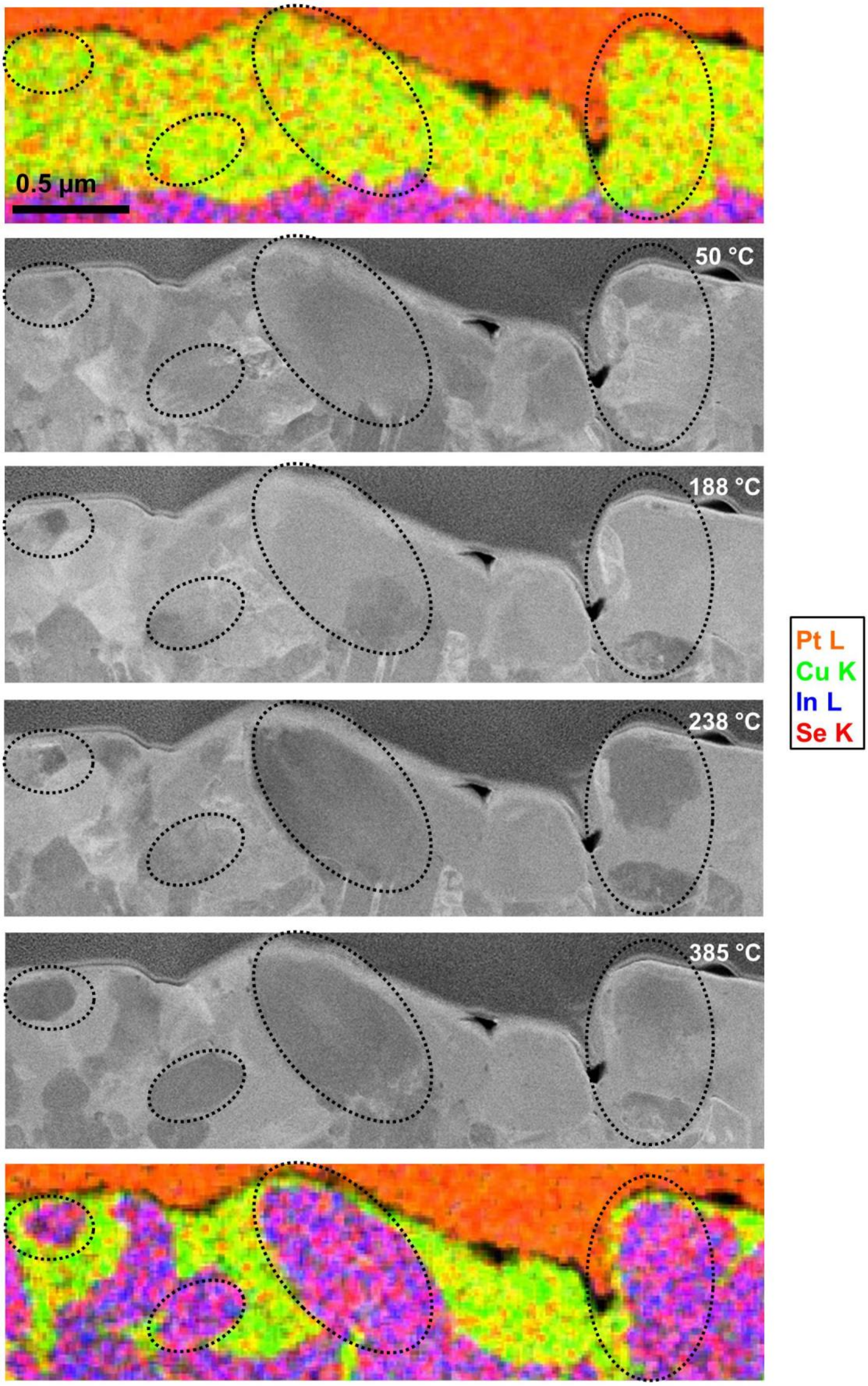

Figure 4.12 LAADF images acquired during *in-situ* heating at 50 °C, 188 °C, 238 °C and 385 °C. EDXS elemental maps show the elemental distribution before (above) and after (below) the *in-situ* heating. The scale bar in the upper image is identical for all images.

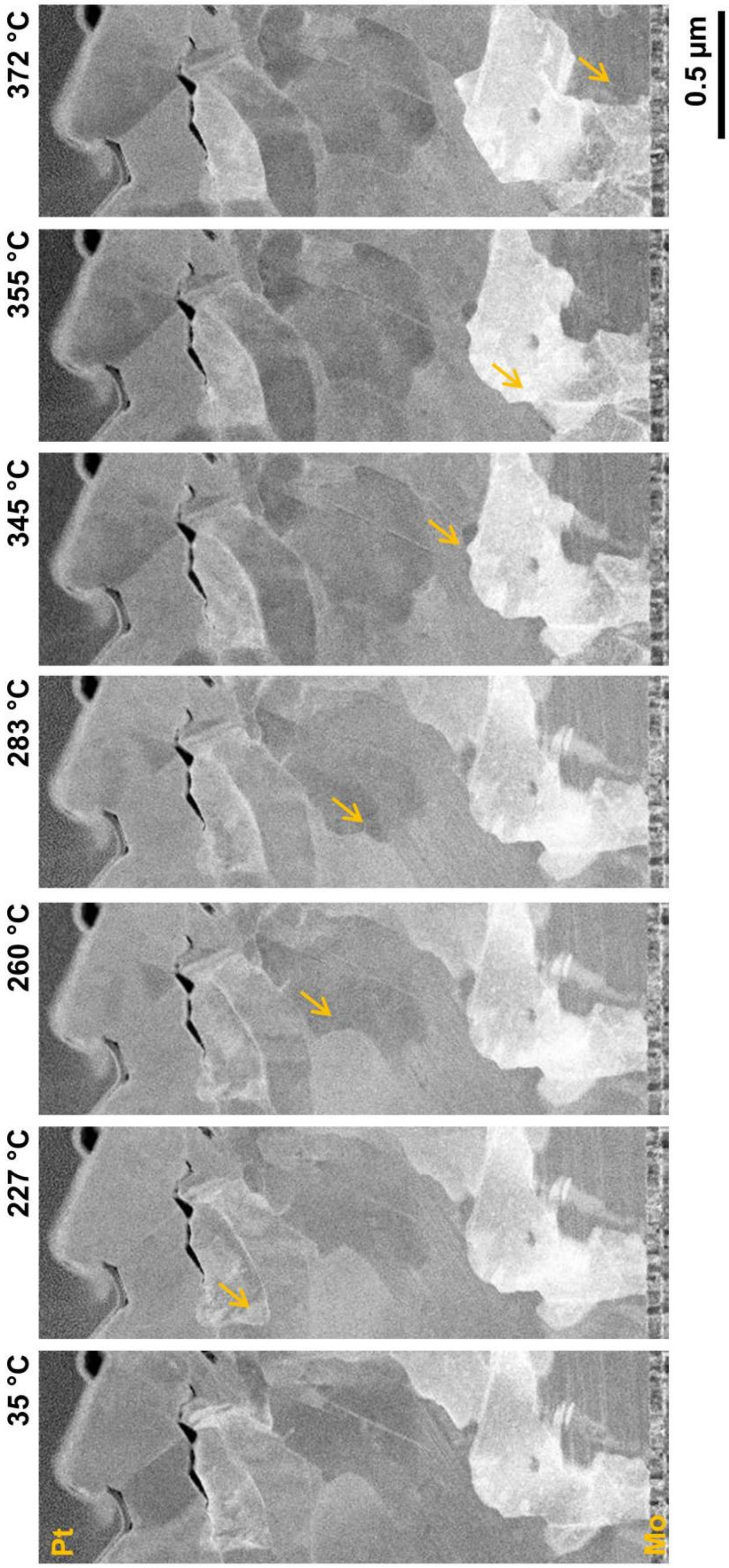

Figure 4.13 LAADF images of the sample 1.3, acquired during *in-situ* heating at various temperatures. Yellow arrows indicate the movement of GBs with time, which can be correlated with Cu in-diffusion to the Cu-poor CIS.

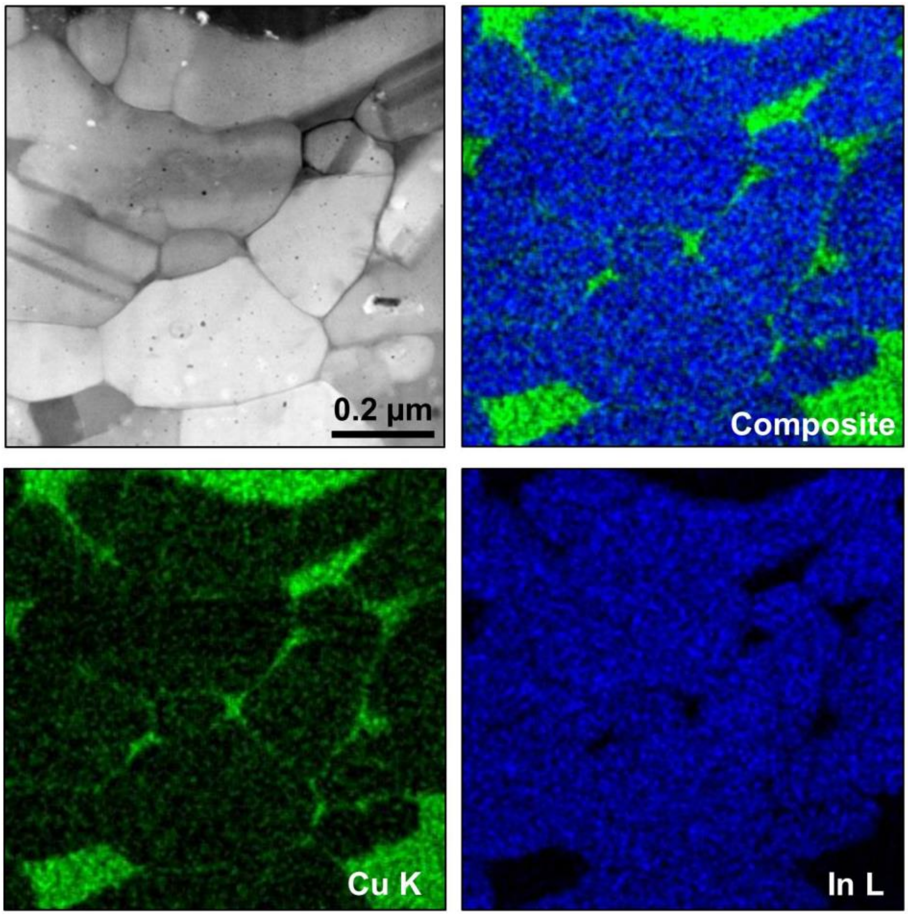

Figure 4.14 STEM-BF image from a middle part of the Cu-poor CIS with thicker Cu-Se capping layer after heating. Cu, In and composite maps show the elemental distribution in the grains as well as at the GBs.

Transmission Kikuchi diffraction (TKD) was additionally performed†† to detect the local orientation of the grains and to estimate the GB planes on the heated TEM lamella. TKD is an SEM-based technique that provides grain size and orientation, texture, GB characteristic, phase and deformation information. It is very similar to the electron backscatter diffraction (EBSD) technique, although, unlike EBSD, an electron-transparent sample is scanned and the diffraction pattern is collected below the sample by a similar detector. By this way, the spatial resolution is increased by an order of magnitude.[91] The grain orientations are visible on the TKD orientation map shown in Figure 4.15. According to the obtained results, GBs close to {100} and {110} tend to change in a way that they eventually become {111}, although some of the {110} did not change. It should be noted that here these GB planes are denoted according to the cubic structure, where the {111} corresponds to {112} in the equivalent tetragonal notation.

[††] The TKD analyses were performed by Dr. Norbert Schäfer and PD Dr. Daniel Abou-Ras.

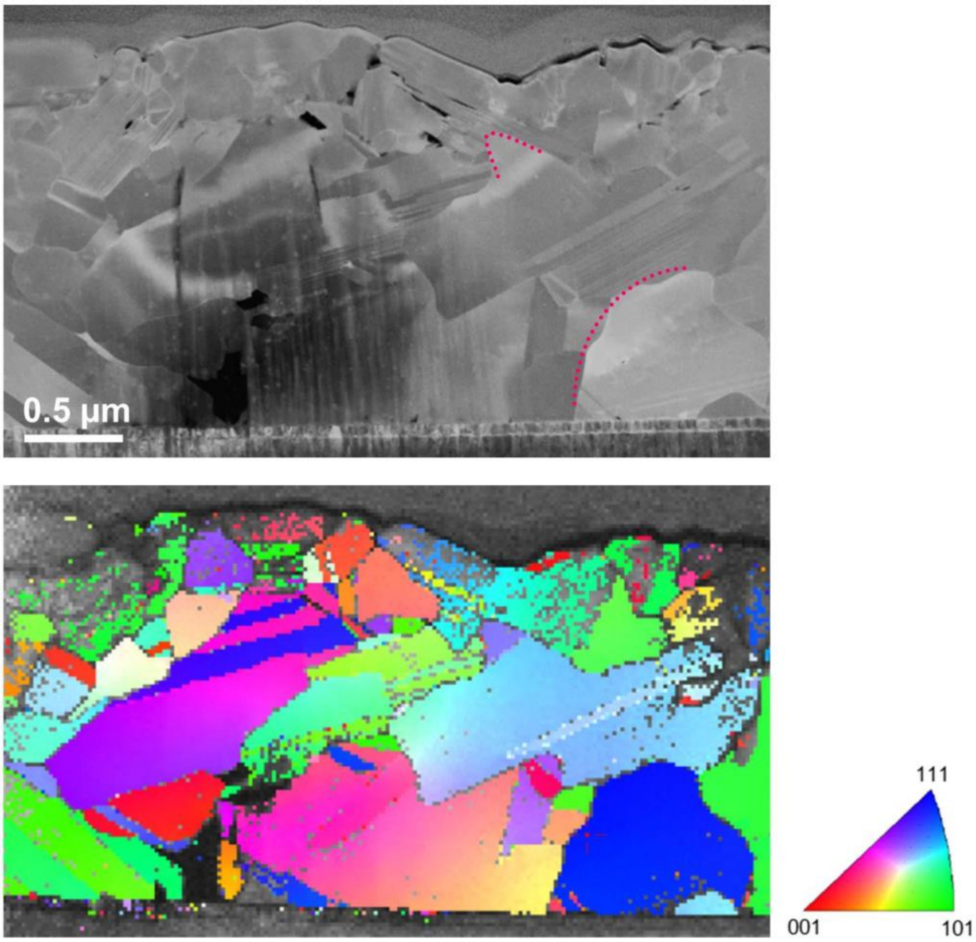

Figure 4.15 STEM-LAADF image from the same region as shown in Figure 4.2 (this time at 470 °C) as a reference image for the TKD orientation map. The red-dotted lines show {111} GB planes.

In the literature, there are proposed models to explain the effect of Cu on the grain growth; those might help to explain why the recrystallization was observed only in the samples with a $Cu_{2-x}Se$ capping layer. The first of these models is related to stress: when Cu incorporates into the Cu-poor CIS lattice, the crystal structure expands and compressive stress builds up in the absorber due to the use of rigid substrates.[92] The formed stress is then relaxed by the migration of GBs, as proven by *in-situ* XRD analysis in combination with modelling.[93] A second model is related to the GB energy. In a kinetic grain growth study, during the annealing of absorbers with various [Cu]/[In] ratios, the authors found that increasing the Cu content in the CIS absorbers reduces the activation energy for GB motion, resulting in larger grains.[28] A final study explains this phenomenon with diffusion and mobility of the cations in the chalcopyrite phase. They show that the incorporation of Ag, which is more mobile than Cu, lowers the recrystallization temperature for the same $CuInS_2$ absorber compared to the equivalent Cu samples.[94]

4.2. Investigation of the recrystallization by growth interruption study

The initial part of the study provided the first direct *in-situ* imaging on the crucial second stage of the CIS fabrication process. Structural and chemical changes during the recrystallization of CIS absorbers were proven via LAADF imaging. The results agreed quite well with previous studies, which were typically carried out at larger length scales using various techniques and/or routes. However, the agreement was not perfect with the previous EDXRD measurements, where PD signals disappeared after the recrystallization, whereas the present STEM *in situ* results point to a continued presence of some PDs even after recrystallization.[31, 33] Therefore, the study continued with post-growth analyses on growth-interrupted and growth-finished samples that were fabricated in a co-evaporation chamber with continuous material support, in a similar fashion to those samples used for EDXRD.

The second sample set (Table 4-1) was grown as follows: one piece of the absorber was removed from the co-evaporation chamber at the second stage, before the recrystallization, and is henceforth called ‘growth-interrupted’. For the remaining piece, the second and third stages were completed (Figure 2.3), and the second sample is thus called ‘growth-finished’. A lower growth temperature, 450 °C, than usual was applied in this study as it is essential to keeping the total energy consumption lower and to enabling the use of polymeric substrates for flexible solar cell applications. The microstructure and chemistry of the two samples are compared by LAADF imaging and EDXS.

LAADF images of the second sample set are shown in Figure 4.16 (a)–(b). The lower section of the growth-interrupted sample shows columnar grains (indicated by a purple band). In the top section, the grains are larger with a high density of defects, clearly visible from the strain-induced bright contrast of these features in the LAADF images. The growth of quaternary CIGS can be understood by considering the simpler ternary parent system. According to the In_2Se_3-Cu_2Se pseudo-binary phase diagram, shown in Figure 2.4, during the growth of CIS the crystal structure transforms from hexagonal In_2Se_3 to tetragonal CIS by passing through hexagonal layered (β-$CuIn_5Se_8$) and tetragonal stannite-type (β-$CuIn_3Se_5$) intermediate crystal structures.[95-97] During these transformations, the Se sub-lattice transforms from …*ABABAB*… stacking to …*ABCABC*… stacking in the <221> direction from the {110}-projection. Rodriguez-Alvarez *et al*. proposed a mechanism for the change of Se stacking: Se layers undergo plastic deformation by dislocation movement.[95] If dislocation movement is pinned at some point during the growth or if the growth is interrupted, atomic planes with SFs might remain in the lattice. This proposed mechanism could explain the high defect concentrations in the growth-interrupted sample. In contrast, in the growth-finished sample, the columnar structure at the bottom of the film has disappeared, most probably during the recrystallization. Furthermore, the defect density in the growth-finished sample is much reduced.

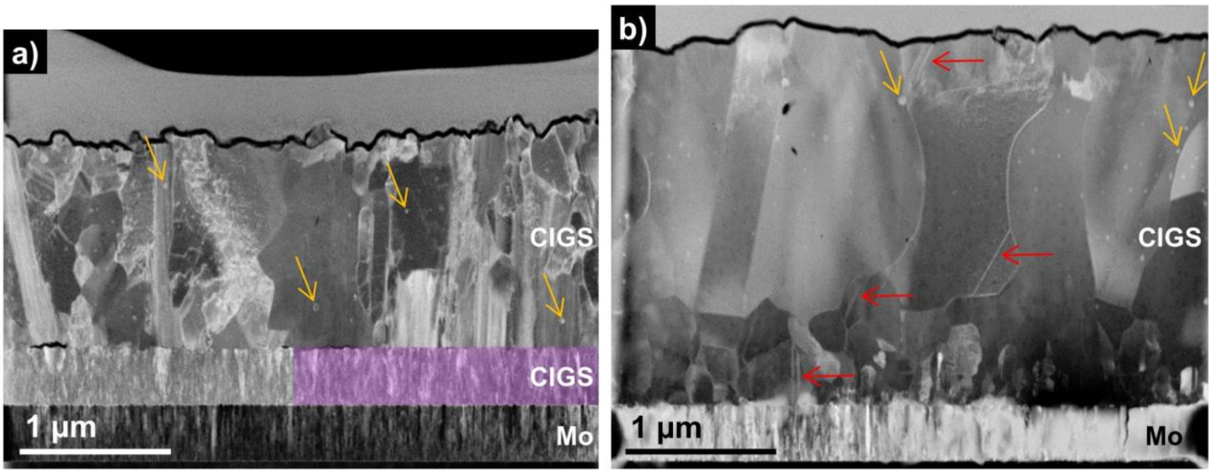

Figure 4.16 LAADF images of the second sample set: Cu-poor (a) growth-interrupted and (b) growth-finished CIGS samples. The purple-shaded area shows the Ga-rich columnar part. Red arrows on (b) show the remaining structural defects. The bright spots seen on both lamellae (shown by yellow arrows) are Cu agglomerates, which are known to form during the FIB sample preparation. Reprinted from E. Simsek Sanli *et al.*, J. Appl. Phys. 120, 205301 (2016)[83], with the permission of AIP Publishing.

The chemical gradient across the thickness of the absorbers was determined by EDXS line scans [Figure 4.17 (a)–(b)]. The line-scan acquired across the growth-interrupted sample reveals a Ga-rich layer at the bottom (the columnar section of the film) and an In-rich layer at the top of the absorber. Even though both In and Ga are evaporated during the first stage but stopped through the second stage, they have distinct profiles along the absorber. This nonuniform In/Ga composition is known to improve the device performance.[98] Three possible reasons are given in the literature for In/Ga gradient formation: growth temperature, Cu and Na concentrations in the absorber, and the relative size of In and Ga atoms.[99-102] During the second stage of the growth, the growing layer tries to lower the total strain by out-diffusion of the larger In atoms towards to forming a $Cu_{2-x}Se$ phase.[102]

For the growth-finished sample, a more gradual Ga gradient close to the back contact compared to the growth-interrupted sample was detected. The In-Ga-Se evaporation at the third-stage resulted in the second Ga grading observed close to the front contact. This type of composition profile is called double grading. Together with the position of the ‘Ga-notch’ within the absorber, double grading directly and strongly affects the device performance.[103, 104] The back grading is thought to improve the V_{oc} of the device by reducing the back-contact recombination.[98, 105] However, at the front contact, a high recombination has been detected when the Ga gradient is strong.[23] Hence, the Ga gradient in the front section of the absorber needs to be optimized to reduce recombination.

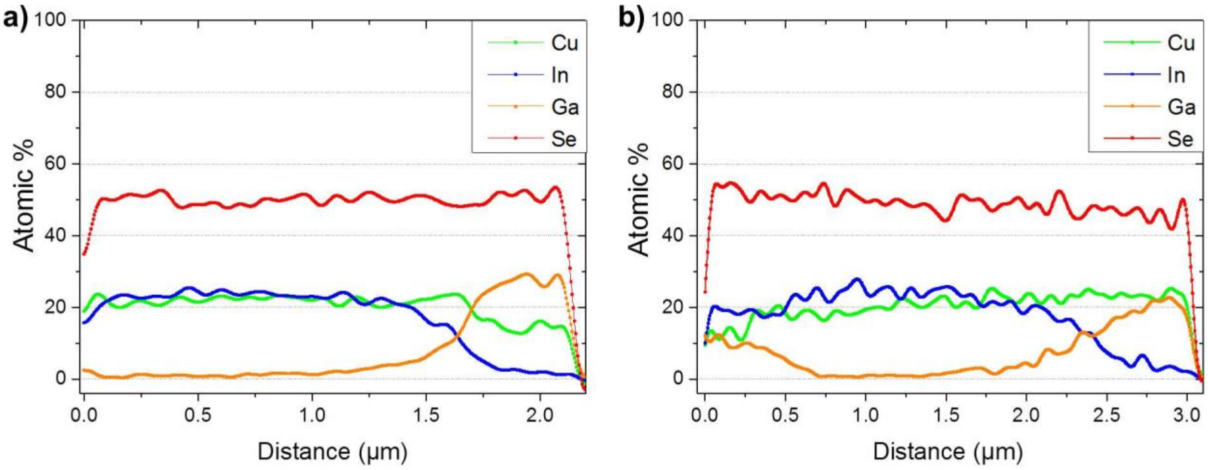

Figure 4.17 EDXS line-scans (from Pt to Mo side) of the second sample set. (a) Growth-interrupted and (b) growth-finished CIGS samples show In-Ga grading along the absorber layer. Reprinted from E. Simsek Sanli *et al.*, J. Appl. Phys. 120, 205301 (2016)[83], with the permission of AIP Publishing.

Dietrich *et al*. investigated the influence of the In-Ga grading on the microstructure.[106] Their EBSD results showed an inversely proportional relationship between the integral Ga concentration and the grain size. It means that the morphology along the CIGS lamellae might already give compositional hints: the lamellar part of the growth-interrupted sample [Figure 4.16 (a)] and the smaller grains on the top and bottom parts of the growth-finished absorber [Figure 4.16 (b)] are Ga-rich.

In the growth-finished sample, closely-spaced PDs were not detected. However, a number of other structural defects, such as dislocations and individual PDs were still present in the grains even after the completion of the growth [some of them are indicated by red arrows in Figure 4.16 (b)]. Therefore, the last part of this study was focused on the imaging and spectroscopical investigations of individual structural defects from growth-interrupted and growth-finished samples in order to explain their nature as well as their possible evolution during the growth.

4.3. Detailed analysis of the structural defects

In this section, high-resolution STEM-HAADF imaging in combination with STEM-EELS was applied to gain insight into the structure and composition of the structural defects. After giving a comprehensive perspective to the experimental details on a defect-free CIGS structure in the following paragraph, the structural defects will be explained under four sub-sections: *i)* defects present in both growth-interrupted and growth-finished samples; *ii)* defects present only in the Cu-poor growth-interrupted samples; *iii)* defects present in the Cu-rich growth-interrupted sample; *iv)* defects present only in the growth-finished sample.

High-resolution images were acquired along the <110>-projection of the structure. In this projection, the CIGS crystal lattice shows dumbbells formed by closely spaced pure Se^{2-} and alternating In^{3+}/Ga^{3+} trivalent and Cu^{+} monovalent cation columns [Figure 4.18 (a)].

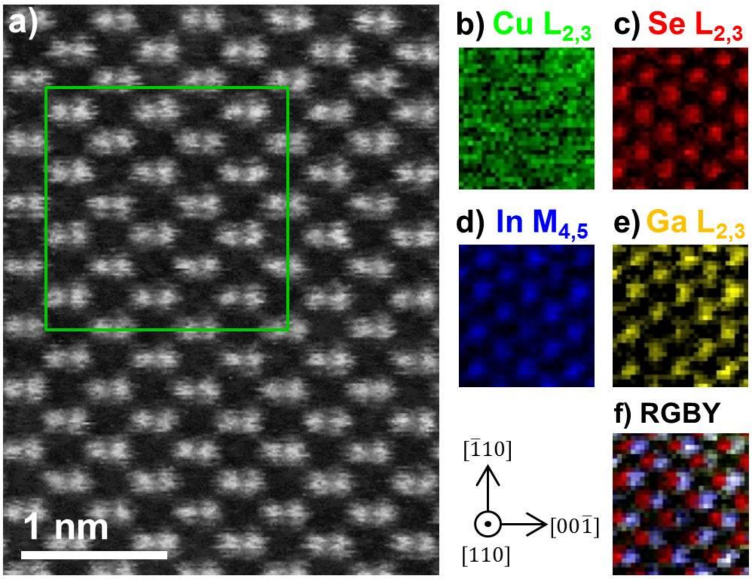

Figure 4.18 (a) HAADF survey image of a defect-free CIGS lattice along the <110>-projection. An EEL spectrum image was acquired from the region selected by a green square on the HAADF image. Elemental distribution maps extracted from the EEL spectrum image, showing the integrated (b) Cu-$L_{2,3}$, (c) Se-$L_{2,3}$, (d) In-$M_{4,5}$ and (e) Ga-$L_{2,3}$ intensities. (f) The composite image was formed by overlapping the simultaneously acquired HAADF image with a color-coded combination of the elemental distribution maps. Reprinted from E. Simsek Sanli *et al.*, J. Appl. Phys. 120, 205301 (2016)[83], with the permission of AIP Publishing.

However, the simultaneous presence of Cu and In/Ga cations in the same atomic column in <110>-zone axis orientation makes distinguishing between column type from images alone challenging. In this case, EEL SI acquisition enables the identification of atom-column compositions from selected regions of a sample. A reference SI was acquired from the defect-free region indicated by the green square on the HAADF image shown in Figure 4.18 (a). The corresponding Cu, Se, In and Ga elemental distribution maps [Figure 4.18 (b)–(e)] are shown with green, red, blue and yellow colors, respectively. The intensities on the elemental maps were normalized to a range from 0 to 1 for simplicity and should therefore not be interpreted in terms of absolute sample compositions. The position of the Se and cation columns are summarized for visual clarity in a red-green-blue-yellow (RGBY) image [Figure 4.18 (e)] displaying a superposition of the Cu, In, Ga and Se elemental distribution maps. This approach proved to be particularly helpful in elucidating the structure and chemistry of individual structural defects in CIGS.

4.3.1. Defects in both growth-interrupted and growth-finished samples

Independent of the point at which the growth was interrupted the following five structural defects kept their characteristic structure and composition: stacking faults (SFs) and twin boundaries (TBs) showed homogeneous elemental distribution, whereas grain boundaries (GBs), tilt boundaries and dislocation cores showed striking cation redistribution –Cu enrichment and In depletion– with slight Se depletion.

- **Stacking faults**

SFs are common-detected defects in chalcopyrite CIGS on the {112} planes. SFs are planar defects where the long-range stacking sequence of the crystal structure is interrupted. The insertion of an additional plane to the perfect crystal produces an extrinsic SF (ESF), whereas the deletion of a lattice plane produces an intrinsic SF (ISF). An ESF and an ISF are shown in Figure 4.19 (a) and Figure 4.20 (a), respectively. The determination of the type of stacking fault present in these samples was carried out as follows: in Figure 4.19 where the stacking fault is observed in the <110>-projection, the stacking sequence of Se across the defect along the <221> direction is …*ABC***B***ABC*…, identifying an ESF [Figure 4.19 (a)], as there is an additional **B** plane. Spatially resolved EELS results show homogeneous Cu, In and Se elemental distribution at the ESF [Figure 4.19 (b)–(d)]. A composite image [Figure 4.19 (e)] is formed by superimposing the simultaneous HAADF image, acquired during the SI acquisition, and the Cu, In, Se elemental distribution maps extracted from the SI. Note that no Ga map is presented since the ESF and most of the observed defects, which will be presented in this work, were localized in the Ga-poor region of the CIGS sample. This made the extraction of the low-intensity Ga $L_{2,3}$ edge, which also overlaps with the Cu $L_{2,3}$ edge, not reliable.

In Figure 4.20, the Se stacking across the defect is …*ABCA***.***CABC*…, where the B plane is missing in the <221> direction, which indicates that there is an ISF. The ISF lies on the

{112} plane on the same projection of a CIS[‡‡] sample. Like ESFs, ISFs also exhibit a homogeneous elemental distribution [Figure 4.20 (b)–(e)].

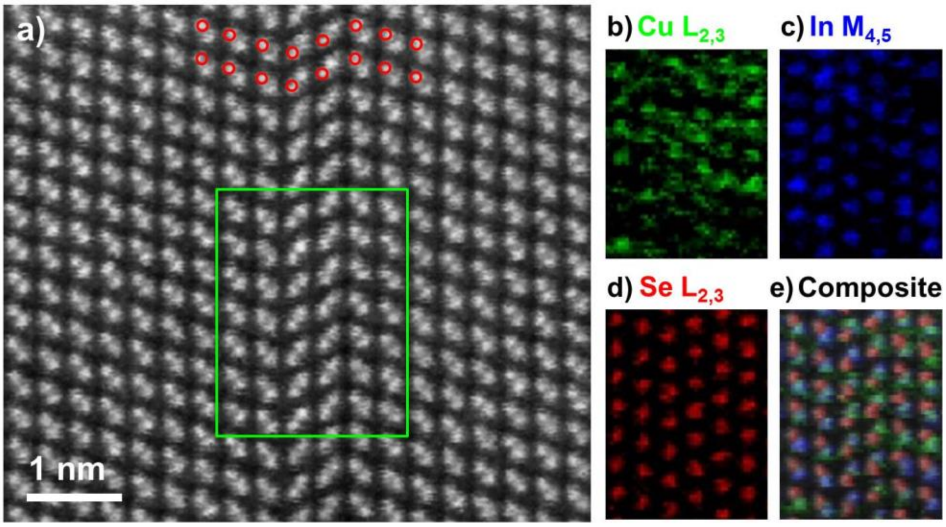

Figure 4.19 (a) HAADF image of an extrinsic SF, and (b)–(d) the corresponding EELS elemental distribution maps from the area denoted with green rectangle on the HAADF image. (e) A composite map was formed by superimposing the RGB color-coded image with a simultaneously acquired HAADF image. Red circles on the HAADF image show Se columns across the ESF. The figure is reprinted by permission from Wiley & Sons, Inc.: Compositional and electrical properties of line and planar defects in Cu(In,Ga)Se_2 thin films for solar cells – a review by D. Abou-Ras *et al*. Phys. Status Solidi RRL 10, No.5 (2016)[107].

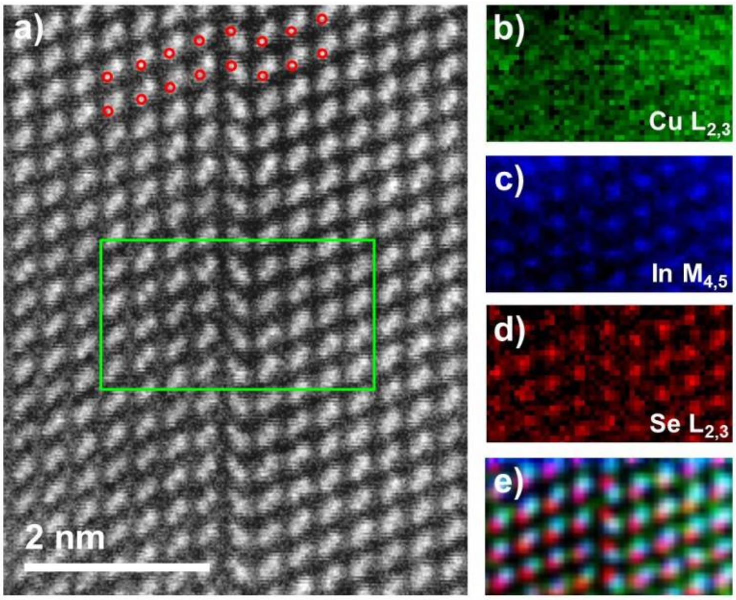

Figure 4.20 (a) HAADF image of an intrinsic SF. The elemental distribution maps are extracted from the SI acquired and show (b) Cu, (c) In and (d) Se. (e) RGB color-coded map shows the homogeneous elemental distribution.

[‡‡] In the scope of this thesis not only CIGS but also Na incorporated CIS samples, which have defects with similar characteristics, were probed. A short summary of those samples is given in the section 4.3.3.

Such cation-Se terminated SFs extend across the whole grain without causing local compositional changes and terminate almost systematically at GBs. Indeed, previous studies showed that the SFs with cation-Se termination do not need to include elemental redistribution, and therefore they do not create deep-level defects, which would risk impacting the absorber properties.[108, 109]

A smaller number of SFs terminate inside the grains, in which case they always intersect with other defects such as (partial) dislocations. The interaction of an ESF with Frank partials and their effects on the elemental distribution as well as the impact of such a defect on device performance were also investigated and discussed in more details in section 4.3.2.

❖ Σ3 twin boundaries

Other PDs that are often observed in CI(G)S absorbers are TBs, which are very similar to SFs. A TB from the growth-interrupted CIGS sample is shown in Figure 4.21 (a). As with SFs, Cu, In, and Se elemental maps [Figure 4.21(b)–(d)] and the composite image [Figure 4.21 (e)] show a homogeneous chemical distribution around the TB. The cation-Se termination on {112} planes at the TB is depicted by red (Se) and black (cation) circles overlaid on the HAADF image. The formation mechanism of Se-cation terminated twin boundaries is a 250° (= 70°+180°) rotation around the <110> axis. A similar type of coherent TB is explained in detail for the sphalerite structure by Holt and Yacobi.[110] It was described as an upright (ortho) TB. Due to the correct (compared to an undefected structure) sequence of cation-Se bonds at this boundary, the interplanar distances remain the same as in the grain interiors. The TB is a special type of Σ boundaries (Σ3).[111]

The lamellar twins on {112} planes are the most-frequently found boundaries in CI(G)S absorber layers due to their low formation energies.[112] Extensive work has been performed experimentally and theoretically on Σ3 {112} TBs.[108, 113, 114] In a recent paper, Mirhoisseini *et al*. theoretically showed that Σ3 (112) boundaries shift both the VBM and the CBM with respect to the grain interiors.[115] This way electrons are attracted to the boundary, but the boundary also repels the associated holes such that the carrier recombination stays low. It has also been found that cation-Se-terminated Σ3 TBs do not create gap states, so they do not affect the performance of the solar cell. The only possible effect might arise in the case of a close proximity of a large number of such PDs, which could result in a change in local structure, as was explained for CdTe thin-film solar cells.[109]

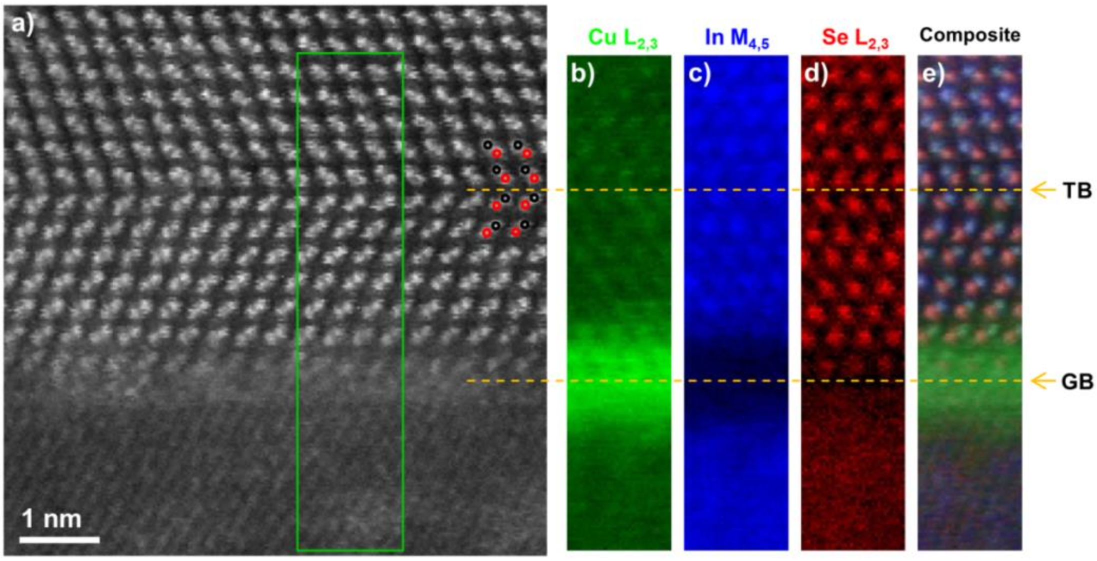

Figure 4.21 (a) HAADF image of a Se-cation terminated TB and a random GB from the growth-interrupted sample. The upper grain is oriented in <110>-direction. (b)–(d) Elemental distribution maps extracted from the EEL spectrum image, showing the Cu, In, Se, respectively. (e) RGB composite image was superimposed onto the simultaneously-acquired HAADF image. Reprinted from E. Simsek Sanli *et al.*, J. Appl. Phys. 120, 205301 (2016)[83], with the permission of AIP Publishing.

❖ Random grain boundaries

Due to the polycrystalline structure of CI(G)S absorbers, the most common structural defects are GBs. In Figure 4.21 (a), there is a GB in between the upper grain, oriented in <110>-direction, and the bottom grain, which is oriented in an unknown direction. Therefore, it is not possible to resolve the atomic columns on both sides of the GB simultaneously. The present GB is denoted as a ‘random’ GB, because there is no predetermined, high symmetry relation between these two grains. At this random GB, a clear chemical change was detected at the cation positions, with a very strong increase in the amount of Cu as shown in Figure 4.21 (b)–(e) by EELS spectrum imaging as well as by EELS line-scan analysis in Figure 4.22. The Cu enrichment at the GB region is an indication of the likely presence of Cu_{In} antisite[§§] defects, where the excess Cu atoms are at the In sites. Cu-rich cation columns (with a large number of such antisite defects) can in fact be found in the terminating layers of the upper grain. At the final plane of the upper grain (just above the yellow dotted line in [Figure 4.21 (d)]), a slight Se depletion is visible. Careful examination also suggests the presence of an increase in oxygen content at the GB, although this finding remains ambiguous owing to the overlap of the In-M and O-K edges in the EEL spectra. Although the presence of oxygen cannot be confirmed unambiguously, previous experimental studies on random GBs by means

---

[§§] An antisite defect occurs when an atom of a compound occupies the site of another chemical species of the compound.

of atom-probe tomography[116] confirmed increased oxygen concentrations at random GBs, whenever a reduced Se signal was detected. This anticorrelation of Se and O indicates that O atoms occupy the Se sites, O_{Se}.

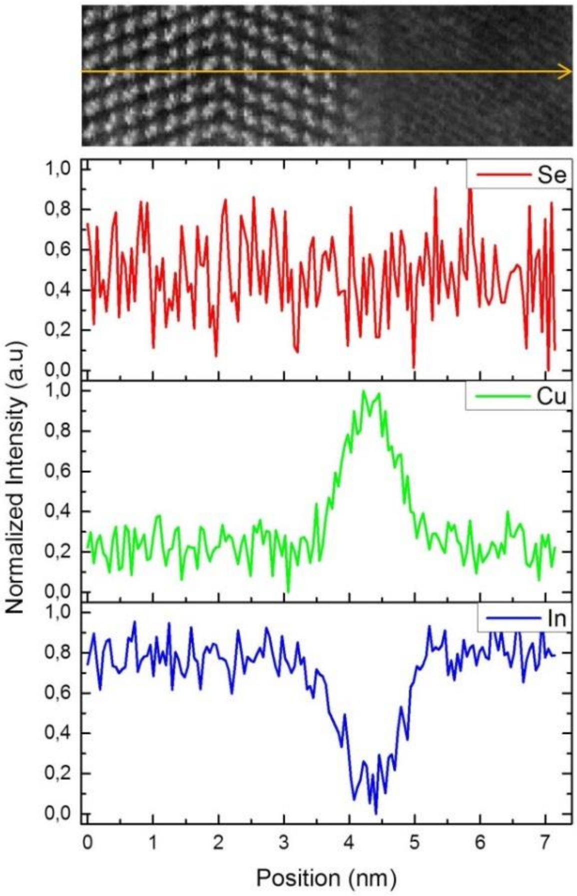

Figure 4.22 The STEM-EELS line scan shows homogeneous elemental distribution at the TB and the elemental redistribution at the GB.

In this particular lamella from the second sample set no signal which can be attributed to Na impurities was detected, since a Na-diffusion barrier was deposited between the SLG and Mo back contact. In the case of the CIS samples where a NaF layer was deposited before the CIS deposition, it was not possible to extract the Na-K edge either. This is due to the overlap with the intense Cu-$L_{2,3}$ edge and the very low concentration of Na (0.1-1at %).

As discussed in the previous sub-section, higher Cu diffusion along the GBs than within the grain interiors may be regarded as a reason for the detected Cu enrichment at the GBs, even in the growth-interrupted CI(G)S layer, which at no point during the co-evaporation process exhibited a Cu-rich composition. In the growth-finished sample shown in Figure 4.23; however, the last deposition stage was In-Ga-Se. In that case, the reason for Cu enrichment and In depletion at the GBs may be the compensation of a slight Se depletion.

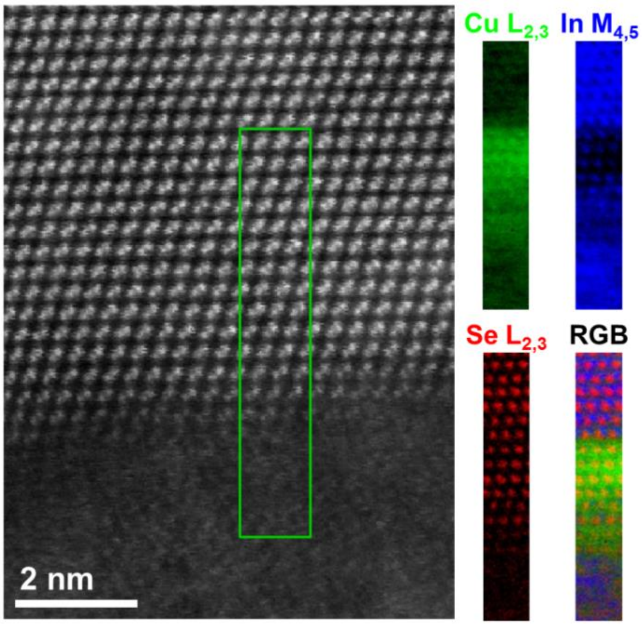

Figure 4.23 HAADF image of a random GB from the growth-finished sample and the corresponding Cu, In and Se elemental maps from the selected region. The difference of the chemical profile, the width of the Cu-rich region, is probably due to the geometrical effect. This GB is not an edge-on boundary. Reprinted from E. Simsek Sanli *et al.*, J. Appl. Phys. 120, 205301 (2016)[83], with the permission of AIP Publishing.

The type, quantity, mobility, electrical activity and possible effects of GBs on the performance of the solar cell are still puzzling for researchers.[116-125] Despite the presence of numerous GBs and without any heat/chemical treatment –unlike CdTe or Si–, polycrystalline CIGS shows high power-conversion efficiencies. In recent work, Yan *et al.* theoretically showed that at GBs deep gap states are formed in both CdTe and CIGS absorbers.[125] These gap states are harmful to the solar cell performance, and they have to be avoided, if the performance needs to be optimized. The removal of these gap states appears to happen spontaneously in CI(G)S by chemical modification, specifically by the creation of Cu_{In} and O_{Se} antisites.[125] The experimental results obtained here are thus in agreement with these theoretical predictions: the elemental redistribution observed at the GB region in CI(G)S helps the system to remain electrically benign. Therefore, a high concentration of such GBs does not play a crucial role for the CIGS solar cells' performance.

❖ Tilt boundaries

Less frequent, although found in both growth-interrupted and growth-finished CI(G)S samples, are tilt boundaries. Figure 4.24 and Figure 4.25 show two tilt boundaries with a 113° and 105° rotation along the <110> axis from the growth-interrupted and growth-finished samples, respectively.

As in the case of GBs, Cu enrichment in combination with In depletion was detected at the tilt boundaries. Se exhibits a relatively homogeneous distribution at the boundary region. Few darker Se columns at the tilt boundary, which can be interpreted as Se vacancies, probably (in part) occupied by oxygen atoms, are visible.

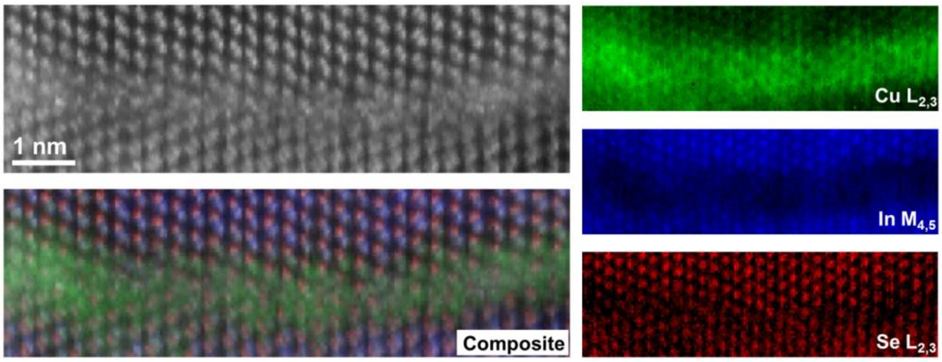

Figure 4.24 Simultaneously acquired HAADF image of a tilt boundary with 113° rotation angle from the growth-interrupted sample. Cu, In and Se elemental distribution maps from the growth-interrupted sample. The red-green-blue composite image is superimposed on the simultaneous HAADF image. Reprinted from E. Simsek Sanli *et al.*, J. Appl. Phys. 120, 205301 (2016)[83], with the permission of AIP Publishing.

Even though, there is not any theoretical work concerning these specific tilt boundaries, defect segregation on a similar defect, a Σ3(114) boundary, was studied using first-principle calculations.[115] The results showed how the presence of Cu_{In} and O_{Se} antisites breaks the ‘wrong bonds’ and cleans the deep gap states formed due to the presence of them at the boundary.[115] Here, the term ‘wrong bonds’ is used to denote bonds with unfavorable atoms, such as anion-anion or cation-cation bonding.[126] Hence, having Cu_{In} and O_{Se} antisites is a beneficial mechanism, as is the case at GBs.

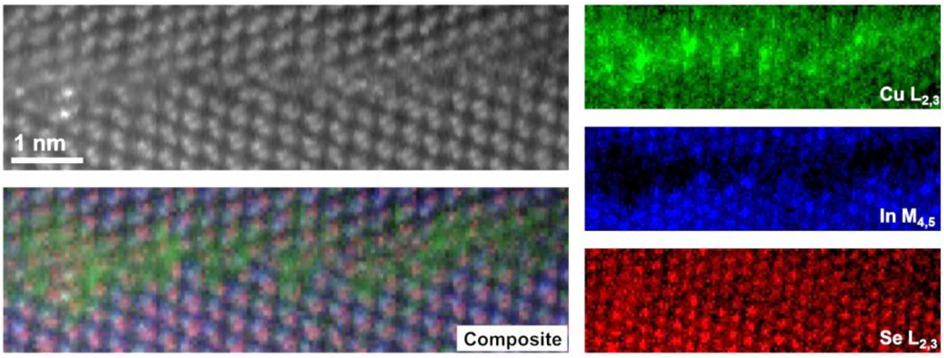

Figure 4.25 Simultaneously acquired HAADF image of a tilt boundary with 105° rotation angle from the growth-finished sample and the corresponding Cu, In and Se elemental maps extracted from the electron energy-loss spectrum. The composite image was formed by superimposing the HAADF image on a red-green-blue image composite map of Se, Cu and In, respectively. Reprinted from E. Simsek Sanli *et al.*, J. Appl. Phys. 120, 205301 (2016)[83], with the permission of AIP Publishing.

❖ Dislocation cores

A similar chemical segregation behavior was also observed at dislocation cores, *i.e.* twin-terminated edge dislocations. An overview of two dislocation cores and three Σ3 (112) TBs terminating at dislocation cores is shown in Figure 4.26 (a). Averaged sequential imaging (whereby a series of rapidly scanned images is aligned and averaged using rigid registration techniques) was used to obtain images with high signal-to-noise ratio of the two dislocation cores indicated on the overview image with yellow and purple boxes [Figure 4.26 (b) and (f)]. As before, EELS revealed that the stoichiometric composition is preserved at and across the Σ3 (112) TBs, while an anticorrelated redistribution of Cu and In is observed at the dislocation cores. This finding is illustrated in Figure 4.26 (c)–(e) with elemental distribution maps for Cu, In and Se at the upper dislocation core, and in Figure 4.26 (g)–(i) with the Cu, In, Se maps from the bottom dislocation core. Cu_{In} antisites were found at both dislocation cores. The slight Se depletion at the dislocation cores is attributed again to the presence of O_{Se} antisites, like in the case of GBs and tilt boundaries.

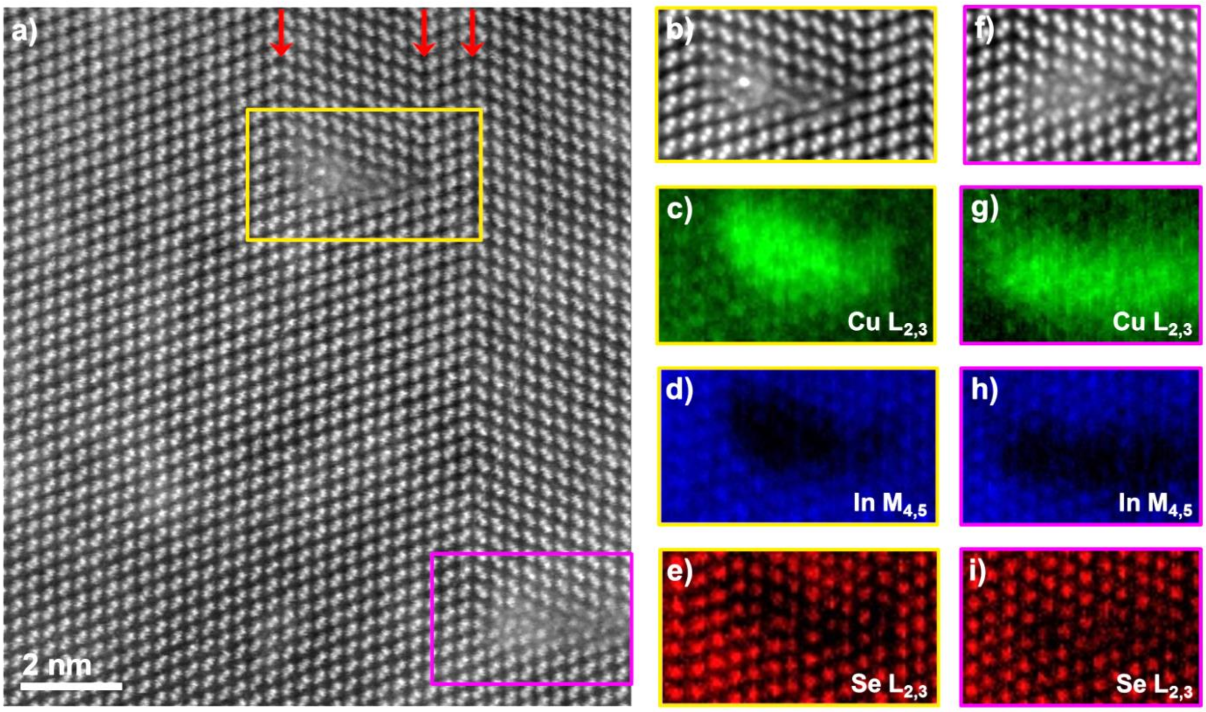

Figure 4.26 (a) HAADF image of two dislocation cores with associated twin boundaries from the growth-interrupted sample. (b, f) Averaged sequential images of the upper and bottom dislocation cores, indicated by yellow and purple boxes, are shown, respectively. (c)–(e) Elemental distribution maps from the upper dislocation core including two twin boundaries. (g)–(i) Elemental distribution maps from the bottom dislocation core and associated twin boundary. Reprinted from E. Simsek Sanli *et al.*, J. Appl. Phys. 120, 205301 (2016)[83], with the permission of AIP Publishing.

Edge dislocations were not studied in CI(G)S, but in Si. It was found that due to their high formation energies they are unfavorable to form in Si.[19] Moreover, due to the presence of dangling bonds, large structure volumes are needed to study them reliably with computational methods.[127] Hence, theoretical studies on dislocations in CI(G)S have so far only been carried out on (also experimentally observed) full 60°-mixed dislocations, which exhibit both edge and screw characters and are easier to handle numerically.[128, 129] 60° dislocation cores contain either cations (Cu, In, Ga) or anions (Se). In both cases, they exhibit dangling and 'wrong' bonds, which create charge accumulation towards the dislocation cores and form defect states.[128, 129] In the case of Cu depletion at the dislocation core, segregation of point defects, *i.e.* Na_{Cu}, can passivate the dislocation cores.[128] However, as stated above, edge dislocations were not theoretically studied. Further studies need to be done to comment on their effects on the performance of the CIGS solar cells.

4.3.2. Defects in the Cu-poor growth-interrupted samples

The drawback of atomic-resolution imaging is the poor observation statistics. However, after careful investigations on several grains from various depths of the growth-interrupted and growth-finished CIGS samples, the following three defects were detected only in the growth-interrupted CIGS samples: inversion boundaries, complex defects and Frank partial dislocations.

- **Inversion boundaries**

A Se-Se-terminated inversion boundary is shown in Figure 4.27. EEL spectrum imaging confirmed that the terminating ions are Se on both sides of the defect. The polarity of the Se-cation dumbbell becomes inverted when crossing the boundary. This is illustrated in the composite image where the red columns corresponding to Se are on the right side of the dumbbell in the leftmost section of the image, but on the left side of the dumbbell when crossing the boundary. Unlike in the case of the Se-cation-terminated TBs, due to the Se–Se termination of this defect, the distance between the {112} planes is larger (d_{112}=0.48 nm) than in the grain interiors (d_{112}=0.33 nm), which results in a dark line in the HAADF image (Figure 4.27). The distance between terminating columns on either side of the boundary is measured in the HAADF image as 0.37 nm, which compares very favorably to the calculated Se-Se distance of 0.35 nm for simulated CIS.[115] At this type of boundary, although the stoichiometric composition is preserved, strong atomic reconstruction is expected[114, 123], due to the unusual Se-Se 'inverted' bonds, which therefore create Se-dangling bonds. Indeed, the Se-Se termination at the boundary region creates a negative excess charge, which in turn might change the local band structure and could alter the absorber properties. Possible In_{Cu} antisite defects were predicted by calculations as necessary point defects to stabilize the anion-terminated boundaries.[114]

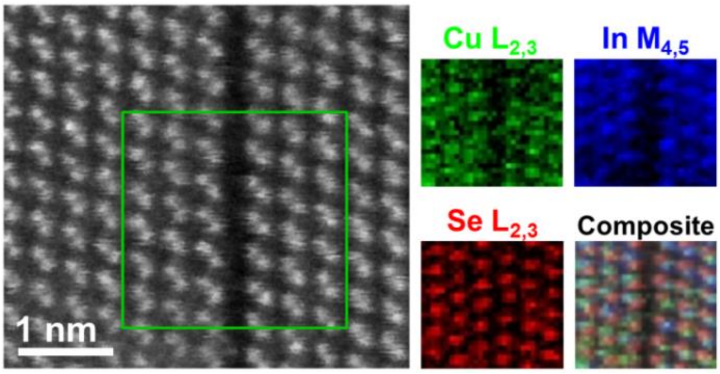

Figure 4.27 HAADF image of a Se-Se terminated inversion boundary and the Cu, In and Se distribution maps extracted from the area indicated with a green rectangle on the high-angle annular dark-field image. The composite image shows a homogeneous elemental distribution. This defect type was observed only in the interrupted sample. Reprinted from E. Simsek Sanli *et al.*, J. Appl. Phys. 120, 205301 (2016)[83], with the permission of AIP Publishing.

❖ 'Complex' defects

Figure 4.28 and Figure 4.29 show elemental distribution maps acquired on two complex defects in growth-interrupted CIGS samples. It was found that both defects have the overall characteristics of an ISF with one missing plane in the <221> direction. Both defects are formed on the {112} planes, although they possess clear structural differences. The defect depicted in Figure 4.28 has a similar structure to an inversion boundary; however, atomic reconstruction –Cu enrichment– is detected, although compensating positive charges (In_{Cu} antisites) would be expected. At this defect, it seems that it was energetically favorable to bind the excess Cu to the Se ions, in order to avoid negative excess charges. Figure 4.29 shows a related structure which includes a rotation of the cation (projected) site within the central plane and for which the planar distances between Se sites (the assignment of which was determined by EELS mapping) are preserved across the defected region. The red ball and arrow models on both figures show the equal planar distances of Se sites across the complex defects.

In both structures, the EELS maps demonstrate how the concentrations of Cu and In vary in an anti-correlated manner, while the Se distribution remains homogeneous. As before, the Se maps show slightly weaker intensity at the core of the defect suggesting a possible weak depletion in Se, although channeling effects may also play a role in generating this kind of contrast. SF-like complex defects might be the indicator of the initial stage of the $Cu_{2-x}Se$ phase that forms after enough Cu diffusion into the CI(G)S lattice had occurred.

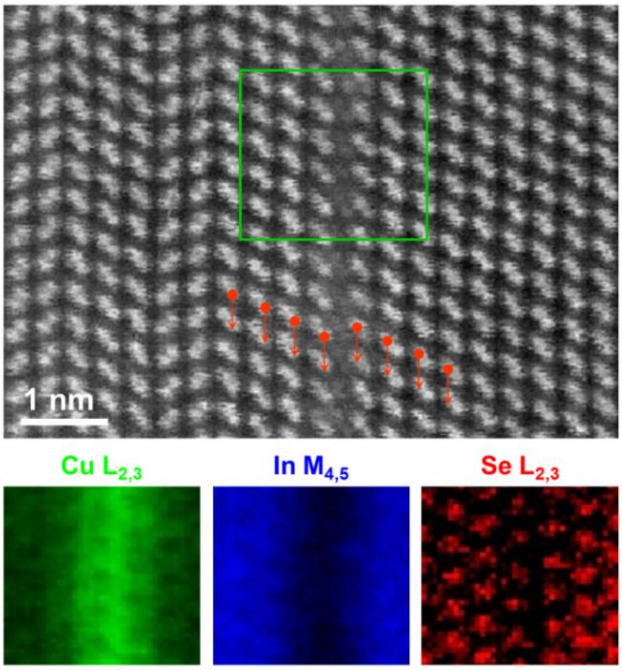

Figure 4.28 HAADF image of a SF-like complex defect from the growth-interrupted sample. Corresponding Cu, In and Se elemental maps from the denoted rectangle in the HAADF image. Red ball-arrow model shows Se columns across the defect region with constant and equal distances. Reprinted from E. Simsek Sanli *et al.*, J. Appl. Phys. 120, 205301 (2016)[83], with the permission of AIP Publishing.

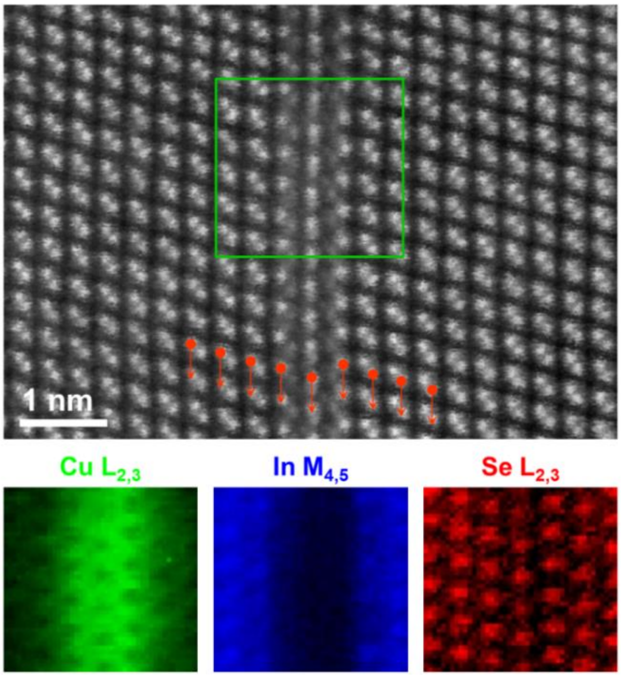

Figure 4.29 HAADF image of SF-like complex defect and corresponding Cu, In and Se elemental distribution maps from the denoted rectangle in the HAADF image. This defect type was only seen in the growth-interrupted sample. Red ball-arrow model shows Se columns across the defect region. Reprinted from E. Simsek Sanli *et al.*, J. Appl. Phys. 120, 205301 (2016)[83], with the permission of AIP Publishing.

❖ Frank partial dislocations

Frank partial dislocations in CIGS were neither observed experimentally by HR-STEM nor studied by density-functional theory (DFT) simulations before. A number of them were observed here during the HR-STEM analysis on the growth-interrupted CIGS. As it will be explained below, the cation redistribution around the partial dislocation cores was quite striking, so that it needed to be studied by DFT simulations to understand the characteristics and reasons of the elemental redistribution and its effects on the photovoltaic performance.

In Figure 4.30 (a), it is possible to detect a region with a slightly different stacking between two yellow boxes: ...*ABC***BA***BC*..., which creates an ESF. Interestingly, this ESF terminates within the yellow boxes drawn in the same figure. This termination is only possible due to the presence of partial dislocations separating the faulted regions from the perfect crystal.[130]

In the partial dislocations shown in Figure 4.30 (a), the Burgers vector, b = ±1/6 <221>, is normal to the plane of the fault. As a result, it cannot glide, indicating that this is an extrinsic Frank partial dislocation. Furthermore, similar to the case of Si[131] and based on its sessile nature and what has been found for PDs in CIS occurring on low-energy facet planes[58], it can be concluded that this is a grown-in defect and not the result of mechanical strain relaxation.

To study the properties of this extrinsic Frank loop by means of DFT calculations, a corresponding supercell with a SF bounded by two straight Frank partials was built.[***] As the observed defect was localized in the Ga-poor region of the sample, the simulations were carried out for a CIS structure. A slice of an extrinsic Frank loop, and its relaxed structure can be seen in Figure 4.30 (b). All atoms are fully coordinated, and no dangling bonds are found. Due to the symmetry of the chalcopyrite structure of CIS and its slip plane (112), in which this defect occurs, any transversal cut of a stoichiometric Frank loop in this material will consist of two structurally different transversal sections of the Frank partial bounding the loop, an α- and a β-core, and the extrinsic stacking fault between them. The inserted plane terminates in anions for the β-core [Figure 4.30 (c)] and in cations for the α-core [Figure 4.30 (d)].

[***] The supercell was built by Daniel Barragan-Yani.

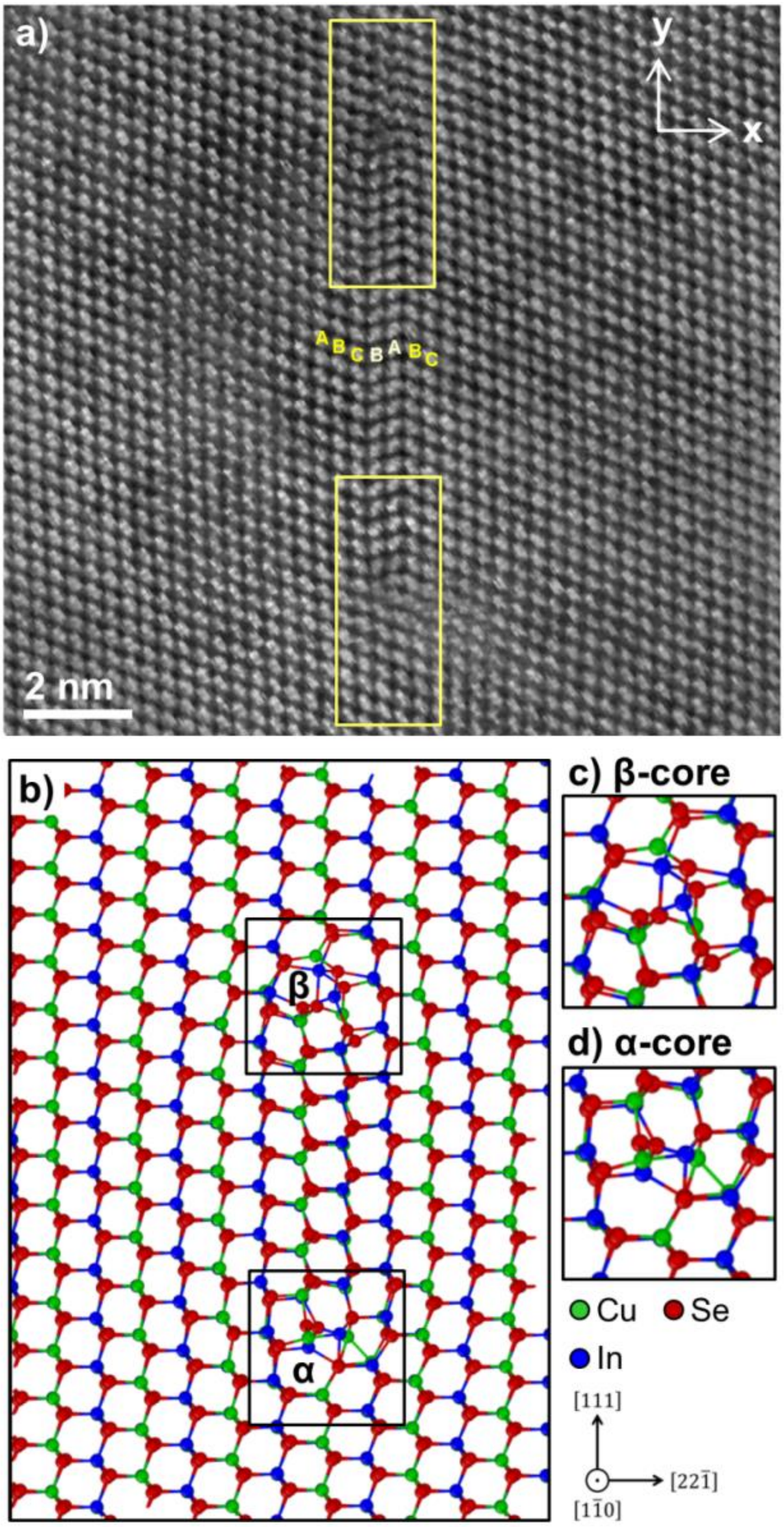

Figure 4.30 (a) HAADF image of the positive Frank partial dislocations associated with an extrinsic SF. Two yellow boxes indicate the top and bottom parts of the SF including partial dislocation cores (*β*-core in the upper box and *α*-core in the bottom one). The relaxed structure of an extrinsic Frank loop in CIS obtained with DFT. (b) Complete supercell showing the simulated loop, (c) *β*-core and (d) *α*-core. Reprinted figure with permission from E. Simsek Sanli *et al*., Point defect segregation and its role in the detrimental nature of Frank partials in Cu(In, Ga)Se$_2$ thin-film absorbers, Phys. Rev. B 95, 195209 (2017)[84]. Copyright (2018) by the American Physical Society.

The two regions indicated by the yellow boxes in Figure 4.30 (a) were analyzed by means of EELS, with the HAADF intensity distributions acquired simultaneously with the SIs. In this [1$\bar{1}$0] projection shown in Figure 4.31 (a), closely spaced Se and alternating In/Ga and Cu columns are visualized as an inset with red (Se) and black (Cu and In/Ga) balls. Se, Cu, and In elemental distribution maps were extracted from the acquired EEL spectra, and they are shown in Figure 4.31 (b)–(d) in red, green, and blue, respectively. Cu-rich clouds were found outside of both cores coinciding with a lower In signal intensity. Directly at the dislocation cores; however, the α-core shows a considerable excess of Cu, while the β-core exhibits only a slight increase in the Cu signal compared to the bulk material. Furthermore, immediately below the cores and to the side of the SF, a subtle drop in Cu signal is seen to coincide with a small increase in In.

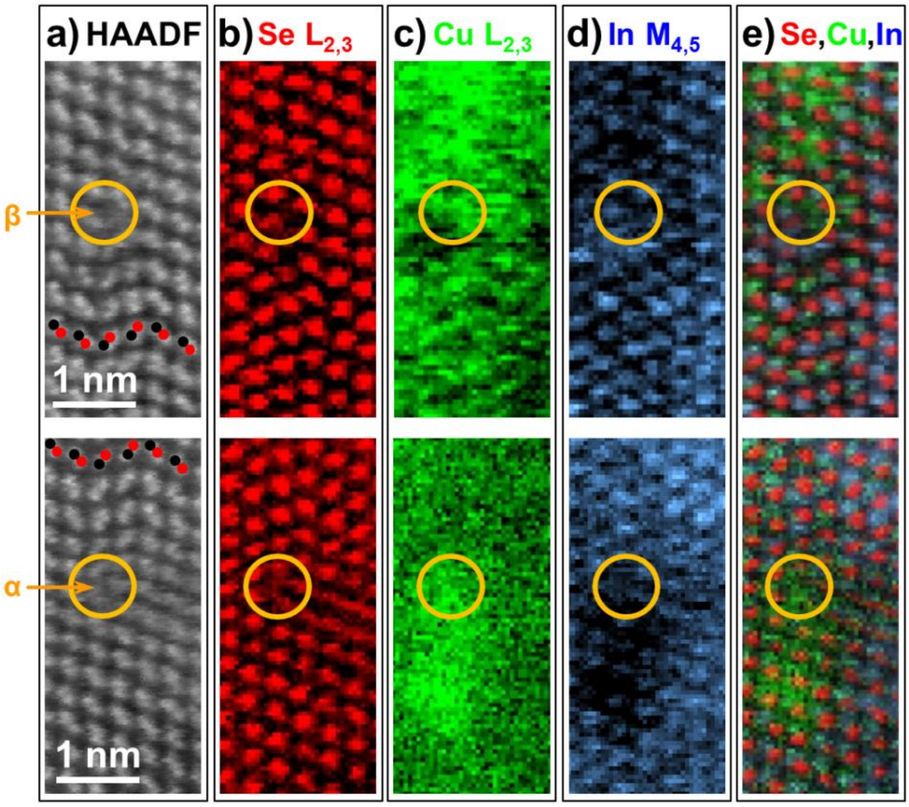

Figure 4.31 Two simultaneously acquired HAADF images from the areas indicated by yellow boxes on Figure 4.30 (a) show the association of the SF and the Frank loop (β-core in the upper panel and α-core in the bottom one). Dislocation cores are indicated by orange circles on the image. (b)–(d) Corresponding Se, Cu and In elemental distribution maps are shown in red, green, and blue colors. (e) RGB map is a color-coded superposition of the elemental maps. Reprinted figure with permission from E. Simsek Sanli *et al.*, Point defect segregation and its role in the detrimental nature of Frank partials in Cu(In, Ga)Se_2 thin-film absorbers, Phys. Rev. B 95, 195209, (2017)[84]. Copyright (2018) by the American Physical Society.

To understand such atomic rearrangements, the chemical decorations of Frank partials were studied by means of relative formation energies, E^{q}_{RFE}.[†††] Further details of the calculation and the formula of E^{q}_{RFE} are not given here, but can be found in the reference paper.[84] Non-stoichiometric Frank loop supercells were constructed by creating relevant point defects in the positions indicated by yellow circles in both Figure 4.32 (a)–(b) for the Cu vacancy and antisite defects ($\mathrm{Cu_{In}}$ and $\mathrm{In_{Cu}}$), while the **X**s mark the positions chosen for Cu interstitials. The chemical potentials, μ, for the Cu and In were chosen according to Pohl *et al.*'s work[132] to mimic the experimental Cu-poor, chalcopyrite phase conditions, in this case for $\mu_{\mathrm{Cu}} = -0.4$ eV and $\mu_{\mathrm{In}} \simeq -1.0$ eV.

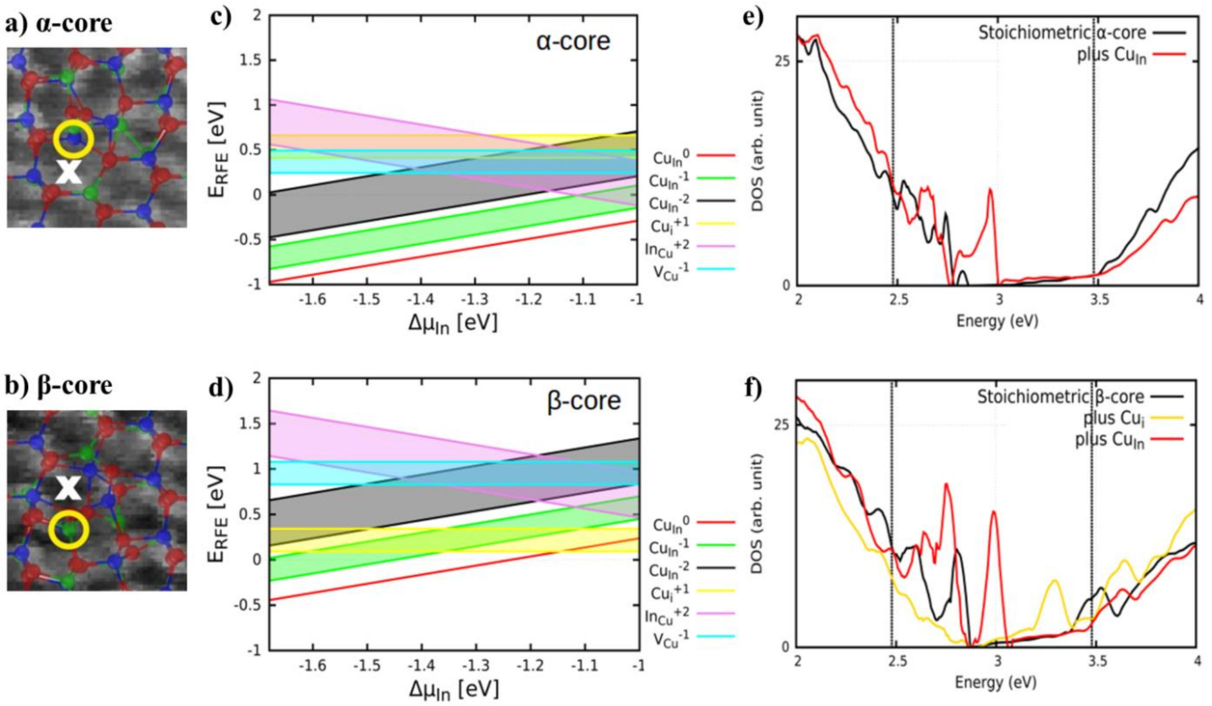

Figure 4.32 Simulated structures were superimposed on the HAADF images for the (a) α-core and (b) β-core. Relative formation energies of point defects inside the (c) α- and (d) β-cores of the Frank loop. The chemical potentials for Cu and In were chosen to mimic the experimental Cu-poor conditions, and charged defects are presented as colored bands rather than lines to show also their values when $0 \leq E_{\mathrm{F}} \leq 0.25$ eV. LDOSs of stoichiometric and decorated cores are shown for both (e) α-core and (f) β-core. The band gap of the bulk structure is marked by dotted vertical lines.[‡‡‡] Reprinted figure with permission from E. Simsek Sanli *et al.*, Point defect segregation and its role in the detrimental nature of Frank partials in Cu(In, Ga)$\mathrm{Se_2}$ thin-film absorbers, Phys. Rev. B 95, 195209 (2017)[84]. Copyright (2018) by the American Physical Society.

The relative formation energies for various defect types in the α-core and β-core are shown in Figure 4.32 (c)–(d), respectively. Relative formation energies of charged defects are

---

[†††] Relative formation energies were calculated by Daniel Barragan-Yani.

[‡‡‡] Calculations were done by Daniel Barragan-Yani.

presented as colored bands reflecting the range of possible Fermi levels ($0 \leq E_F \leq 0.25$ eV). In the cation-containing α-core, Figure 4.31 (c), the neutral and charged Cu_{In} antisites exhibit negative formation energies, which means that this defect would occur spontaneously and that the α-core has a tendency to be decorated by excess Cu. Within the relevant range of Fermi energies, the neutral antisite is the most stable configuration. Thus the Cu-rich dislocation core has no excess charge. Only when E_F is extremely close to the VBM, the In_{Cu} antisite does also have a negative E_{RFE}^{q}. Since these thermodynamic conditions do not occur in the real absorber, it can be concluded that the decoration of the α-core by neutral Cu_{In} is the main reason for the considerable Cu accumulation at the α-core observed in the experiments. For the Se-containing β-core, Figure 4.32 (d), all defect structures exhibit positive formation energies when $\Delta\mu_{In} = -1.0$ eV, which is the reason why compositional changes observed experimentally inside this core are less marked compared to its α counterpart. The presence of the neutral Cu_{In} antisite and some Cu interstitials explain the slight Cu increase found in this structure.

Therefore, the experimentally observed behavior of Cu at the dislocation cores, Figure 4.31, is in full agreement with the theoretical results. After unraveling the causes of such chemical changes inside the α- and β-cores, the local density of states (LDOS) of both structures were used, when decorated with their preferred point defects to study the effects of such non-stoichiometric structures on the electrical properties of the absorber layer. It was found that the presence of Cu_{In} inside both α- and β-cores induces a defect state [Figure 4.32 (e)–(f)] around the middle of the gap and enhances non-radiative recombination. Thus, the decorated Frank loop should be electrically active due to the presence of Cu_{In} inside the α- and β-cores. Moreover, although there are no dangling bonds in the stoichiometric structures, defect levels are also observed in the LDOS of the stoichiometric structures. These defect levels are thought to be strain induced; similar to what has been observed in the case of threading dislocations in GaN.[133]

To elucidate the nature of the Cu clouds detected around the cores (Figure 4.31), further HAADF and EELS experiments were conducted over a larger field of view. Similar line defects showed Cu clouds that extend up to 10 nm away from the dislocation cores (Figure 4.33). The absence of dangling bonds in the relaxed stoichiometric structures and the resulting absence of localized charges rule out electrostatic interactions, which is in contrast to the case of full dislocations reported by Dietrich *et al*.[128] The nonsymmetric distribution of the Cu clouds around the dislocations also provides a hint that they cannot be due to electrostatic potentials, which would imply only a radial dependence of the Cu distribution.

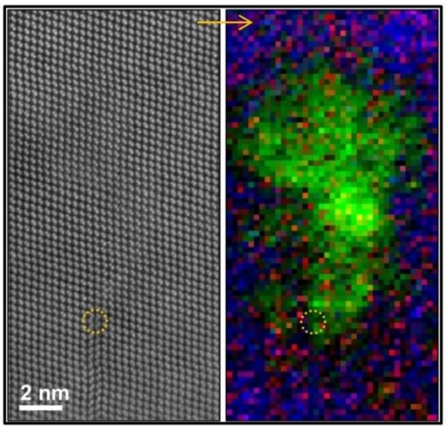

Figure 4.33 HAADF image (left) of a partial dislocation core and the corresponding EELS elemental distribution map (right) composed of Se (red), Cu (green), and In (blue) signals. The diffusion range of Cu is 5-10 nm. Reprinted figure with permission from E. Simsek Sanli *et al.*, Point defect segregation and its role in the detrimental nature of Frank partials in Cu(In, Ga)Se_2 thin-film absorbers, Phys. Rev. B 95, 195209 (2017)[84]. Copyright (2018) by the American Physical Society.

Therefore, strain was tested as a possible driving force of such atomic redistribution around the cores. GPA[81] was used to visualize the compressive and tensile strain fields associated with the dislocation cores. The main x and y axes, chosen for the strain analysis, are presented on the HAADF image in Figure 4.30 (a). Figure 4.34 (a)–(b) shows the corresponding components, ε_{xx} and ε_{yy}, of the strain tensor superimposed to the same HAADF image (with a 90° rotation to the left) to correlate visually the measured strain values to the exact atomic positions. The color bar indicates a change in strain from +7.5% tensile to −7.5% compressive for both the ε_{xx} and ε_{yy} components. The atoms at the SF, especially those near the dislocation cores, experience compressive strain. At the sides of the SF, the effect is inverted, and atoms experience tensile strain. At the SF, the atomic columns are displaced horizontally from their positions, at larger distances away from the dislocation cores along the x direction. It results in larger strain fields as is shown in the ε_{xx} map. In contrast, the vertical displacement is rather localized close to the dislocation core in the y direction. For comparison, the strain-field components for a pair of partial dislocations, ε_{xx} and ε_{yy}, were calculated from linear elasticity theory.[130] In Figure 4.34 (c)–(d), the theoretical strain distribution is shown, which reproduces the experimental result. Similarities in the positioning of the tensile and compressive regions between theoretical and experimental results give further proof that the defect studied with HR-STEM is indeed an extrinsic Frank loop. Since linear elastic results are divergent very close to the core, the results were bounded to a maximum of ±5%.

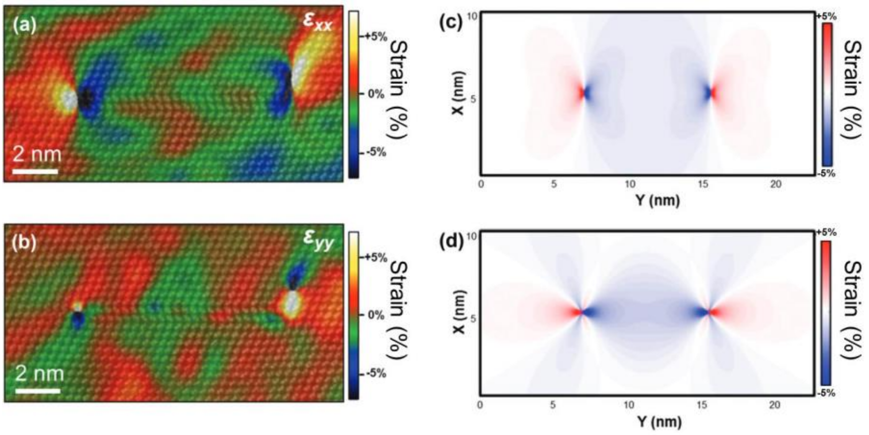

Figure 4.34 The HAADF image shown in Figure 4.29 (a) is superimposed with (a) ε_{xx} and (b) ε_{yy} strain components extracted by GPA. Strain fields for an extrinsic Frank loop as predicted from linear elasticity solutions (c) ε_{xx} and (d) ε_{yy}.[§§§] Reprinted figure with permission from E. Simsek Sanli *et al.*, Point defect segregation and its role in the detrimental nature of Frank partials in Cu(In, Ga)Se_2 thin-film absorbers, Phys. Rev. B 95, 195209 (2017)[84]. Copyright (2018) by the American Physical Society.

To reveal the nature of the Cu clouds, the mechanical coupling of this strain field to the defect thermodynamics was analyzed. The calculations are not given in this work, but can be found in the reference paper.[84] Calculations provided evidence that the Cu clouds detected outside of the core region probably consist of $\mathrm{Cu}_{\mathrm{In}}^{-2}$ point defects and the driving force for their formation is the interaction of the strain fields of the dislocations with these point defects. Also due to the strain, $\mathrm{In}_{\mathrm{Cu}}^{+2}$ antisites are predicted to accumulate in areas under compressive strain, providing a charge compensation mechanism. Although not as prominent as the Cu-rich clouds, they are observed by means of EELS [in the dotted circles in Figure 4.31 (d)].

Regarding the effect of such clouds on the electrical properties of a device containing dislocation loops like the one studied here, it has been pointed out in previous studies that the $\mathrm{Cu}_{\mathrm{In}}^{-2}$ antisite constitutes the most harmful hole-trap in CIGS absorber layers.[132] Thus, Cu clouds composed of such defects would also be detrimental for the efficiency of the device.

In the case of the quaternary compound CIGS, conclusions can be drawn by including Ga in this analysis. In such a situation, the expected In-rich clouds would include $\mathrm{Ga}_{\mathrm{Cu}}^{+2}$ along with $\mathrm{In}_{\mathrm{Cu}}^{+2}$, since both would respond similarly to strain due to the analogous ionic radius of In and Ga. It was shown that both $\mathrm{Ga}_{\mathrm{Cu}}^{+2}$ along with $\mathrm{In}_{\mathrm{Cu}}^{+2}$ are shallow donor defects.[132] Therefore, the finding that the presence of $\mathrm{Cu}_{\mathrm{In}}$ is the factor determining the detrimental nature would remain valid for CIGS.

[§§§] Theoretical strain field components were calculated by Daniel Barragan-Yani.

Since the calculated energy band diagrams suggest that the presence of Cu_{In} at the α- and β-cores induces deep midgap defect states, the annihilation of Frank loops during the CIGS growth is essential in order to obtain higher absorber qualities for record conversion efficiencies of the corresponding solar-cell devices.

4.3.3. Defects in the Cu-rich growth-interrupted samples

Two growth-interrupted CIS absorbers with 12 nm NaF precursor layer were analyzed to see the effects of Na incorporation and growth temperature on the structural defects. Two pieces from the same set of samples were removed from the co-evaporation chamber before and just after the recrystallization. Two growth-interrupted lamellae with Cu-poor and Cu-rich compositions are shown in Figure 4.35 (a)-(b), respectively. Independent of the composition and the recrystallization, both samples show similar microstructures: small grains with defects including closely-spaced PDs. In the scope of Stange *et al.*'s work, which was carried out on the same sample family, the conclusion was drawn that Na inhibits the growth of defect-free grains particularly at low growth temperatures of ~350 °C. This is achieved by reducing the Cu/In diffusion during the recrystallization.[134] That work explained the high defect concentration detected in the Cu-rich CIS sample as well.

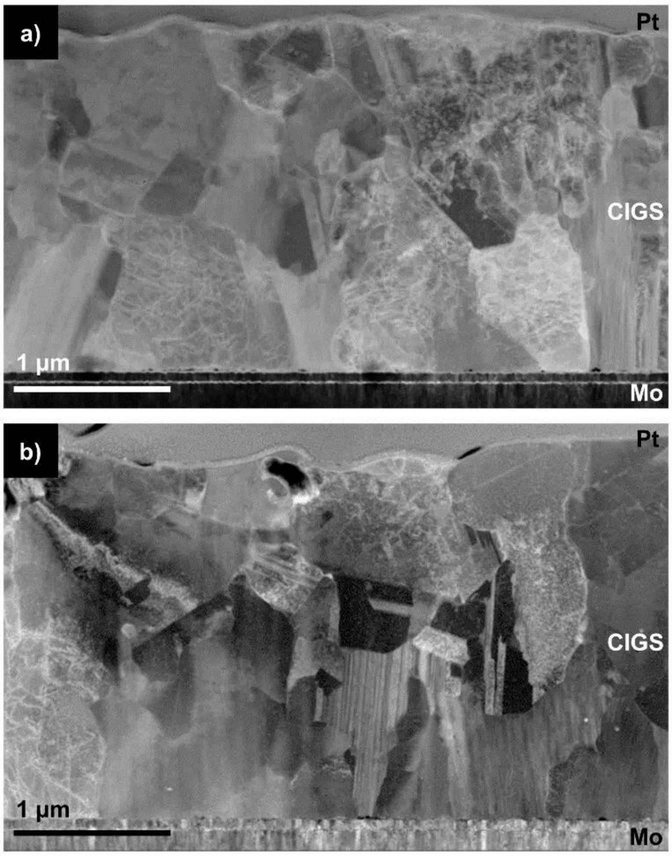

Figure 4.35 LAADF images of the fourth sample set: Na incorporated (a) Cu-poor growth-interrupted and (b) Cu-rich growth-finished samples.

The defect structures and elemental (re)distributions at the individual structural defects present in these samples were found to be the same as the Cu-poor CIGS absorbers, except for one defect, which was detected in the Cu-rich CIS samples as a striking CuPt-ordered phase inclusion.

- **‘CuPt-ordered’ phase inclusion**

During the growth of CI(G)S absorbers, metastable secondary phases with different ordering than usual are formed. Such a phase, in the form of platelets, was detected in the growth-interrupted Cu-rich CIS sample around the GBs (Figure 4.36). Previously, similar structures were described in the literature as a ‘CuPt-ordered’ CIS phase.[89, 135, 136] According to the literature, this phase is a metastable transition phase that forms during the ‘topotactical growth’[****].[89]

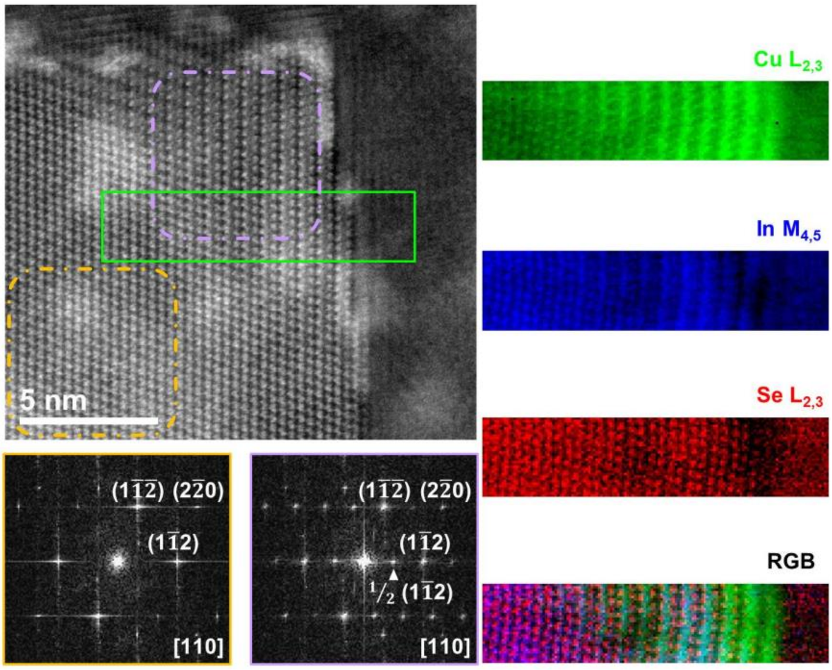

Figure 4.36 HAADF image of a ‘CuPt-ordered’ defect around a GB. Two Fourier transforms (FFTs) are extracted from the regions indicated by purple and yellow squares on the HAADF image. Additional spots are visible on the purple framed FFT, which was extracted from the ‘CuPt ordered’ region. Cu, In and Se elemental maps are extracted from the region selected with a green rectangle on the HAADF image. RGB color-coded image is shown for visual clarity.

In Figure 4.36 the HAADF image shows a morphological change of the {112} planes in the <110>-oriented grain around the GB region. On the upper right corner of the <110>-oriented grain, the lattice spacing was measured as d_{112}=0.67 nm, which is twice the

---

[****] The topotactical growth model is explained in section 4.3.4 in more detail.

chalcopyrite-type CIS lattice spacing, d_{112}=0,33 nm. Fourier transforms (FFTs) were extracted from the chalcopyrite and the 'CuPt ordered' regions indicated in Figure 4.36 by yellow and purple dashed boxes, respectively. The FFT, extracted from the 'CuPt-ordered' region, shows extra spots on the $^1/_2(1\bar{1}2)$ positions. In the literature, these extra spots are described as typical signs of 'CuPt-type ordering'.[136] The elemental distribution was elucidated through EELS elemental maps. A slight Cu enrichment, especially close to the GB region, is detected. The smeared columnar Cu and In signal, between the homogenously distributed Se columns, is detected as a result of the CuPt-type ordering.

The same 'CuPt-ordered' CIS phase was also observed as a precipitate connected to a long PD within the chalcopyrite CIS matrix [Figure 4.37 (a)]. The elemental maps [Figure 4.37 (b)–(d)] from the long PD show Cu enrichment in combination with In depletion along the length of the defect, which is similar to the SF-like complex defects. A slight Cu enrichment due to the close positioning of cation columns and an accompanying slight In depletion are also detected at the precipitate, although the effect appears highly smeared out. While this would imply a reduced elemental redistribution in this region, it is in fact due to the presence of an underlying chalcopyrite structure below the precipitate. The chalcopyrite structure can be revealed by acquiring a through focal series of images, acquired by varying the microscope defocus setting from +20 nm to −20 nm as shown in Figure 4.38. At −20 nm defocus the chalcopyrite structure with two TBs and an ISF can be clearly seen.

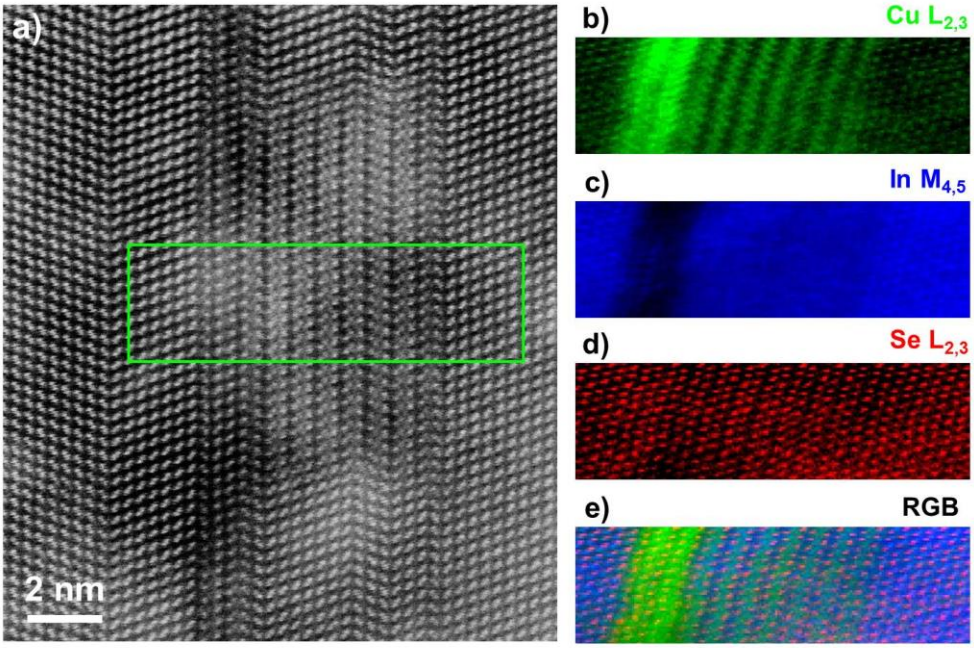

Figure 4.37 (a) HAADF image of a long PD and a small 'CuPt-ordered' precipitate formed in the CIS grain. Elemental distribution maps of (b) Cu-$L_{2,3}$, (c) In-$M_{4,5}$ and (d) Se-$L_{2,3}$ are extracted from the acquired EEL spectrum image. (e) RGB image composed of Cu, In and Se elemental distribution maps.

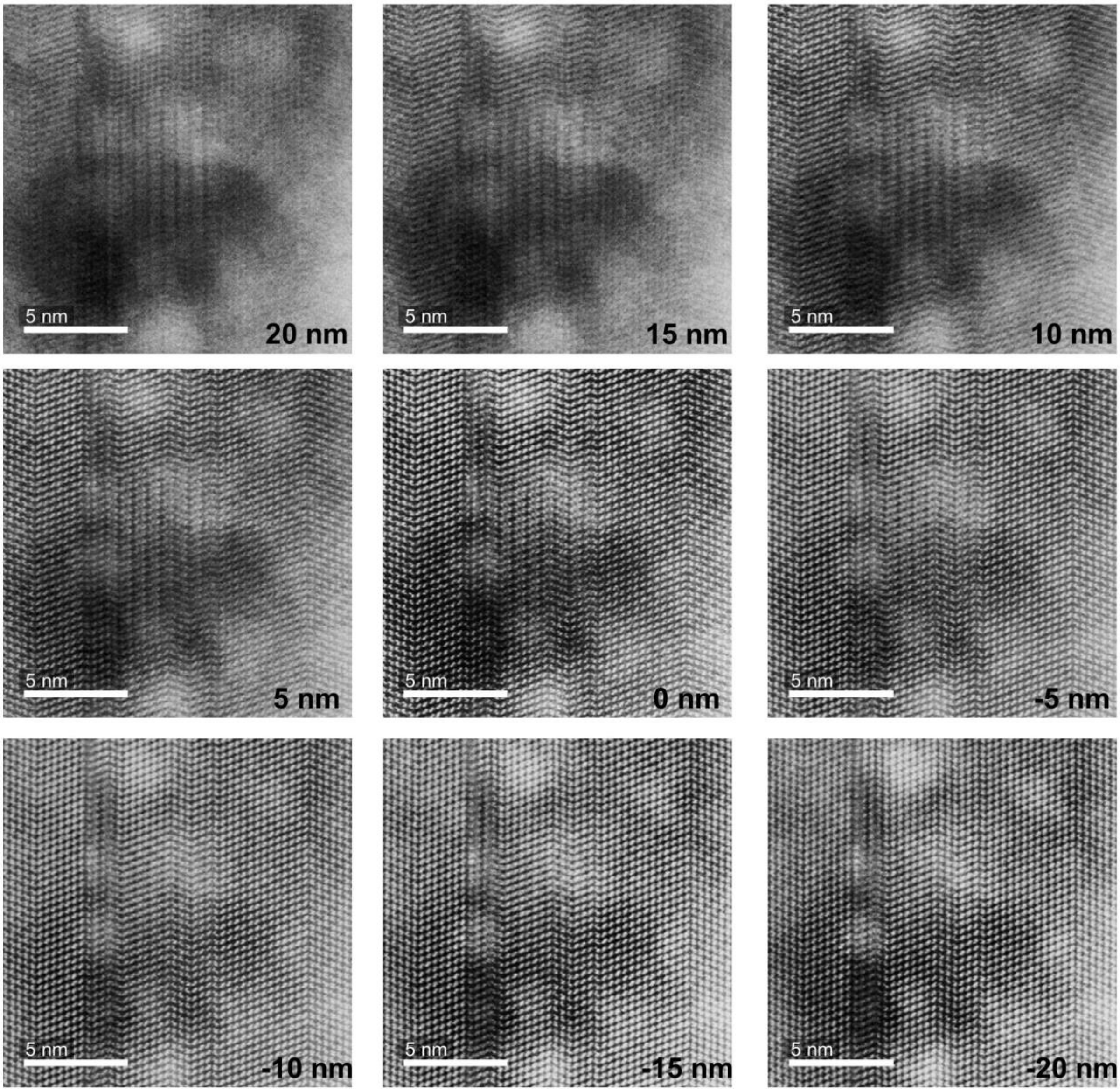

Figure 4.38 A through focal series from +20 nm to −20 nm of images from the same area shows that the ‘CuPt-ordered’ CIS phase is on top of the chalcopyrite CIS.

4.3.4. Defects in the growth-finished sample

The detection of secondary phases in the CI(G)S system by XRD and TEM in combination with EDXS initiated research on the growth mechanisms of CI(G)S thin-films. In 1993, Klenk *et al*. proposed a vapor-liquid-solid mechanism as a growth model for large-grained CIS and CGS films under Cu-rich conditions.[137] In 1997, Wada *et al*. proposed a new growth model called ‘topotactic reaction’ for CIS.[89] A topotactic reaction is a chemical solid-state reaction, where the initial and final crystals have a three-dimensional crystallographic relation.[138] In a later work, Nishiwaki *et al*. explained the growth of CIGS produced by the three-stage co-evaporation technique with the same model.[139] According to their proposed model, during the third stage of this process two reactions occur: *i)* the growth of CIGS grains from the $Cu_{2-x}Se$ phase through the incorporation of In, Ga and in the presence of sufficiently-high Se vapor pressure. The $Cu_{2-x}Se$ phase is thought to transform to CIGS by maintaining the Se sublattice in the same cubic closed-packed structure, while the cations are being exchanged. The crystallographic relation between the pseudo-cubic CIS and the cubic $Cu_{2-x}Se$ is given by Wada *et al.* as follows: $(11\bar{1})_{Cu2Se} \| (11\bar{1})_{CIS}$ and $[011]_{Cu2Se} \| [011]_{CIS}$ [89]; *ii)* the decomposition of CIGS and the formation of indium selenide and gallium selenide. However, this second (clearly unwanted) reaction can be impeded by sufficient Se flux or even be reversed without any decomposition of the forming CIGS.[139]

- **The $Cu_{2-x}Se$ phase**

Figure 4.39 shows two grains, where the upper grain is oriented in the <110>-direction and the bottom grain is oriented in an unknown direction. A higher magnification image from the same region is shown in Figure 4.40 (a).

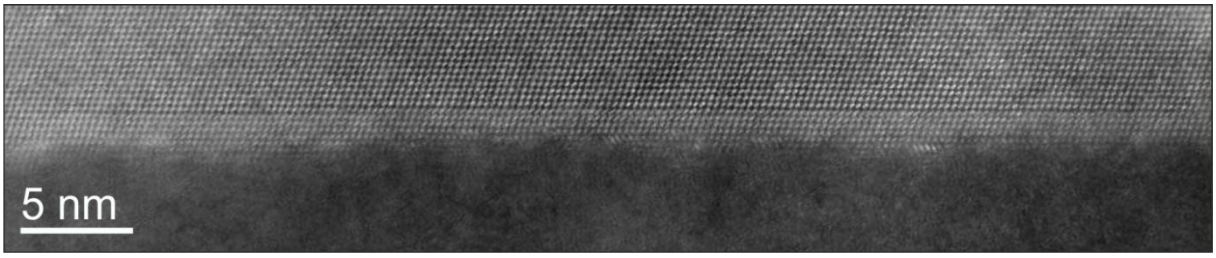

Figure 4.39 HAADF image of a platelet around the grain boundary. Reprinted from E. Simsek Sanli *et al.*, Appl. Phys. Lett. 111, 032103 (2017)[85], with the permission of AIP Publishing.

The two grains are separated by about 5 atomic planes of material which can be described as a platelet coherently grown on the upper grain. The platelet exhibits a clearly different crystal structure from the upper grain. In the <110>-projection of the CIGS structure, Se and cation columns form the characteristic dumbbell structure, whereas the platelet exhibits triplets of closely spaced Cu-Se-Cu atomic columns instead. Cu, In and Se elemental maps [Figure 4.40 (b)–(d)] show the chemical differences between the CIGS matrix and the platelet present at the GB: the platelet is richer in Cu than the main grain, while the concentration of In is strongly depleted. The platelet is therefore identified as $Cu_{2-x}Se$. Figure 4.40 (e) is a composite image showing the distribution of Se, Cu and In. The planar distances for the Se columns are equal for both the CIGS matrix and the $Cu_{2-x}Se$ phase. The $Cu_{2-x}Se$ phase seems highly ordered, although the EELS map suggests a somewhat smeared Cu distribution. This can be attributed to the close positioning of Cu columns in the <110>-direction. The slightly lowered Se signal intensity around the GB region gives further credence to the identification of a secondary phase different from the bulk, going from a high Se concentration CIGS matrix to the lower Se concentration $Cu_{2-x}Se$ phase. The occurrence of cation redistribution at random GBs was unambiguously demonstrated, including clear evidence for regions with Cu enrichment and In depletion. However, contrary to what is observed here, those Cu-rich/In-poor boundary regions did not exhibit any clear crystallinity, and no highly ordered secondary phase was observed at those boundaries. The presence of a remnant $Cu_{2-x}Se$ fully ordered phase at GBs and within grains appears therefore to be a rare occurrence.

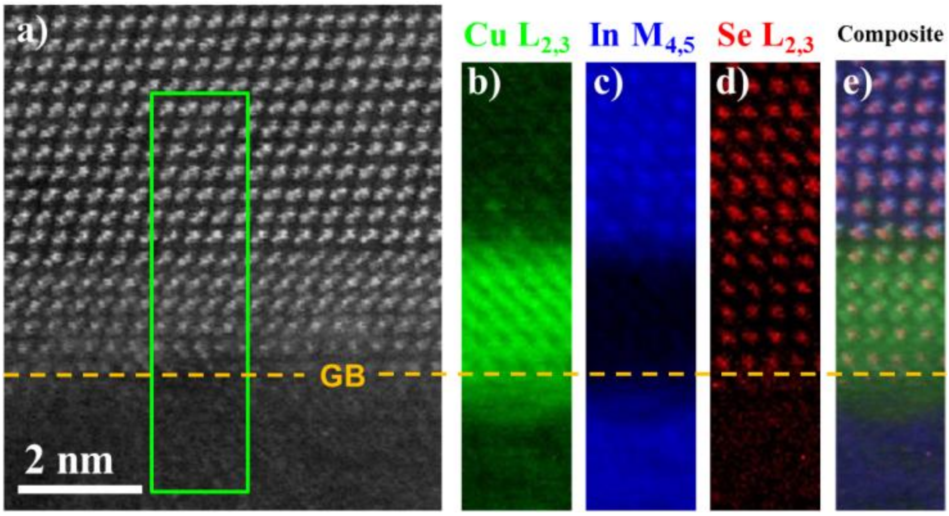

Figure 4.40 (a) $Cu_{2-x}Se$ phase around a grain boundary on {112} planes. Cu enrichment in combination with In depletion is visible at the GB region. Elemental distribution maps of (b) Cu-$L_{2,3}$, (c) In-$M_{4,5}$ and (d) Se-$L_{2,3}$ are extracted from the acquired EEL spectrum image. (e) Simultaneous HAADF image and an RGB image are superimposed. The CIGS dumbbell structure and the $Cu_{2-x}Se$ triplets are clearly visible. Reprinted from E. Simsek Sanli *et al.*, Appl. Phys. Lett. 111, 032103 (2017)[85], with the permission of AIP Publishing.

The same coherent structure identified as $Cu_{2-x}Se$ platelets was also observed within a CIGS grain, similarly aligned along the {112} planes. Figure 4.41 (a) shows an example of a platelet inclusion consisting of three atomic planes of $Cu_{2-x}Se$ within the CIGS matrix. A similar example with two planes of $Cu_{2-x}Se$ phase is shown in the Figure 4.42 (a). Figure 4.42 (b)-(d) show Cu, In and Se elemental maps, respectively. The composite image [Figure 4.42 (e)] shows a polarity inversion of the Se and cation columns in the CIGS matrix across the $Cu_{2-x}Se$ platelet. The red Se atomic columns are on the down-side of the dumbbells in the upper part of the matrix, but on the top-side of the dumbbells in the bottom side of the CIGS matrix. The reason for this site reversal is the presence of additional Cu columns in the $Cu_{2-x}Se$ phase. Site reversal was also the case at the GB, the Se map shows the uninterrupted continuation of the Se sub-lattice, whereas Cu and In cations are exchanged.

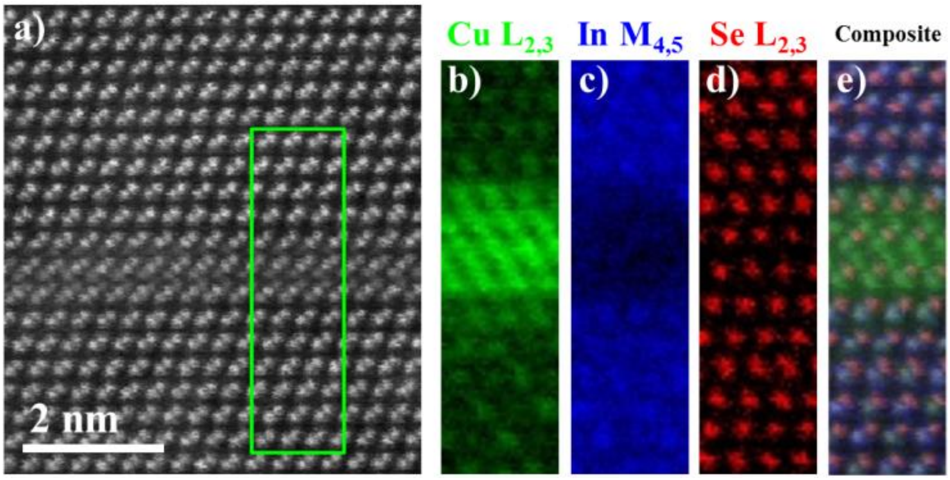

Figure 4.41 (a) Three planes of $Cu_{2-x}Se$ phase in a CIGS grain. Elemental distribution maps of (b)–(d) Cu, In, Se; (e) Simultaneous HAADF image is superimposed to an RGB image. Reprinted from E. Simsek Sanli *et al.*, Appl. Phys. Lett. 111, 032103 (2017)[85], with the permission of AIP Publishing.

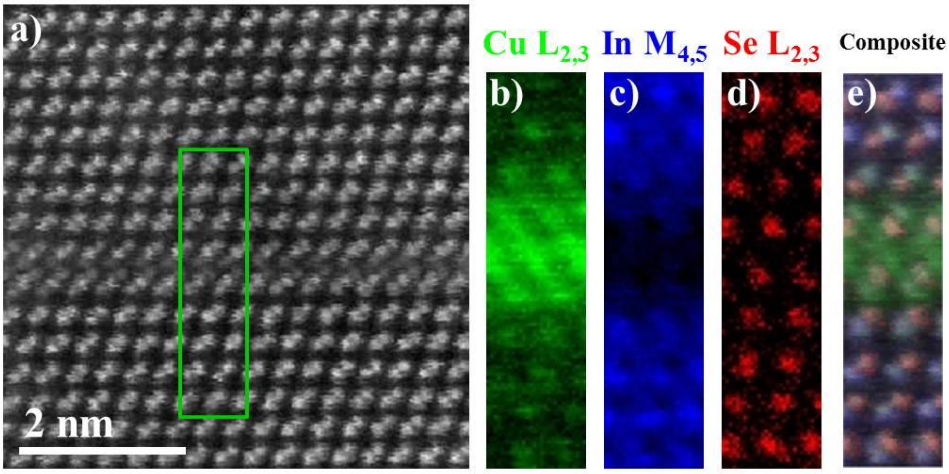

Figure 4.42 (a) Two planes of $Cu_{2-x}Se$ phase in the CIGS grain. There is a site change in CIGS lattice across the $Cu_{2-x}Se$ phase. Elemental distribution maps of (b)–(d) Cu, In and Se; (e) Composite image shows elemental distribution. Reprinted from E. Simsek Sanli *et al.*, Appl. Phys. Lett. 111, 032103 (2017)[85], with the permission of AIP Publishing.

Despite its simple binary chemical formula, Cu-Se forms complex stoichiometric (CuSe, Cu_2Se, $CuSe_2$, Cu_3Se_2) and non-stoichiometric, $Cu_{2-x}Se$ phases.[140, 141] There are two main equilibrium phases for non-stoichiometric $Cu_{2-x}Se$ at lower Cu concentrations: a high-temperature β-$Cu_{2-x}Se$ and a low-temperature α-$Cu_{2-x}Se$ phase.[142] It has also been noted that for $x = 0.15$–0.25 the high-temperature phase can be present at room temperature.[143] While the EELS results unequivocally show the presence of a secondary $Cu_{2-x}Se$ phase, a comparison of the structure observed experimentally with simulations can help to confirm the specific crystallography of the inclusion phase. Thus, in order to validate the experimental observations, a model structure was created, informed by the experimental images of the platelets incorporated within a CIS matrix (once again no Ga ions were included in the model structure for simplicity due to the low Ga content in the region of the film observed experimentally). A chalcopyrite-type crystal structure was used for the CIS. An anti-fluorite type structure with the space group $Fm\bar{3}m$ was used for the $Cu_{2-x}Se$ platelets, as the most likely structure, following Wada *et al.*[89] In the parent stoichiometric Cu_2Se structure (used in the model for simplicity, as an unambiguous determination of the exact platelet stoichiometry through EELS would be difficult), 4 Se atoms form a simple fcc sublattice, 4a (000), with 8 Cu atoms occupying the tetrahedral and octahedral sites, 8c ($^1/_4\,^1/_4\,^1/_4$), in the subcell.[140] The lattice parameters are adapted to match with the surrounding CIS to a = 5.8 Å and c = 11.6 Å, and for Cu_2Se to a = 5.8 Å. Figure 4.43 (a) and (b) show a <110> projection of the created CIS and Cu_2Se crystal structures visualized using Vesta.[144] The incorporation of a Cu_2Se platelet within a CIS matrix [Figure 4.43 (c)] with 23 nm thickness was carried out using Model Builder, a complex interface building tool provided in the QSTEM software suite, which is a free image simulation software based on frozen phonon multislice methods.[145] The simulation parameters were chosen to reflect the experimental conditions: 100 kV acceleration voltage with a semi-convergence angle of 33 mrad, and the HAADF detector's semi-angles were set to 85–190 mrad. Figure 4.43 (d) shows a simulated image for a total sample thickness of 16.1 nm, chosen to match with the measured thickness of the FIB lamella (~15 nm). The simulation is shown in the yellow frame overlaid on top of an experimental image, obtained by rigid registration of a series of rapidly scanned HAADF images.[146] The intensities in the simulated image and experimental image show an excellent match. It should be noted that the comparison is not provided on an absolute intensity scale. The intensities of both simulated and experimental images were stretched to the full greyscale range. Although the simulation is therefore not fully quantitative, it certainly demonstrates a good structural agreement with the proposed anti-fluorite phase.

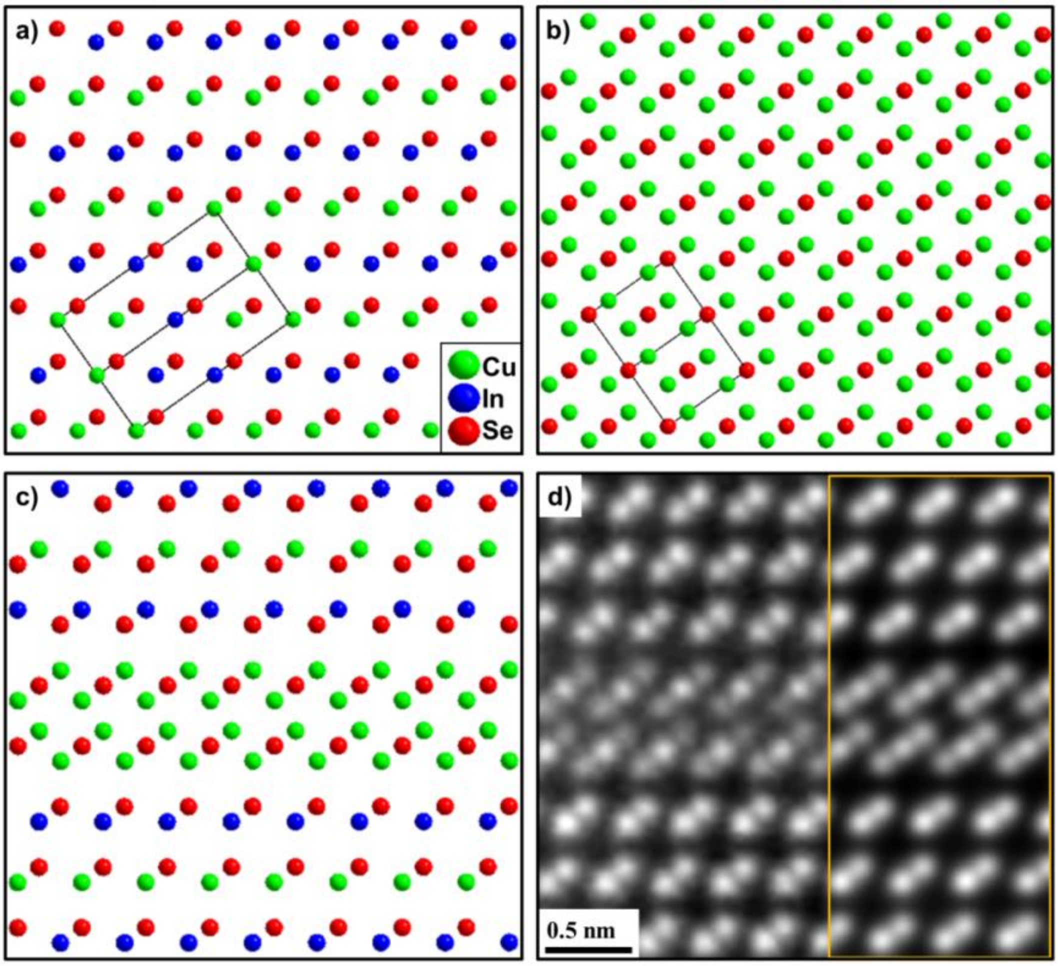

Figure 4.43 <110>-projection of the created (a) CIS –with a chalcopyrite crystal structure– and (b) Cu_2Se –with an antifluorite crystal structure– based on Wada *et al*. The unit cells are shown with black frames on the crystal structures. (c) Simulated model of Cu_2Se in the CIS matrix. (d) Averaged sequential image (left) overlapped with the simulated model of Cu_2Se (right) in the CIS matrix. Reprinted from E. Simsek Sanli *et al.*, Appl. Phys. Lett. 111, 032103 (2017)[85], with the permission of AIP Publishing.

Other possible crystal structures were also considered. Aside from the anti-fluorite structure used above, the other most likely Cu-Se containing secondary phases are $F\bar{4}3m$ and $F23$ for $Cu_{2-x}Se$ and $Pnmm$ for $CuSe_2$. Models of these structures are shown in the Figure 4.44 for completeness. However, a cursory visual inspection of these models demonstrates a poor match to the observed HAADF images, and full simulations were therefore not attempted.

The observation of $Cu_{2-x}Se$ platelets, which are likely the remnants of the $Cu_{2-x}Se$ phase known to form during the Cu-rich phase of the growth, in particular as small inclusions within grains, provide the most direct and conclusive experimental evidence to date of the proposed topotactical growth model for the formation of CIGS absorbers produced by three-stage co-evaporation technique.

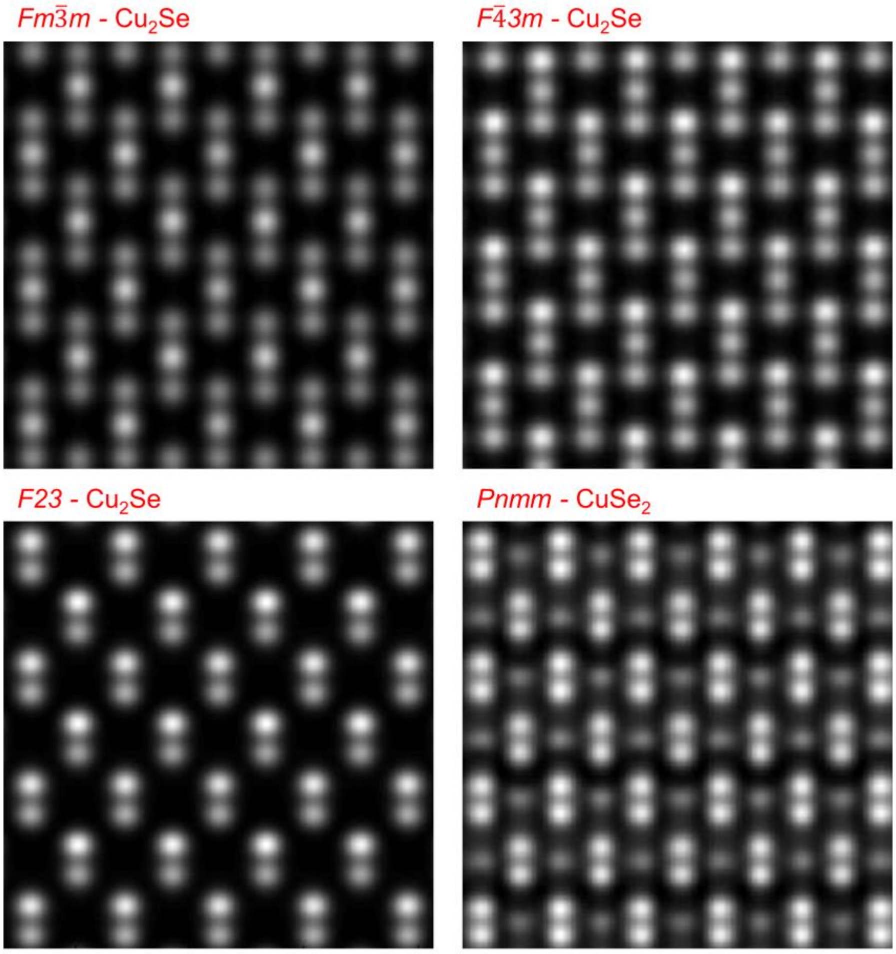

Figure 4.44 The simulated anti-fluorite type cubic structure for Cu_2Se phase and three other crystal structures for Cu_2Se and $CuSe_2$ phases. Reprinted from E. Simsek Sanli *et al.*, Appl. Phys. Lett. 111, 032103 (2017)[85], with the permission of AIP Publishing.

This page intentionally left blank.

5. Conclusion and outlook

In the present study, several TEM techniques were used to provide insights into the microstructural and compositional evolution of CIGS absorbers during various growth processes, with a particular focus on line and planar defects. STEM-LAADF imaging was applied for large-scale morphology and defect density analysis. The orientation of the grains was determined via electron diffraction. For the high-resolution analysis of the microstructural defects, STEM-HAADF imaging was used. Elemental distributions along the absorber layer and at the various structural defects were analyzed by EDXS and EELS. Furthermore, cation diffusion between different phases was investigated by heating experiments.

The recrystallization of CIS absorbers was investigated for the first time via STEM heating of CIS-$Cu_{2-x}Se$ diffusion couples. STEM-LAADF imaging provided a direct *in-situ* view of the GB migration in CIS during Cu in-diffusion. The GBs migrate towards the grains with closely-spaced PDs, and the PDs ultimately vanished. During the heating of diffusion couples, recrystallization started at the CIS/$Cu_{2-x}Se$ interface and advanced towards the back contact as Cu diffuses into the Cu-poor CIS layer. When the Cu-poor CIS was heated in the absence of the capping layer, no recrystallization was observed. Both results proved conclusively that recrystallization is triggered only by the excess Cu.

The contrast change in LAADF imaging during *in-situ* heating hinted towards a Cu-In interdiffusion. This was later confirmed by EDXS, performed after the heating experiments. Further experiments could include *in-situ* spectrum image acquisition, which would provide a near-instantaneous tracking of the Cu diffusion and enable the detection of the diffusion paths, (*i.e.* confirming that the diffusion does happen at GBs, as concluded from static studies so far). A particular challenge for such studies is the necessity of using different settings for imaging and spectroscopy. For example for LAADF imaging, low collection angles are needed, whereas for EELS, the collection angle needs to be large enough to achieve a decent signal-to-noise ratio. Also, for EDXS, the sample needs to be tilted towards the EDX detector, which increases the relative thickness of the sample in the direction of the electron beam. An increased electron path is of course not desired for both EELS and imaging. Moreover, the heating should be sufficiently slow to allow the spectrum imaging to be acquired in a steady sample. In this case, either the sample should be heated with a rate of about 1 K/min, or in intervals of about 5-10 min. In the case of slow temperature ramping, the analysis can take up to 7 h. In the case of heating with intervals, the recrystallization is expected to stop when the heating stops. However, the temperature fluctuates a few degrees until it reaches a steady value, which may slightly alter the microstructure and the elemental distribution during spectrum imaging.

The comparison of growth-interrupted and growth-finished samples validated the presence of closely-spaced PDs before the recrystallization and their annihilation during the growth process. However, in the growth-finished samples individual microstructural defects different than closely-spaced PDs were detected.

The in-depth HR-STEM and EELS analyses from various growth stages provided clues regarding the microstructural evolution of individual defects. SF-like complex defects were detected in Cu-poor growth-interrupted samples. These complex defects might be the origin of the $Cu_{2-x}Se$ phase that forms after the absorber becomes Cu-rich. A future high-resolution heating study on diffusion couples could reveal the exact evolution of SF-like complex defects. Furthermore, the proposed topotactical growth model was experimentally confirmed by the observation of coherent $Cu_{2-x}Se$ platelets in the growth-finished CIGS absorber.

A pair of Frank partial dislocations, which was detected (for the first time in the CIGS system) in a growth-interrupted sample, was studied by STEM-EELS and calculations based on DFT. Outside of the dislocations cores, Cu-rich clouds are formed due to strain. The energy of the dislocation cores is reduced in the presence of asymmetric Cu excess. The DFT simulations show that at the cation-containing α-core, the neutral Cu_{In} antisites have negative formation energies, whereas at the Se-containing β-core, the Cu_{In} antisites and Cu interstitials have low positive formation energies. The presence of Cu_{In} point defects induces defect states and enhances non-radiative recombination. Thus, the complete annihilation of Frank partials is essential for achieving high power-conversion efficiencies. This study confirmed that the growth conditions used for this set of samples is effective at achieving this: no Frank partials were observed in the growth-finished samples, which indeed are known to reach good efficiencies.

Although closely-spaced PDs were annihilated, individual cation-Se terminated TBs and SFs preserved their structure and composition during the entire growth. As previously studied via theoretical calculations, the presence of such defects with stoichiometric composition does not alter the optoelectronic properties of the absorber. Hence, the presence of such defects is not detrimental to the final performance of the CIGS solar cells. The number of edge dislocations and random GBs is reduced after the recrystallization, but both defect types were present at various growth stages as well. To comment on the effects of edge dislocations, and in particular of the strong elemental redistribution observed experimentally here, further theoretical work is needed. For the GBs; however, the formation of Cu_{In} and O_{Se} antisites were previously found to be beneficial for removal of the gap states. This explains why CIGS solar cells show one of the highest efficiencies, despite their polycrystalline nature.

Finally, in a future study, local band gap fluctuations at microstructural defects can be analyzed via valence EELS. However, due to the low band-gap energy of CIGS, ~1.2 eV, high energy resolution is needed. A microscope with both an aberration corrector and a monochromator is essential to reach the required spatial and energy resolutions for the atomically resolved local band gap measurements at structural defects. Moreover, low acceleration voltage is required to prevent the occurrence of Cherenkov radiation, which can limit the determination of the band gap.

This page intentionally left blank.

List of figures

Abbreviations and symbols

ADF	Annular dark field
BF	Bright field
CBM	Conduction-band minimum
CGS	$CuGaSe_2$
CIGS	$Cu(In,Ga)Se_2$
CI(G)S	$Cu(In,Ga)Se_2$ and/or $CuInSe_2$
CIS	$CuInSe_2$
DM	Digital Micrograph
EDXRD	Energy-dispersive X-ray diffraction
EDXS	Energy-dispersive X-ray spectroscopy
EELS	Electron energy-loss spectroscopy
ESF	Extrinsic stacking fault
FIB	Focused-ion beam
GB	Grain boundary
GPA	Geometric Phase Analysis
HAADF	High-angle annular dark-field
HR-STEM	High-resolution scanning transmission electron microscopy
ISF	Intrinsic stacking fault
J_{sc}	Short-circuit current density
LAADF	Low-angle annular dark-field
PD	Planar defect
RGB	Red-green-blue
SF	Stacking fault
SI	Spectrum image
SLG	Soda-lime glass
STEM	Scanning transmission electron microscopy
TB	Twin boundary
TEM	Transmission electron microscopy
V_{oc}	Open-circuit voltage
VBM	Valance-band maximum

This page intentionally left blank.

References

1. A. E. Becquerel, Comptes Rendus des Séances Hebdomadaires **9**, 561-567 (1839).
2. W. Smith, Nature **7**, 303 (1873).
3. W. G. Adams and R. E. Day, Philosophical Transactions of the Royal Society of London **167**, 313-349 (1877).
4. C. E. Fritts, presented at the Proceedings of the American Association for the Advancement of Science, 1883 (unpublished).
5. D. M. Chapin, C. S. Fuller and G. L. Pearson, Journal of Applied Physics **25** (5), 676-677 (1954).
6. A. Ã. Reinders, P. Verlinden, A. Freundlich and W. van Sark, *Photovoltaic Solar Energy: From Fundamentals to Applications*. (Wiley, 2017).
7. K. P. Bhandari, J. M. Collier, R. J. Ellingson and D. S. Apul, Renewable and Sustainable Energy Reviews **47**, 133-141 (2015).
8. M. A. Green, Y. Hishikawa, W. Warta, E. D. Dunlop, D. H. Levi, J. Hohl-Ebinger and A. W. H. Ho-Baillie, Progress in Photovoltaics: Research and Applications **25** (7), 668-676 (2017).
9. J. Ramanujam and U. P. Singh, Energy & Environmental Science **10** (6), 1306-1319 (2017).
10. S. Siebentritt, Current Opinion in Green and Sustainable Chemistry **4**, 1-7 (2017).
11. T. D. Lee and A. U. Ebong, Renewable and Sustainable Energy Reviews **70**, 1286-1297 (2017).
12. A. M. K. Gustafsson, Recycling of CIGS solar cell waste materials. PhD Thesis, Chalmers University of Technology (2014).
13. M. I. Asghar, J. Zhang, H. Wang and P. D. Lund, Renewable and Sustainable Energy Reviews **77** (Supplement C), 131-146 (2017).
14. M. A. Green and A. Ho-Baillie, ACS Energy Letters **2** (4), 822-830 (2017).
15. J.-P. Correa-Baena, A. Abate, M. Saliba, W. Tress, T. Jesper Jacobsson, M. Gratzel and A. Hagfeldt, Energy & Environmental Science **10** (3), 710-727 (2017).
16. M. A. Green, Y. Hishikawa, E. D. Dunlop, D. H. Levi, J. Hohl-Ebinger and A. W. Y. Ho-Baillie, Progress in Photovoltaics: Research and Applications **26** (1), 3-12 (2018).
17. Solar Frontier press release dated December 20, 2017.
18. L. L. Kazmerski, M. Hallerdt, P. J. Ireland, R. A. Mickelsen and W. S. Chen, Journal of Vacuum Science & Technology A: Vacuum, Surfaces, and Films **1** (2), 395-398 (1983).
19. A. Rockett, *The Materials Science of Semiconductors*. (Springer US, 2007).
20. C. Bellabarba and C. Rincon, Japanese Journal of Applied Physics **32** (S3), 599 (1993).
21. W. Hörig, W. Möller, H. Neumann, E. Reccius and G. Kühn, physica status solidi (b) **92** (1), K1-K4 (1979).
22. S.-H. Wei, S. B. Zhang and A. Zunger, Applied Physics Letters **72** (24), 3199-3201 (1998).
23. A. Chirilă, S. Buecheler, F. Pianezzi, P. Bloesch, C. Gretener, A. R. Uhl, C. Fella, L. Kranz, J. Perrenoud, S. Seyrling, R. Verma, S. Nishiwaki, Y. E. Romanyuk, G. Bilger and A. N. Tiwari, Nat Mater **10** (11), 857-861 (2011).
24. D. Abou-Ras, R. Caballero, C. A. Kaufmann, M. Nichterwitz, K. Sakurai, S. Schorr, T. Unold and H. W. Schock, physica status solidi (RRL) – Rapid Research Letters **2** (3), 135-137 (2008).
25. Y. Hamakawa, *Thin-Film Solar Cells: Next Generation Photovoltaics and Its Applications*. (Springer Berlin Heidelberg, 2003).
26. P. Jackson, R. Wuerz, D. Hariskos, E. Lotter, W. Witte and M. Powalla, Physica Status Solidi (RRL) – Rapid Research Letters **10** (8), 583-586 (2016).
27. A. M. Gabor, J. R. Tuttle, D. S. Albin, M. A. Contreras, R. Noufi and A. M. Hermann, Applied Physics Letters **65** (2), 198 (1994).
28. T. Schlenker, M. L. Valero, H. W. Schock and J. H. Werner, Journal of Crystal Growth **264** (1–3), 178-183 (2004).
29. R. Caballero, V. Izquierdo-Roca, X. Fontané, C. A. Kaufmann, J. Álvarez-García, A. Eicke, L. Calvo-Barrio, A. Pérez-Rodríguez, H. W. Schock and J. R. Morante, Acta Materialia **58** (9), 3468-3476 (2010).
30. J. K. Larsen, L. Gütay and S. Siebentritt, Applied Physics Letters **98** (20), 201910 (2011).
31. H. Rodriguez-Alvarez, N. Barreau, C. A. Kaufmann, A. Weber, M. Klaus, T. Painchaud, H. W. Schock and R. Mainz, Acta Materialia **61** (12), 4347-4353 (2013).

32. R. Caballero, C. A. Kaufmann, V. Efimova, T. Rissom, V. Hoffmann and H. W. Schock, Progress in Photovoltaics: Research and Applications **21** (1), 30-46 (2013).
33. R. Mainz, E. Simsek Sanli, H. Stange, D. Azulay, S. Brunken, D. Greiner, S. Hajaj, M. D. Heinemann, C. A. Kaufmann, M. Klaus, Q. M. Ramasse, H. Rodriguez-Alvarez, A. Weber, I. Balberg, O. Millo, P. A. van Aken and D. Abou-Ras, Energy & Environmental Science **9** (5), 1818-1827 (2016).
34. R. Klenk, T. Walter, D. Schmid and H. W. Schock, Japanese Journal of Applied Physics **32** (S3), 57 (1993).
35. L. Gütay, D. Regesch, J. K. Larsen, Y. Aida, V. Depredurand and S. Siebentritt, Applied Physics Letters **99** (15), 151912 (2011).
36. J. R. Tuttle, D. S. Albin and R. Noufi, Solar Cells **27** (1), 231-236 (1989).
37. V. Nadenau, D. Hariskos, H.-W. Schock, M. Krejci, F.-J. Haug, A. N. Tiwari, H. Zogg and G. Kostorz, Journal of Applied Physics **85** (1), 534-542 (1999).
38. Y. Yan, K. M. Jones, J. AbuShama, M. M. Al-Jassim and R. Noufi, MRS Online Proceedings Library **668**, H6.10.11-H16.10.16 (2001).
39. T. B. Elliot, *New Research on Semiconductors*. (Nova Science Publishers, 2006).
40. J. S. Park, Z. Dong, S. Kim and J. H. Perepezko, Journal of Applied Physics **87** (8), 3683-3690 (2000).
41. S.-H. Wei, S. B. Zhang and A. Zunger, Journal of Applied Physics **85** (10), 7214-7218 (1999).
42. J. Hedstrom, H. Ohlsen, M. Bodegard, A. Kylner, L. Stolt, D. Hariskos, M. Ruckh and H.-W. Schock, Record of the Twenty Third IEEE Photovoltaic Specialists Conference, 364-371 (1993).
43. J. R. V. Probst, W. Stetter, H. Harms, W. Riedl, J. Holz, and F. Karg, Proceedings of the 13th European Photovoltaic Solar Energy Conference, 2123 (1995).
44. D. W. Niles, K. Ramanathan, F. Hasoon, R. Noufi, B. J. Tielsch and J. E. Fulghum, Journal of Vacuum Science & Technology A: Vacuum, Surfaces, and Films **15** (6), 3044-3049 (1997).
45. M. A. Contreras, B. Egaas, P. Dippo, J. Webb, J. Granata, K. Ramanathan, S. Asher, A. Swartzlander and R. Noufi, presented at the Conference Record of the Twenty Sixth IEEE Photovoltaic Specialists Conference - 1997, 1997 (unpublished).
46. L. Kronik, U. Rau, J.-F. Guillemoles, D. Braunger, H.-W. Schock and D. Cahen, Thin Solid Films **361-362**, 353-359 (2000).
47. J. E. Granata, J. R. Sites, S. Asher and R. J. Matson, *Quantitative incorporation of sodium in CuInSe2 and Cu(In,Ga)Se2 photovoltaic devices*. (1997).
48. K. Granath, M. Bodegård and L. Stolt, Solar Energy Materials and Solar Cells **60** (3), 279-293 (2000).
49. D. Rudmann, A. F. da Cunha, M. Kaelin, F. Kurdesau, H. Zogg, A. N. Tiwari and G. Bilger, Applied Physics Letters **84** (7), 1129-1131 (2004).
50. N. Tokio, I. Daisuke, O. Hiroki and K. Akio, Japanese Journal of Applied Physics **36** (2R), 732 (1997).
51. J. H. Yun, K. H. Kim, M. S. Kim, B. T. Ahn, S. J. Ahn, J. C. Lee and K. H. Yoon, Thin Solid Films **515** (15), 5876-5879 (2007).
52. T. Lepetit, S. Harel, L. Arzel, G. Ouvrard and N. Barreau, Progress in Photovoltaics: Research and Applications **25** (12), 1068-1076 (2017).
53. N. Nicoara, T. Lepetit, L. Arzel, S. Harel, N. Barreau and S. Sadewasser, Scientific Reports **7**, 41361 (2017).
54. M. Malitckaya, H. P. Komsa, V. Havu and M. J. Puska, The Journal of Physical Chemistry C **121** (29), 15516-15528 (2017).
55. M. Tsuyoshi, K. Atsuhito and W. Takahiro, Japanese Journal of Applied Physics **54** (8S1), 08KC20 (2015).
56. P. Schöppe, S. Schönherr, R. Wuerz, W. Wisniewski, G. Martínez-Criado, M. Ritzer, K. Ritter, C. Ronning and C. S. Schnohr, Nano Energy **42** (Supplement C), 307-313 (2017).
57. S. Schorr, C. Stephan and C. A. Kaufmann, in *Neutron Applications in Materials for Energy*, edited by G. J. Kearley and V. K. Peterson (Springer International Publishing, Cham, 2015), pp. 83-107.

58. C. J. Kiely, R. C. Pond, G. Kenshole and A. Rockett, Philosophical Magazine A **63** (6), 1249-1273 (1991).
59. L. K. Ondrej, C. L. Tracy, F. M. Matthew, S. Gwyn, E. B. Philip and D. Niklas, Journal of Physics: Conference Series **522** (1), 012023 (2014).
60. D. B. Williams and C. B. Carter, *Transmission Electron Microscopy: A Textbook for Materials Science*. (Springer, 1996).
61. U. Kaiser, J. Biskupek, J. C. Meyer, J. Leschner, L. Lechner, H. Rose, M. Stöger-Pollach, A. N. Khlobystov, P. Hartel, H. Müller, M. Haider, S. Eyhusen and G. Benner, Ultramicroscopy **111** (8), 1239-1246 (2011).
62. O. Scherzer, Zeitschrift für Physik **101** (9), 593-603 (1936).
63. O. Scherzer, Optik **8**, 311-317 (1947).
64. M. Haider, S. Uhlemann, E. Schwan, H. Rose, B. Kabius and K. Urban, Nature **392**, 768 (1998).
65. J. Zach and M. Haider, Nuclear Instruments and Methods in Physics Research Section A: Accelerators, Spectrometers, Detectors and Associated Equipment **363** (1), 316-325 (1995).
66. O. L. Krivanek, N. Dellby, A. J. Spence, R. A. Camps and L. M. Brown, *Aberration correction in the STEM*. (1997).
67. I. MacLaren and Q. M. Ramasse, International Materials Reviews **59** (3), 115-131 (2014).
68. R. Brydson, *Aberration-corrected Analytical Electron Microscopy*. (Wiley, 2011).
69. L. M. Brown, Journal of Physics: Conference Series **522** (1), 012012 (2014).
70. P. J. Phillips, M. De Graef, L. Kovarik, A. Agrawal, W. Windl and M. J. Mills, Ultramicroscopy **116**, 47-55 (2012).
71. D. C. Bell and N. Erdman, *Low Voltage Electron Microscopy: Principles and Applications*. (Wiley, 2012).
72. R. F. Egerton, Microscopy and Microanalysis **20** (3), 658-663 (2014).
73. R. F. Egerton, *Electron Energy-Loss Spectroscopy in the Electron Microscope*. (Springer US, 2011).
74. R. F. Egerton and M. Malac, Journal of Electron Spectroscopy and Related Phenomena **143** (2), 43-50 (2005).
75. Watanabe M., Okunishi E. and Ishizuka K., Microscopy and Analysis **23** (7), 5-7 (2009).
76. A. Kirkland, J. Hutchison, R. S. o. Chemistry and D. J. Smith, *Nanocharacterisation*. (RSC Publishing, 2007).
77. L. A. Giannuzzi and F. A. Stevie, *Introduction to Focused Ion Beams: Instrumentation, Theory, Techniques and Practice*. (Springer, 2005).
78. L. A. Giannuzzi, J. L. Drown, S. R. Brown, R. B. Irwin and F. A. Stevie, Microscopy Research and Technique **41** (4), 285-290 (1998).
79. J. Ayache, L. Beaunier, J. Boumendil, G. Ehret and D. Laub, *Sample Preparation Handbook for Transmission Electron Microscopy: Methodology*. (Springer New York, 2010).
80. D. Abou-Ras, B. Marsen, T. Rissom, F. Frost, H. Schulz, F. Bauer, V. Efimova, V. Hoffmann and A. Eicke, Micron **43** (2–3), 470-474 (2012).
81. M. J. Hÿtch, E. Snoeck and R. Kilaas, Ultramicroscopy **74** (3), 131-146 (1998).
82. L. Jones and P. D. Nellist, Microscopy and Microanalysis **19** (4), 1050-1060 (2013).
83. E. Simsek Sanli, Q. M. Ramasse, W. Sigle, D. Abou-Ras, R. Mainz, A. Weber, H.-J. Kleebe and P. A. van Aken, Journal of Applied Physics **120** (20), 205301 (2016).
84. E. Simsek Sanli, D. Barragan-Yani, Q. M. Ramasse, K. Albe, R. Mainz, D. Abou-Ras, A. Weber, H. J. Kleebe and P. A. van Aken, Physical Review B **95** (19), 195209 (2017).
85. E. Simsek Sanli, Q. M. Ramasse, R. Mainz, A. Weber, D. Abou-Ras, W. Sigle and P. A. van Aken, Applied Physics Letters **111** (3), 032103 (2017).
86. N. Barreau, T. Painchaud, F. Couzinié-Devy, L. Arzel and J. Kessler, Acta Materialia **58** (17), 5572-5577 (2010).
87. S. Nishiwaki, T. Satoh, S. Hayashi, Y. Hashimoto, T. Negami and T. Wada, Journal of Materials Research **14** (12), 4514-4520 (1999).
88. J. Kessler, C. Chityuttakan, J. Lu, J. Schöldström and L. Stolt, Progress in Photovoltaics: Research and Applications **11** (5), 319-331 (2003).
89. T. Wada, N. Kohara, T. Negami and M. Nishitani, Journal of Materials Research **12** (6), 1456-1462 (1997).

90. D. Thomas, R. Mainz, H. Rodriguez-Alvarez, B. Marsen, D. Abou-Ras, M. Klaus, C. Genzel and H. W. Schock, Thin Solid Films **519** (21), 7193-7196 (2011).
91. R. R. Keller and R. H. Geiss, Journal of Microscopy **245** (3), 245-251 (2012).
92. I. M. Kötschau and H. W. Schock, Journal of Physics and Chemistry of Solids **64** (9), 1559-1563 (2003).
93. R. Mainz, H. Rodriguez-Alvarez, M. Klaus, D. Thomas, J. Lauche, A. Weber, M. D. Heinemann, S. Brunken, D. Greiner, C. A. Kaufmann, T. Unold, H. W. Schock and C. Genzel, Physical Review B **92** (15), 155310 (2015).
94. H. Rodriguez-Alvarez, R. Mainz, B. Marsen and H.-W. Schock, Journal of Solid State Chemistry **183** (4), 803-806 (2010).
95. H. Rodriguez-Alvarez, A. Weber, J. Lauche, C. A. Kaufmann, T. Rissom, D. Greiner, M. Klaus, T. Unold, C. Genzel, H.-W. Schock and R. Mainz, Advanced Energy Materials **3** (10), 1381-1387 (2013).
96. T. Maeda, W. Gong and T. Wada, Japanese Journal of Applied Physics **55** (04ES15) (2016).
97. N. Kohara, S. Nishiawaki, T. Negami and T. Wada, Japanese Journal of Applied Physics **39** (11R), 6316 (2000).
98. M. Gloeckler and J. R. Sites, Journal of Physics and Chemistry of Solids **66** (11), 1891-1894 (2005).
99. C. A. Kaufmann, R. Caballero, T. Unold, R. Hesse, R. Klenk, S. Schorr, M. Nichterwitz and H. W. Schock, Solar Energy Materials and Solar Cells **93** (6-7), 859-863 (2009).
100. R. Caballero, C. A. Kaufmann, T. Eisenbarth, M. Cancela, R. Hesse, T. Unold, A. Eicke, R. Klenk and H. W. Schock, Thin Solid Films **517** (7), 2187-2190 (2009).
101. O. Lundberg, J. Lu, A. Rockett, M. Edoff and L. Stolt, Journal of Physics and Chemistry of Solids **64** (9–10), 1499-1504 (2003).
102. A. M. Gabor, J. R. Tuttle, M. H. Bode, A. Franz, A. L. Tennant, M. A. Contreras, R. Noufi, D. G. Jensen and A. M. Hermann, Solar Energy Materials and Solar Cells **41–42**, 247-260 (1996).
103. S. Schleussner, U. Zimmermann, T. Wätjen, K. Leifer and M. Edoff, Solar Energy Materials and Solar Cells **95** (2), 721-726 (2011).
104. N. E Gorji, M. D. Perez, U. Reggiani and L. Sandrolini, *A New Approach to Valence and Conduction Band Grading in CIGS Thin Film Solar Cells*. (2012).
105. T. Dullweber, G. H. anna, U. Rau and H. W. Schock, Solar Energy Materials and Solar Cells **67** (1), 145-150 (2001).
106. J. Dietrich, D. Abou-Ras, T. Rissom, T. Unold, H. Schock and C. Boit, Photovoltaics, IEEE Journal of **2** (3), 364-370 (2012).
107. D. Abou-Ras, S. S. Schmidt, N. Schäfer, J. Kavalakkatt, T. Rissom, T. Unold, R. Mainz, A. Weber, T. Kirchartz, E. Simsek Sanli, P. A. van Aken, Q. M. Ramasse, H.-J. Kleebe, D. Azulay, I. Balberg, O. Millo, O. Cojocaru-Mirédin, D. Barragan-Yani, K. Albe, J. Haarstrich and C. Ronning, physica status solidi (RRL) – Rapid Research Letters **10** (5), 363-375 (2016).
108. Y. Yan, R. Noufi and M. M. Al-Jassim, Physical Review Letters **96** (20) (2006).
109. Y. Yan, K. M. Jones, C. S. Jiang, X. Z. Wu, R. Noufi and M. M. Al-Jassim, Physica B: Condensed Matter **401-402**, 25-32 (2007).
110. D. B. Holt and B. G. Yacobi., *Extended Defects in Semiconductors*. (Cambridge University Press, 2007).
111. W. Bollmann, *Crystal defects and crystalline interfaces*. (Springer-Verlag, 1970).
112. N. Medvedeva, E. Shalaeva, M. Kuznetsov and M. Yakushev, Physical Review B **73** (3) (2006).
113. Y. Yan, C. S. Jiang, R. Noufi, S.-H. Wei, H. R. Moutinho and M. M. Al-Jassim, Physical Review Letters **99** (23) (2007).
114. C. Persson and A. Zunger, Applied Physics Letters **87** (21), 211904 (2005).
115. H. Mirhosseini, J. Kiss and C. Felser, Physical Review Applied **4** (6) (2015).
116. D. Abou-Ras, S. S. Schmidt, R. Caballero, T. Unold, H.-W. Schock, C. T. Koch, B. Schaffer, M. Schaffer, P.-P. Choi and O. Cojocaru-Mirédin, Advanced Energy Materials **2** (8), 992-998 (2012).
117. D. Abou-Ras, S. Schorr and H. W. Schock, Journal of Applied Crystallography **40** (5), 841-848 (2007).

118. R. Baier, C. Leendertz, D. Abou-Ras, M. C. Lux-Steiner and S. Sadewasser, Solar Energy Materials and Solar Cells **130**, 124-131 (2014).
119. S. Sadewasser, D. Abou-Ras, D. Azulay, R. Baier, I. Balberg, D. Cahen, S. Cohen, K. Gartsman, K. Ganesan, J. Kavalakkatt, W. Li, O. Millo, T. Rissom, Y. Rosenwaks, H. W. Schock, A. Schwarzman and T. Unold, Thin Solid Films **519** (21), 7341-7346 (2011).
120. G. Hanna, T. Glatzel, S. Sadewasser, N. Ott, H. P. Strunk, U. Rau and J. H. Werner, Applied Physics A **82** (1), 1-7 (2006).
121. S. S. Schmidt, D. Abou-Ras, S. Sadewasser, W. Yin, C. Feng and Y. Yan, Physical Review Letters **109** (9) (2012).
122. M. Cojocaru, x, O. din, C. Pyuck-Pa, D. Abou-Ras, S. S. Schmidt, R. Caballero and D. Raabe, Photovoltaics, IEEE Journal of **1** (2), 207-212 (2011).
123. D. Abou-Ras, B. Schaffer, M. Schaffer, S. S. Schmidt, R. Caballero and T. Unold, Physical Review Letters **108** (7) (2012).
124. W. J. Yin, Y. Wu, R. Noufi, M. Al-Jassim and Y. Yan, Applied Physics Letters **102** (19) (2013).
125. Y. Yan, W.-J. Yin, Y. Wu, T. Shi, N. R. Paudel, C. Li, J. Poplawsky, Z. Wang, J. Moseley, H. Guthrey, H. Moutinho, S. J. Pennycook and M. M. Al-Jassim, Journal of Applied Physics **117** (11), 112807 (2015).
126. C. S. S. R. Kumar, *Transmission Electron Microscopy Characterization of Nanomaterials*. (Springer Berlin Heidelberg, 2013).
127. T. Kaplan, F. Liu, M. Mostoller, M. F. Chisholm and V. Milman, *A Large Scale Ab Initio Study of Impurities in Si Edge Dislocations*. (1996).
128. J. Dietrich, D. Abou-Ras, S. S. Schmidt, T. Rissom, T. Unold, O. Cojocaru-Mirédin, T. Niermann, M. Lehmann, C. T. Koch and C. Boit, Journal of Applied Physics **115** (10), 103507 (2014).
129. D. Barragan-Yani and K. Albe, Physical Review B **95** (11), 115203 (2017).
130. D. Hull and D. J. Bacon, *Introduction to Dislocations*. (Elsevier Science, 2001).
131. H. Föll and B. O. Kolbesen, Applied physics **8** (4), 319-331 (1975).
132. J. Pohl and K. Albe, Physical Review B **87** (24) (2013).
133. L. Lymperakis, J. Neugebauer, M. Albrecht, T. Remmele and H. P. Strunk, Physical Review Letters **93** (19), 196401 (2004).
134. H. Stange, S. Brunken, H. Hempel, H. Rodriguez-Alvarez, N. Schäfer, D. Greiner, A. Scheu, J. Lauche, C. A. Kaufmann, T. Unold, D. Abou-Ras and R. Mainz, Applied Physics Letters **107** (15), 152103 (2015).
135. M. H. Bode, Journal of Applied Physics **76** (1), 159-162 (1994).
136. M. H. Bode, M. M. Al-Jassim, J. Tuttle and D. Albin, MRS Proceedings **283** (1992).
137. R. Klenk, T. Walter, H.-W. Schock and D. Cahen, Advanced Materials **5** (2), 114-119 (1993).
138. U. Müller, *Symmetry Relationships between Crystal Structures: Applications of Crystallographic Group Theory in Crystal Chemistry*. (OUP Oxford, 2013).
139. S. Nishiwaki, N. Kohara, T. Negami, H. Miyake and T. Wada Japanese Journal of Applied Physics **38** (5R), 2888 (1999).
140. D. J. Chakrabarti and D. E. Laughlin, Bulletin of Alloy Phase Diagrams **2** (3), 305-315 (1981).
141. S. R. Gosavi, N. G. Deshpande, Y. G. Gudage and R. Sharma, Journal of Alloys and Compounds **448** (1–2), 344-348 (2008).
142. H. Liu, X. Shi, F. Xu, L. Zhang, W. Zhang, L. Chen, Q. Li, C. Uher, T. Day and G. J. Snyder, Nat Mater **11** (5), 422-425 (2012).
143. N. H. Abrikosov, V. F. Bankina, M. A. Korzhuev, G. K. Demski and O. A. Teplov, Soviet Physics Solid State **25** (1983).
144. K. Momma and F. Izumi, Journal of Applied Crystallography **44** (6), 1272-1276 (2011).
145. C. T. Koch, Determination of core structure periodicity and point defect density along dislocations. PhD Thesis, Arizona State University (2002).
146. K. Kimoto, T. Asaka, X. Yu, T. Nagai, Y. Matsui and K. Ishizuka, Ultramicroscopy **110** (7), 778-782 (2010).

This page intentionally left blank.

Acknowledgements

I would like to acknowledge Helmholtz Virtual Institute VI-520 “Microstructure Control for Thin-film Solar Cells” for being the primary financial support for this work. I would like to mention that this work has also been supported in part by the European Union Seventh Framework Program [FP/2007] under Grant Agreement No. 312483 (ESTEEM 2).

I gratefully acknowledge Prof. Dr. Peter A. van Aken, for giving me the opportunity to do my PhD in the Stuttgart Center for Electron Microscopy, for being my doctoral advisor and for his encouragement, support and guidance during my PhD study. I am also grateful to him for his understanding at hard times.

I would like to thank Prof. Dr. Hans-Joachim Kleebe for accepting me as his PhD student and for his support throughout the VI-520 project.

I would like to thank Prof. Dr. Wolfram Jaegermann and Prof. Dr. Christoph T. Koch for accepting to be my examiners at my defense and reading my thesis.

I am grateful to my non-official, long-distance supervisor Prof. Dr. Quentin M. Ramasse for his guidance throughout my PhD. He has always been supportive and encouraging. I would like to thank him for the long hours that we spent together at Nion UltraSTEM 100. I appreciate his efforts in correcting my manuscripts and thesis. I would also like to acknowledge Prof. Dr. Quentin M. Ramasse, Dr. Demie Kepaptsoglou and Dr. Fredrik Hage for their hospitality during my stay at the SuperSTEM.

Dr. Wilfried Sigle was also my non-official supervisor. I am indebted to him for being ready to help at any time. He has always been so kind to support me in every aspect.

I would like to thank the coordinator of the VI-520 project PD Dr. Daniel Abou-Ras for his time and efforts in correcting my manuscripts and my thesis. He has been encouraging and supportive at all times. Also thanks to him for preparing nice work atmosphere throughout the VI project by bringing experts from various fields. I would like to acknowledge Dr. Roland Mainz, for providing me the first set of samples at the beginning of my PhD studies. I would like to thank to all PhD students of the VI-520 project for keeping a friendly work atmosphere in the past years. I would like to acknowledge Dr. Helena Stange for sample growth and Daniel Barragan-Yani for the theoretical calculations. I would like to thank Max Kahnt, Sibylle Bergmann and Dr. Norbert Schäfer for their valuable contribution to the project.

I am thankful to Dr. Bernhard Fenk for preparing the TEM lamellas by FIB. Without those well prepared samples, it would not be possible to realize this work.

Many thanks to former and current members of the StEM group. First, I would like to thank Caroline Heer. With her big smile she supported me at various topics, including the personal ones. I appreciate the guidance by Ute Salzberger and Marion Kelsch in sample preparation. Dr. Vesna Srot introduced me to her son, VG 501, and this helped me at the beginning of my PhD studies. Special thanks to Marion Kelsch and Dr. Vesna Srot, who surprised me with their presents at various occasions. I would like to acknowledge Kersten Hahn and Peter Kopold, for giving trainings at several microscopes and keeping the microscopes running. Together with Dr. Fritz Phillipp we tried to understand the structure of complex defects. I would like to thank him for his efforts. Dr. Yi Wang deserves special thanks for helping me with QSTEM, at the ARMs and with the data analysis by writing small scripts. I would especially thank to Nilesh Vats and Robin Lingstädt, whom I share the office, for making the office alive, sharing daily life`s happiness and stress. Last but not least, many thanks to my colleagues/friends Dr. Cigdem Ozsoy Keskinbora, Eren Suyolcu and Dr. Burcu Ögüt for being supportive in all matters.

Former and current members of ‘Turkish Mafia’ at the institute made my life joyful. I would like to thank Dr. Semanur Baylan ‘the cook’, Dr. Kahraman Keskinbora, Dr. Yeliz Unutulmazsoy, Dr. Burcu Minsky and Joel Minsky, Dr. Pinar Kaya, Ceren Yasa, Oncay Yasa, Dr. Utku Culha and Dr. Hakan Ceylan.

Thanks to the members of my family-in-law, Öngün Sanlı, Murat Sanlı and Aydın Can Sanlı, for supporting me continuously with their enthusiasm.

My dear mother Sakine Şimşek and father Sever Şimşek, I am indebted to your love, encouragement, guidance and support in every aspect of my life. We realized it together. Sonsuz teşekkürler.

My best friend and dear husband Umut T. Sanlı, without your presence, continuous support and encouragement it would not be possible to write these final sentences. Thanks for everything, but especially for our discussions and your comments on each and every single page of my life, my manuscripts and my thesis. Without your support, the story would not be so nice. Iyi ki varsın.

Curriculum vitae

PERSONAL DATA

Name	Ekin Şimşek Sanlı
Birthday	04.09.1986
Place of birth	Ankara / Turkey

EDUCATION

2012 – 2018 Stuttgart, Germany	Ph.D. student in the Stuttgart Center for Electron Microscopy group at the Max Planck Institute for Solid State Research
2009 – 2011 Kiel, Germany	International Master's Program at the Christian Albrechts University of Kiel in Materials Science
2004 – 2009 Eskisehir, Turkey	B. Sc. degree at Anadolu University in Materials Science and Engineering

PUBLICATIONS

1. C. Li, **E. Simsek Sanli**, H. Strange, M. D. Heinemann, D. G. Schäfer, R. Mainz, W. Sigle, D. Abou-Ras, P. A van Aken; "In-situ observations of recrystallization in CuInSe2 solar cells via STEM", *Microsc. Microanal.* **24** (S1), 1492-1493 (2018); doi: 10.1017/S1431927618007948

2. **E. Simsek Sanli**, Q. M. Ramasse, R. Mainz, A. Weber, D. Abou-Ras, W. Sigle, P. A. van Aken; "Evidence for $Cu_{2-x}Se$ platelets at grain boundaries and within grains in $Cu(In,Ga)Se_2$ thin films", *Appl. Phys. Lett.* **111**, 032103 (2017); doi: 10.1063/1.4993917

3. S. S. Schmidt, S. Merdes, A. Steigert, R. Klenk, C. A. Kaufmann, **E. Simsek Sanli**, P. A. van Aken, M. Oertel, A. Schneikart, B. Dimmler, R. Schlatmann; "Interface engineering of CIGS/ALD-Zn(O,S) heterojunctions", *Jpn. J. Appl. Phys.* **56**, 08MC12 (2017); doi: 10.7567/JJAP.56.08MC16

4. **E. Simsek Sanli**, D. Barragan-Yani, Q. M. Ramasse, K. Albe, R. Mainz, D. Abou-Ras, A. Weber, H.-J. Kleebe, P. A. van Aken; "Point defect segregation and its role in the detrimental nature of Frank partials in $Cu(In,Ga)Se_2$ thin-film absorbers", *Phys. Rev. B* **95**, 195209 (2017); doi: 10.1103/PhysRevB.95. 195209

5. **E. Simsek Sanli**, Q.M. Ramasse, W. Sigle, D. Abou-Ras, R. Mainz, A. Weber, H.-J. Kleebe, P.A. van Aken, "Elemental redistributions at structural defects in $Cu(In,Ga)Se_2$ thin films for solar cells", *J. Appl. Phys.* **120**, 205301-1-7 (2016); doi: 10.1063/1.4967731

6. R. Mainz, **E. Simsek Sanli**, H. Stange, D. Azulay, S. Brunken, D. Greiner, S. Hajaj, M. D. Heinemann, C. A. Kaufmann, M. Klaus, Q. M. Ramasse, H. Rodriguez-Alvarez, A. Weber, I. Balberg, O. Millo, P. A. van Aken, D. Abou-Ras; "Annihilation of structural defects in chalcogenide absorber films for high-efficiency solar cells", *Energy Environ. Sci.* **9**, 1818-1827 (2016); doi: 10.1039/c6ee00402d

7. D. Abou-Ras, S. S. Schmidt, N. Schäfer, J. Kavalakkatt, T. Rissom, T. Unold, R. Mainz, A. Weber, T. Kirchartz, **E. Simsek Sanli**, P. A. van Aken, Q. M. Ramasse, H.-J. Kleebe, D. Azulay, I. Balberg, O. Millo, O. Cojocaru-Mirédin, D. Barragan-Yani, K. Albe, J. Haarstrich, C. Ronning; "Compositional and electrical properties of line and planar defects in $Cu(In,Ga)Se_2$ thin films for solar cells - a review", *Phys. Status. Solidi RRL* **10**, 363-375 (2016); doi: 10.1002/pssr.201510440

8. **E. Simsek**, Q. M. Ramasse, D. Abou-Ras, R. Mainz, A. Weber, H.-J. Kleebe, P. A. van Aken; "Linking microstructure and local chemistry in $Cu(In,Ga)Se_2$ thin-film solar cells", *Microsc. Microanal.* **21** (S3), 2279-2280 (2016); doi: 10.1017/S1431927615012179

9. Q. M. Ramasse, F. Azough, R. Freer, D. M. Kepaptsoglou, R. Mainz, A. Weber, D. Abou-Ras, **E. Simsek**, P. A. van Aken; "Atomic-Scale STEM-EELS characterization of the chemistry of structural defects and interfaces in energy-related materials", *Microsc. Microanal.* **20** (S3), 562-563 (2014); doi: 10.1017/S143192761400453X

PRESENTATIONS

1. **E. Simsek Sanli**, H. Stange, D. Greiner, D. Abou-Ras, N. Schäfer, R. Mainz, W. Sigle, P. A. van Aken; Microscopy Conference 2017; Poster presentation: “In-situ STEM measurement of grain growth in $CuInSe_2$ during $Cu_{2-x}Se$ in-diffusion”
2. **E. Simsek Sanli**, Q. M. Ramasse, W. Sigle, D. Abou-Ras, R. Mainz, A. Weber, H.-J. Kleebe, P. A. van Aken; StEM Workshop at Ringberg Castle, 2017; Oral Presentation: “Elemental redistributions at structural defects in $Cu(In,Ga)Se_2$ thin films for solar cells”
3. S. S. Schmidt, S. Merdes, A. Steigert, R. Klenk, C. A. Kaufmann, **E. Simsek Sanli,** M. Oertel, A. Schneikart, B. Dimmler, R. Schlatmann; International Photovoltaic Science and Engineering Conference-26; “Interface engineering of CIGS/ALD-Zn(O,S) heterojunctions”
4. D. Abou-Ras, N. Schäfer, J. Kavalakkatt, S. S. Schmidt, T. Rissom, R. Mainz, A. Weber, T. Unold, J. Haarstrich, C. Ronning, **E. Simsek Sanli,** P. A. van Aken, Q. M. Ramasse, H.-J. Kleebe, O. Cojocaru-Mirédin, D. Azulay, I. Balberg, O. Millo; 20th International Conference on Ternary and Multinary Compounds; “Enhanced understanding of planar defects in $Cu(In,Ga)Se_2$ by correlative, multiscale analyses and comparison with device simulations”
5. **E. Simsek Sanli**, Q. M. Ramasse, W. Sigle, D. Barragan, K. Albe, D. Abou-Ras, R. Mainz, A. Weber, H.-J. Kleebe, P. A. van Aken; International Workshop at Ringberg Castle, 2016; Oral presentation; “Analysis of structural defects in $Cu(In,Ga)Se_2$ thin-film solar cells by means of HR-STEM and EELS”
6. **E. Simsek Sanli**, H. Stange, W. Sigle, Q. M. Ramasse, D. Abou-Ras, R. Mainz, H.-J. Kleebe, P.A. van Aken; EMRS 2016 Spring Meeting; Poster presentation: “Influence of Na on the defect structures in $CuInSe_2$”
7. **E. Simsek Sanli**, Q. M. Ramasse, D. Abou-Ras, R. Mainz, A. Weber, H.-J. Kleebe, P. A. van Aken; MRS 2015 Fall Meeting; Poster presentation: “Analysis of structural defects in $Cu(In,Ga)Se_2$ thin-film solar cells”
8. **E. Simsek**, Q. M. Ramasse, D. Abou-Ras, R. Mainz, A. Weber, H.-J. Kleebe, P. A. van Aken; Microscopy Conference 2015; Poster presentation: “$Cu_{2-x}Se$ phase in $Cu(In,Ga)Se_2$ thin-film solar cells by means of HR-STEM and EELS”
9. **E. Simsek**, Q. M. Ramasse, D. Abou-Ras, R. Mainz, A. Weber, H.-J. Kleebe, P. A. van Aken; Microscopy & Microanalysis 2015; Oral presentation; “Linking microstructure and local chemistry in $Cu(In,Ga)Se_2$ thin-film solar cells”
10. **E. Simsek**, Q.M. Ramasse, D. Abou-Ras, R. Mainz, A. Weber, H.-J. Kleebe, P.A. van Aken; 18th International Microscopy Congress 2014; Poster presentation: “HR-STEM and EELS analyses of structural defects in $Cu(In,Ga)Se_2$”
11. **E. Simsek**, Q. M. Ramasse, D. Abou-Ras, R. Mainz, A. Weber, H.-J. Kleebe, P. A. van Aken; SuperSTEM Summer School: Advanced Topics in Aberration-Corrected STEM; Poster presentation; “High-resolution analytical STEM investigation of the microstructure in $Cu(In,Ga)Se_2$ thin films”
12. **E. Simsek**, Q. M. Ramasse, D. Abou-Ras, R. Mainz, A. Weber, H.-J. Kleebe, P. A. van Aken; StEM Workshop at Ringberg Castle, 2014; Oral presentation: “High-resolution analytical STEM investigation of the microstructure in $Cu(In,Ga)Se_2$ thin films”
13. **E. Simsek**, Q. M. Ramasse, D. Abou-Ras, R. Mainz, A. Weber, P. A. van Aken; EMRS 2014 Spring Meeting; Oral presentation; “Chemistry of structural defects in Cu(In,Ga)Se2 by means of STEM”
14. B. Erkartal, S. Hamann, **E. Simsek**, A. Ludwig, L. Kienle; Materials Science and Engineering MSE 2012; Oral presentation: “TEM Investigations of Fe-Pd-X (X = Pt, Mn, Cu) Ferromagnetic Shape Memory Thin Films”
15. **E. Simsek**, P. Kaya, S. Turan, G. Arslan and A. Kalemtas; 19th National Electron Microscopy Congress; Poster presentation: “Characterization of Al-AlN Composites”

Erklärung zur Dissertation

Hiermit versichere ich, die vorliegende Dissertation ohne Hilfe Dritter nur mit den angegebenen Quellen und Hilfsmitteln angefertigt zu haben. Alle Stellen, die aus Quellen entnommen wurden, sind als solche kenntlich gemacht. Diese Arbeit hat in gleicher oder ähnlicher Form noch keiner Prüfungsbehörde vorgelegen.

Darmstadt, im August 2018

(Ekin Şimşek Sanlı)